Analysis of $\bar{p}p \rightarrow \pi\pi\pi\eta$

Andrew Richard Cooper

Department of Physics

Queen Mary and Westfield College

University of London

December 19, 1994

A thesis submitted in accordance with the regulations for the Degree of Doctor of Philosophy in the University of London

To My Parents and Suzanne.

Abstract

Crystal Barrel $\bar{p}p \rightarrow \pi\pi\pi\eta$ data at 1.20GeV/c and 1.94GeV/c have been analysed. In the $\pi^0\pi^0\pi^0\eta$ data at 1.94GeV/c, two new $J^{PC}=2^{-+}$, isospin I=0 resonances are observed. A resonance with mass (1650±15) MeV and width (180±75) MeV is observed to decay into $a_2(1320)\pi^0$. The second new resonance has (1850±30) MeV mass with (225±75) MeV width and decays into $f_2(1270)\eta$. The resonance with 1650 MeV mass is a natural candidate for the η_2, the I=0 partner of the $\pi_2(1670)$. A third resonance with $J^{PC}=2^{++}$ is observed with a (2135±50) MeV mass and (250±50) MeV width; it is observed with decay modes into both $a_2(1320)\pi^0$ and $f_2(1270)\eta$. This third resonance is consistent with the $f_2(2170)$ claimed by GAMS. A tentative signal for a $J^{PC}=0^{-+}$ resonance with a (1625-1650) MeV mass decaying into $f_0(975)\eta$ is also observed.

Contents

Chapter 1

Introduction

1.1 Quarks and Leptons

Particle physics is the study of the fundamental constituents of matter and their interactions. These fundamental or 'elementary' constituents are considered to be point-like particles which contain no internal structure (at least to a level of 10^{-17}m) and can be divided into two groups: *quarks* and *leptons*. Quarks are spin $\frac{1}{2}$ fermions with fractional electric charge. There are 6 types or *flavours* of quarks which can be grouped into three *generations* as seen in Table 1.1. Until recently the top quark has been a prediction, now tentative evidence for it's observation has been published.[1] An example of a particle containing quarks is the proton.

up (u)	charm (c)	top (t)
down (d)	strange (s)	bottom (b)

Table 1.1: Table of quarks. The antimatter quarks are denoted by a bar above the quark symbol eg the anti-up quark, $\bar{u}$.

Each quark has an additive quantum number corresponding to it's flavour. These quantum numbers can be found in Table 1.2. Convention has it that the sign of the quantum number is the same as that of it's electronic charge.

Property	Quark					
	d	u	s	c	b	t
Electric Charge, Q	$-\frac{1}{3}$	$+\frac{2}{3}$	$-\frac{1}{3}$	$+\frac{2}{3}$	$-\frac{1}{3}$	$+\frac{2}{3}$
Isospin z-component, I_z	$-\frac{1}{2}$	$+\frac{1}{2}$	0	0	0	0
Strangeness, S	0	0	-1	0	0	0
Charm, C	0	0	0	+1	0	0
Bottomness, B	0	0	0	0	-1	0
Topness, T	0	0	0	0	0	+1

Table 1.2: Quark additive quantum numbers

These quantum numbers are conserved when quarks are involved in interactions due to the strong force, discussed in the next section.

The leptons are spin$\frac{1}{2}$ fermions with integer electric charge. Like quarks, there are six flavours and they can be grouped into three generations.

Q = -1	electron (e^-)	muon (μ^-)	tau(τ^-)
Q = 0	neutrino (ν_e)	neutrino (ν_μ)	neutrino (ν_τ)

Table 1.3: The leptons are the electron, muon and tau with the corresponding neutrinos.

The vast majority of the observable universe is composed of particles containing the up and down quarks and electrons.

1.2 Quark Interactions

The basic interactions of quarks and leptons can be described by the standard electroweak model[2][3][4][5] and quantum chromodynamics (QCD)[2][6]. Interactions due to the electromagnetic and weak force may occur between all quarks and leptons but interactions due to the strong force, described by QCD, only occur between quarks. The strength of the strong force is so great, that the interactions due to the electroweak force are negligible in comparison: it is the strong force that is able to bind the positively charged protons together to form nuclei.

The quarks, unlike leptons, have an additional kind of charge: *colour*. The colour charge is the source of the attraction/repulsion manifested in the strong force in the same way that electronic charge is observed in the electromagnetic force. The electronic charge has two states: positive and negative. In contrast, the colour charge has three: *red*, *green* and *blue*. Including the anti-colour (anti-red, anti-green and anti-blue) gives six different colour states. Particles with electronic charge tend to bind together to form a composite neutral particle and this is also observed with the coloured quarks. An example of this can be seen in the proton which contains three quarks. Each quark has a different colour charge to form a neutral or *white* colour charge. Particles containing quarks are classed as *hadrons* and these can be reduced into two groups: *Baryons* are particles with three quarks. *Meson* particles contain a quark and anti-quark pair eg the pion ($\pi^+ = \mathrm{u}\bar{d}$).

A major difference between the electromagnetic and strong force lies in the propagation of the force. All forces are considered to be propagated by the exchange of massless bosons. In the case of the electromagnetic force, the bosons are virtual photons. The propagators for the strong force are *gluons*. The virtual photons do not carry electric charge, but gluons carry colour and are therefore able to interact with one another. This self-coupling gives rise to a rapid variation of the coupling constant, α_s, with energy scale, μ. As the energy scale tends to infinity, the coupling constant tends to zero, (there is no force between the quarks): a characteristic termed as asymptotic freedom. This principle of asymptotic freedom is illustrated in equation 1.1.

$$\alpha_s(\mu) = \frac{12\pi}{(33-2n_f)\ln(\mu^2/\Lambda^2)} \times \left[1 - \frac{6(153-19n_f)}{(33-2n_f)^2}\frac{\ln[\ln(\mu^2/\Lambda^2)]}{\ln(\mu^2/\Lambda^2)}\right] + \cdots \quad (1.1)$$

where n_f is the number of quarks with mass less than the energy scale. Λ is a parameter with arbitrary definition and arises to replace a constant of integration when α_s is determined for a fixed energy scale, μ_0.

At small energies, equivalent to large distances, the coupling constant tends to infinity, an effect called confinement. It is in this latter energy scale region that hadrons are formed, but the use of perturbative methods become invalid. QCD is therefore unable to provide an insight into the principles of hadron formation such as why hadrons appear as two or three quark combinations. Alternative combinations are expected, but have not been decisively observed. Such exotic states are:-

- $q\bar{q}q\bar{q}$ - Two bound mesons form a molecule.
- qqg - Hybrid states in which a quark is replaced by a gluon.
- gg and ggg - Glueballs where gluons form a bound state without quarks.

1.3 Quark Model

Empirical work towards an understanding of hadrons has given rise to the quark model[7]. The quark model groups them into *nonets* and is used to predict the masses of mesons. Each nonet contains mesons with specific spin, J, parity, P, and charge conjugation, C. The $J^{PC} = 0^{-+}$ nonet (Table 1.4), contains mesons with u,d and s quarks.

If the orbital angular momentum of a $q\bar{q}$ state is L, then the parity of a meson is given by:-

$$P = (-1)^{L+1} \quad (1.2)$$

Meson	Quark Content	Isospin (I)	I_z	Strangeness
π^+	$u\bar{d}$	1	1	0
π^-	$d\bar{u}$	1	-1	0
π^0	$(d\bar{d} - u\bar{u})/\sqrt{2}$	1	0	0
K^+	$u\bar{s}$	$\frac{1}{2}$	$\frac{1}{2}$	+1
K^0	$d\bar{s}$	$\frac{1}{2}$	-$\frac{1}{2}$	+1
K^-	$\bar{u}s$	$\frac{1}{2}$	-$\frac{1}{2}$	-1
$\bar{K}^0$	$\bar{d}s$	$\frac{1}{2}$	$\frac{1}{2}$	-1
η	$(d\bar{d} + u\bar{u} - 2s\bar{s})/\sqrt{6}$	0	0	0
η'	$(d\bar{d} + u\bar{u} + s\bar{s})/\sqrt{3}$	0	0	0

Table 1.4: The $J^P = 0^-$ nonet of pseudoscalar mesons.

A state with one flavour (eg $u\bar{u}$) has a charge conjugation given by:-

$$C = (-1)^{L+S} \tag{1.3}$$

where the spin, S = 0 or 1.

States with the same IJ^P and additive quantum numbers can mix. If a state is an eigenstate of charge conjugation then, to mix, the states must also have the same value of C. This state mixing produces the π^0, η and $\eta'(958)$. Mesons from this $J^P = 0^-$ nonet are called the *pseudoscalar mesons*. Other nonets include:-

- $J^P = 0^+$: Scalar mesons
- $J^P = 1^-$: Vector mesons
- $J^P = 1^+$: Axial-vector mesons
- $J^P = 2^-$: Pseudotensor mesons
- $J^P = 2^+$: Tensor mesons.

Some assignments of mesons to these nonets can be found in Table 1.5. As can be seen from Table 1.5, a large number of states remain unobserved. Some of the assignments, particularly in the 0^{++} multiplet, are controversial. The $f_0(975)$ and $a_0(980)$ are both candidates for $K\bar{K}$ molecules.[8] [9] One of the objectives for meson spectroscopy is to fill in the gaps and identify exotic states.

1.4 Meson Spectroscopy

Meson spectroscopy is one of the oldest forms of particle physics but still retains an important role. It is a unique area within particle physics since the associated theory has lagged behind the empirical research. The success of experimental meson spectroscopy is due to the large abundance of mesons, the simplicity and relatively low cost of the experiments. Several approximations to the low energy perturbative regime of QCD have arisen to predict masses and decay properties of meson and exotic states: The bag-model[8], the flux-tube model[10], chiral perturbation theory[11] and lattice gauge theory[12]. However, their results and predictions differ significantly.

Identification of new mesons is becoming increasingly difficult. Mesons with large branching ratios and narrow widths are now well established despite occasional confusion over spin-parity assignments. The remaining mesons still to be found are difficult to observe due to one (or a combination) of the following characteristics:-

- Low branching ratio.
- Large width.
- High mass.

Mesons with low branching ratios require the accumulation of vast amounts of data before their signals are statistically significant. Mesons with large widths are difficult to observe in *invariant mass* distributions. The invariant mass technique

$N^{2S+1}L_J$	J^{PC}	$u\bar{d}$, $u\bar{u}$, $d\bar{d}$ I = 1	$u\bar{u}$, $d\bar{d}$, $s\bar{s}$ I = 0	$c\bar{c}$ I = 0	$b\bar{b}$ I = 0	$\bar{s}u$, $\bar{s}d$ I = 1/2	$c\bar{u}$, $c\bar{d}$ I = 1/2	$c\bar{s}$ I = 0	$\bar{b}u$, $\bar{b}d$ I = 1/2
$1\,^1S_0$	0^{-+}	π	η,η'	η_c		K	D	D_s	B
$1\,^3S_1$	1^{--}	ρ	ω,ϕ	$J/\psi(1S)$	$\Upsilon(1S)$	$K^*(892)$	$D^*(2010)$	$D_s^*(2110)$	$B^*(5330)$
$1\,^1P_1$	1^{+-}	$b_1(1235)$	$h_1(1170)$,$h_1(1380)$			K_{1B}	$D_1(2420)$	$D_{s1}(2536)$	
$1\,^3P_0$	0^{++}	$a_0(1450)$	$f_0(1335)$,$f_0(1590)$	$\chi_{c0}(1P)$	$\chi_{b0}(1P)$	$K_0^*(1430)$			
$1\,^3P_1$	1^{++}	$a_1(1260)$	$f_1(1285)$,$f_1(1510)$	$\chi_{c1}(1P)$	$\chi_{b1}(1P)$	K_{1A}			
$1\,^3P_2$	2^{++}	$a_2(1320)$	$f_2(1270)$, $f_2'(1525)$	$\chi_{c2}(1P)$	$\chi_{b2}(1P)$	$K_2^*(1430)$	$D_2^*(2460)$		
$1\,^1D_2$	2^{-+}	$\pi_2(1670)$							
$1\,^3D_1$	1^{--}	$\rho(1700)$	$\omega(1600)$	$\psi(3770)$		$K^*(1680)$			
$1\,^3D_2$	2^{--}					$K_2(1770)$			
$1\,^3D_3$	3^{--}	$\rho_3(1690)$	$\omega_3(1670)$, $\phi_3(1850)$			$K_3^*(1780)$			
$1\,^3F_4$	4^{++}	$a_4(2040)$	$f_4(2050)$,$f_4(2220)$			$K_4^*(2045)$			
$2\,^1S_0$	0^{-+}	$\pi(1300)$	$\eta(1295)$	$\eta_c(2S)$		$K(1460)$			
$2\,^3S_1$	1^{--}	$\rho(1450)$	$\omega(1390)$,$\phi(1680)$	$\psi(2S)$	$\Upsilon(2S)$	$K^*(1410)$			
$2\,^3P_2$	2^{++}		$f_2(1640)$		$\chi_{b2}(2P)$	$K_2^*(1980)$			
$3\,^1S_0$	0^{-+}	$\pi(1770)$	$\eta(1760)$			$K(1830)$			

Table 1.5: Meson Table.

requires the measurement of the energy and momentum of all the final state particles from the annihilation. The invariant mass, M, of n combined particles is given by equation 1.4.

$$M = \sqrt{E^2 - P^2} \tag{1.4}$$

where the total momentum, P, is given by it's components in the x,y,z directions p_x,p_y,p_z as:

$$P^2 = (\sum_i^n p_x^i)^2 + (\sum_i^n p_y^i)^2 + (\sum_i^n p_z^i)^2 \tag{1.5}$$

and the total energy is $E = \sum_i^n E_i$. An example of an invariant mass distribution can be seen in Figure 1.1.

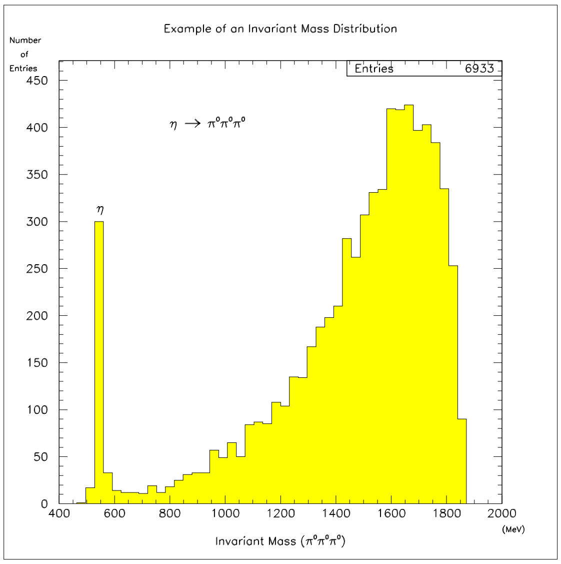

Figure 1.1: Invariant mass distribution for $(\pi^0\pi^0\pi^0)$ from $\bar{p}p \to \pi^0\pi^0\pi^0\eta$ data. The peak at about 550MeV is due to the decay of η (η mass = 547.45MeV) particles into $\pi^0\pi^0\pi^0$.

Mesons with relatively large masses (*ie* above 1500MeV) are not produced in significant numbers from antiproton-proton annihilation at rest. The latter annihilation occurs mainly from an S-wave initial state: a constraint used to great effect when spin analysis is used. Increasing the initial protonium energy increases the number of possible initial spin states.

To compound the problems in searching for new mesons and filling nonets, exotic states have to be identified. It has been proposed[13] that some exotic states may have a spin-parity forbidden to $q\bar{q}$ eg $J^{PC} = 0^{--}$, 0^{+-}, 1^{-+} and 2^{+-}. However, no evidence for such states with abnormal J^{PC} has been found. Exotic states with acceptable $q\bar{q}$ spin-parity may be found by counting states. Once a nonet has been assigned nine resonances, a further state with the same quantum numbers provides evidence that one of the ten states is exotic. To identify which of the ten states does not fit in the nonet, the mass and relative strength of decay modes need to be studied. Reviews of the search for exotic states can be found in references [14],[15] and [16].

A model (based on spherical cavity approximation) used to predict glueball masses[17] agrees well with the current glueball candidates:-

- 0^- $\eta(1440)$ from Mark III data. [7]
- 0^+ $f_0(1500)$ from Crystal Barrel data. [18]
- 0 or 2^+ $\theta(1710)$ from Mark III and WA76 data. [19]

This model also predicts a $J^{PC} = 2^{-+}$ glueball with a mass in the region of 1700MeV. So far, no candidate for a 2^{-+} glueball has been observed.

1.5 Crystal Barrel Experiment

The Crystal Barrel detector[20] was designed and built with the main purpose of searching for exotic states produced in antiproton-proton annihilations. An emphasis was placed on decay channels without charged particles in the annihilation product since many exotic states are expected to decay into neutral particles and the amount of *all neutral* data from previous experiments was small.

The motivation for this analysis is to use $\bar{p}p \to \pi\pi\pi\eta$ Crystal Barrel data in order to observe some of the missing states, notably the I=0 $^1D_2$ state missing from Table 1.5. The observation of more than one 2^- state contributes to the search for the missing 2^- glueball candidate.

1.6 The Scope of this Thesis

In Chapter 4, four sets of data will be presented:

- $\bar{p}p \to \pi^+\pi^-\pi^0\eta$ at 1.2 and 1.94GeV/c
- $\bar{p}p \to \pi^0\pi^0\pi^0\eta$ at the same momenta.

The qualitative features of the data are discussed there. Chapter 5 discusses a maximum likelihood fit to the $\pi^0\pi^0\pi^0\eta$ data at 1.94GeV/c. These were chosen for the first analysis for two reasons. Firstly a promising signal is visible by eye around $\eta\pi^0\pi^0$ masses of 1650MeV, where a 2^{-+} resonance is expected. Secondly, the isospin content of these data is simpler than $\pi^+\pi^-\pi^0\eta$, which contains a strong ρ signal and potentially I=1 $\eta\pi^\pm\pi^0$ resonances.

This choice turned out to be a good one. Three definite resonances are located in the $\pi^0\pi^0\pi^0\eta$ data and a possible fourth. However, the analysis has been lengthy and complex. In the time available, it has not been possible to complete maximum likelihood analyses of the remaining three data sets. That remains a task for the future.

Chapter 2

The Crystal Barrel Detector

2.1 Introduction

The Crystal Barrel spectrometer is based at CERN and is used to study antiproton-proton ($\overline{p}p$) and antiproton-deuterium ($\overline{p}d$) annihilations. The source of protons is a liquid hydrogen target and the antiprotons are provided by an intense and very pure monoenergetic antiproton beam from the Low Energy Antiproton Ring (LEAR).

LEAR is able to supply antiprotons with a momentum in the range ($0.06 \rightarrow 2.0$)GeV/c. At 0.2GeV/c; antiprotons are brought to rest in liquid hydrogen; above this momentum, annihilations are *in flight, ie* the annihilation occurs with a non-zero momentum in the laboratory reference frame. The beam intensity extracted from LEAR is typically $10^4\overline{p}s^{-1} \rightarrow 10^6\overline{p}s^{-1}$. The spill from LEAR can last up to 3 hours before the antiproton accumulator (AA) has to refill LEAR.

The Crystal Barrel detector is designed to give good energy and momentum resolution in the measurement of charged and neutral particles resulting from the $\bar{p}p$ annihilations. It covers almost the full 4π solid angle surrounding the target. As can be seen in Figure 2.1, the general layout of the detector is similar to that of other large detectors involved in high energy physics experiments.

The Crystal Barrel detector's basic components and their corresponding perfor-

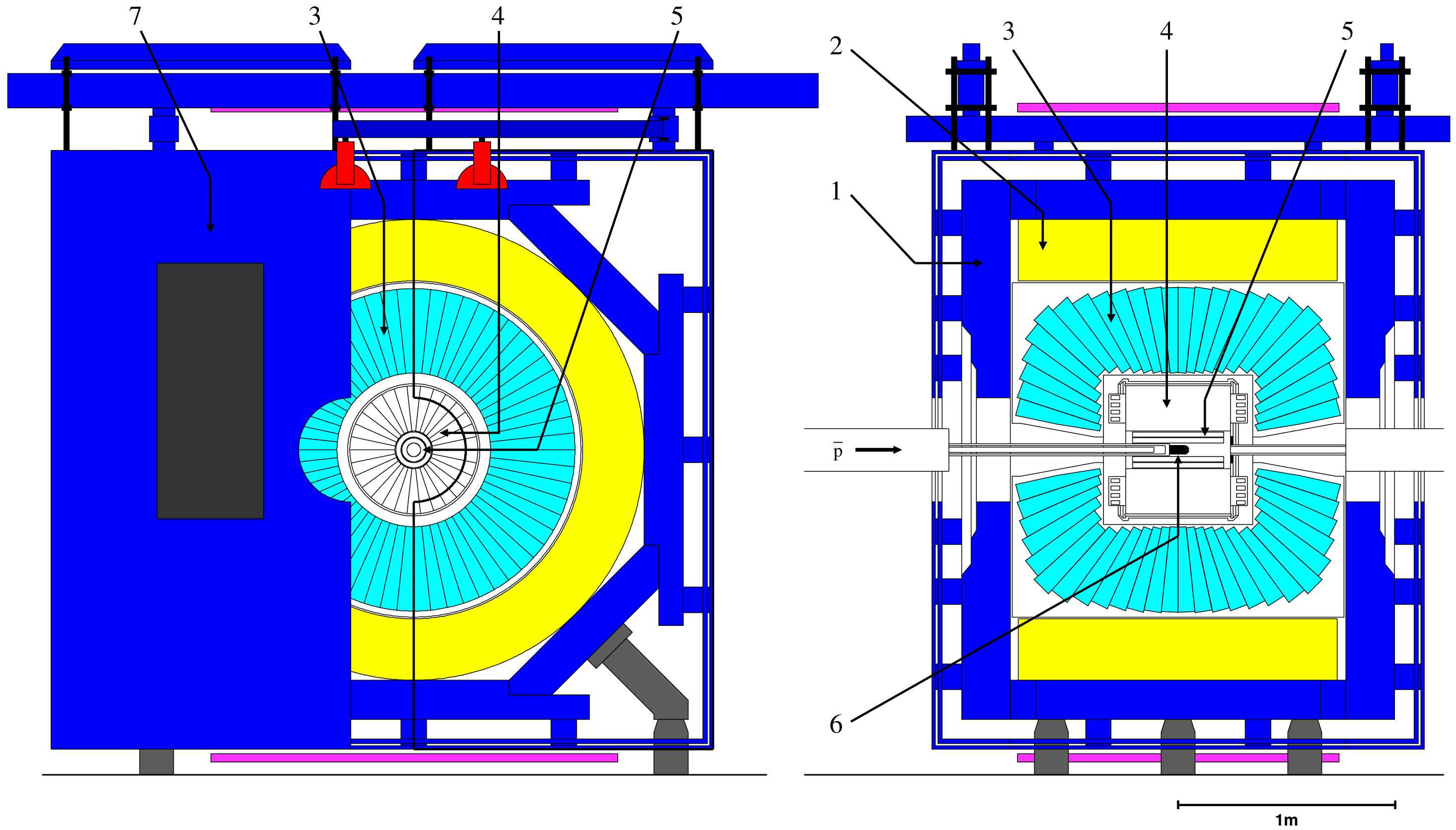

Figure 2.1: The Crystal Barrel Spectrometer. (1) Magnet yoke. (2) Magnet coils. (3) CsI(Tl) barrel. (4) Jet drift chamber. (5) Proportional chamber. (6) Liquid hydrogen target.

mance are described in the following sections.

2.2 Counters and Hydrogen Target

A schematic diagram of the liquid hydrogen target and beam counters can be seen in Figure 2.2.

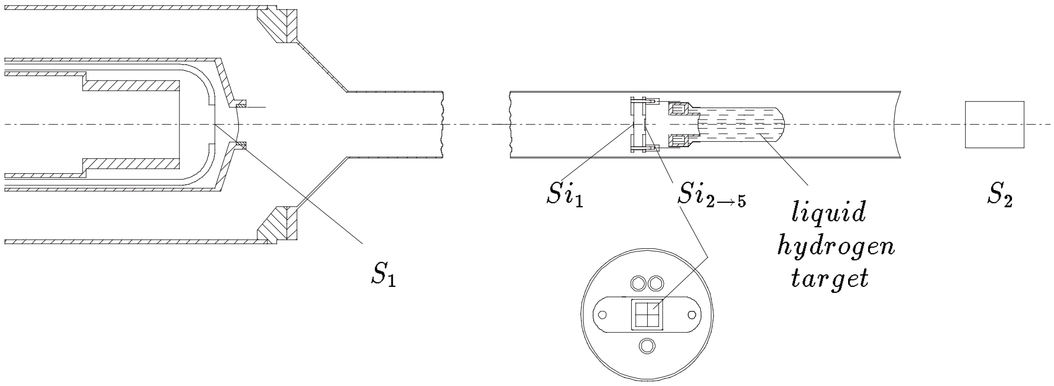

Figure 2.2: Beam Counters and Liquid Hydrogen Target

From the LEAR vacuum, the antiprotons pass through a 100μm beryllium window, a counter S_1 and a 50μm mylar window before entering the target vacuum. To reach the liquid hydrogen target, the antiprotons must pass through two more counters; Si_1 and $Si_{2\to5}$. The liquid hydrogen target is 17mm in diameter, 44mm in length along the beam axis and has a 10mm diameter entrance window. Antiprotons that do not interact in the liquid hydrogen target are vetoed in a counter, S_2, approximately 20cm downstream of the target.

The type, purpose and performance of the four beam counters are as follows:-

- S_1 is used for beam steering and focussing. A scintillator viewed by photomultiplier tubes and alternatively a fast multiwire proportional counter have been used for S_1. Both counters were found to have an intrinsic efficiency verging on 100%.

- Si_1 is a silicon detector used for beam focussing and can also be used as a trigger. Silicon counters of varying thicknesses, depending on the antiproton beam momentum have been used for Si_1. The intrinsic efficiencies of these counters are approximately 98%.

- $Si_{2\rightarrow5}$ are an array of silicon counters used for final beam steering and focussing. A signal from $Si_{2\rightarrow5}$ begins the start signal for the higher level triggers. Segmented silicon diodes with $\sim 98\%$ intrinsic efficiency have been used for $Si_{2\rightarrow5}$. For steering, the counters are divided up into four quadrants, each quadrant read out separately. Since the counter is attached to the target frame, the counter is cooled to -100°C, providing a significant reduction in the counter's noise and leakage current relative to room temperature operation. The uncertainty in trigger time, 0.5ns, is due to the rise-time of the trigger signals. The antiproton beam is directed at the lower two quadrants to avoid any bubbles at the surface of the hydrogen target.

- S_2 acts as a veto counter for antiprotons that have not interacted in the target. A 25mm diameter scintillator counter and a 28mm diameter silicon counter have been used. The typical efficiency of S_2 is greater than 95%.

At 0.2Gev/c, 40% of antiprotons pass through $Si_{2\rightarrow5}$ from S_1. The loss of antiprotons is mainly due to multiple scattering in the vacuum windows and S_1; 0.6% of antiprotons annihilate in $Si_{2\rightarrow5}$. For in flight data, more than 99% of antiprotons pass through $Si_{2\rightarrow5}$. The three dominant processes of antiproton interaction within the liquid hydrogen are elastic scattering, charge exchange and antiproton-proton annihilation. Table 2.1 shows the cross section for the three processes at different beam momenta.

Beam Momentum (GeV/c)	Annihilation (mb)	Elastic Scattering (mb)	Charge Exchange (mb)
1.20	60	40	5
1.94	40	30	3

Table 2.1: Cross sections for dominant processes.

2.3 Proportional Wire Chambers

Two concentric cylindrical proportional wire chambers, PWC1 and PWC2, surround the liquid hydrogen target with their axes along the beam axis. They are primarily used for triggering on the multiplicity of the final state charged particles but also give (r,ϕ) coordinates near to the annihilation vertex. Space limitations prevent the use of preamplifiers for the cathode read-out and therefore no measurements of the z-coordinates are made.

The designs of the two chambers are very similar. The anode wires of length 35cm run parallel to the magnetic field and are made of 15μm diameter gold plated tungsten. The cathode cylinders are made of 22μm thick aluminium foil and are positioned 2.5mm from the sense wires. The inner chamber, PWC1, has 90 anode wires at a radius of 25.5mm from the beam axis and the outer chamber, PWC2, has 150 anode wires at a radius of 43mm. The gas composition used is 69.5% argon, 30% ethane and 0.5% of freon. The operational voltages for both chambers is approximately 2550V with current $\leq 0.5\mu$A. The geometrical acceptances of PWC1 and PWC2 are 99% and 97% of 4π. The chambers have a $\geq$ 99% detection efficiency for minimum ionizing particles.

The chambers are read out using PCOS III commercial systems[21]. Signals from the chamber are amplified and passed through a programmable discriminator (of threshold 2 $\rightarrow$ 15 μA) producing ECL logical output signals which then enter the PCOS III receivers. The receivers have a computer controlled delay (300ns $\rightarrow$

682ns) to synchronize the signals with those of the incident antiproton trigger. The signals are then sent through a crate readout controller, a CAMAC interface and finally to the computer. A second output from the receivers is used to calculate the charged track multiplicity. The measured multiplicity is compared to a preset multiplicity by a programmable look up unit where a trigger decision is made.

2.4 Jet Drift Chamber

A cylindrical drift chamber (JDC) surrounds the PWCs and provides tracking information for charged particles. The JDC may also be used in a trigger for the charged particle multiplicity. A schematic diagram of the JDC can be seen in Figure 2.3.

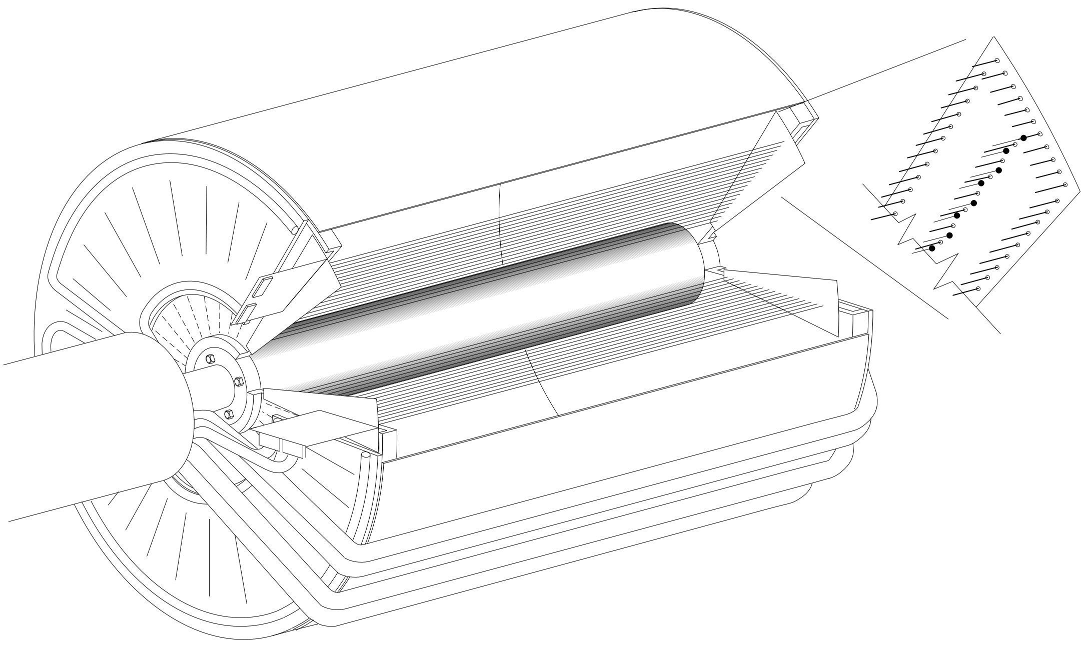

Figure 2.3: The Jet Drift Chamber. Staggering of the sense wire positions, shown in the expanded drawing, has been exaggerated for clarity.

JDC stands for the jet drift chamber type of drift cell[22]; The chamber is divided up into 30 azimuthal sectors and 23 radial layers with 8mm spacing. The inner and outer sense wires have a radius of 63mm and 239mm respectively with a sensitive length of 399mm. The corresponding detection solid angle is 95% of 4π, though this is reduced to 93% by a track fitting requirement of at least 3 layers in a track. Segmentation of the chamber enables a good dE/dx resolution and therefore $\pi^{\pm}/K^{\pm}$ separation for momenta below 500MeV/c.

Three types of wires are used in the chamber: sense, guard and field wires. The sense wires are grounded and allow, using charge division, the measurement of the axial position of charged tracks. The sense wires are radially alternated with guard wires (at -2318V) and also staggered by $\pm 200\mu$m to resolve left/right ambiguity. The guard wires control the gas gain and decouple the sense wires. The field wires produce an homogenous drift field of 1000V/cm. The sense wires are made of 20μm stainless steel and are positioned in the chamber with 40μm rms accuracy. The guard and field wires are made of 152μm diameter aluminium coated with 0.64μm of gold.

A "slow" gas mixture of 90% carbon dioxide and 10% isobutane is used in a single-pass system with the gas at ambient pressure, 25°C and a flow rate of 10litre/hour. With a magnetic field of 1.5T the electron drift velocity is 8.4μm/ns and the Lorentz angle is 7.2°. Since the electron drift velocity is dependent on the gas composition and density, the gas mixture and temperature are regulated. The pressure is left free though constantly monitored. Data for each JDC sector are read out in parallel. The signals are amplified using surface mounted preamplifier cards and digitized using flash ADCs. The digitized signals are amplified using differential amplifiers before the data are written to tape.

The (r,ϕ) resolution has $\sigma = 125\mu$m. For charged pions with a momentum in the range $(0.1 \rightarrow 1.0)$GeV/c, measured from events in which the annihilation occurred at rest, this corresponds to a resolution of $1.5\% \rightarrow 3.0\%$. The beam axis resolution has $\sigma = (7 \rightarrow 8)$mm.

2.5 Electromagnetic Calorimeter

The electromagnetic calorimeter is used to measure the energy and directions of photons. It is a modular system of 1380 thallium doped CsI crystals that cover 95% of the 4π solid angle. The crystals are arranged in a vertex-pointing geometry over the range of polar angles 12° to 168°. Figure 2.4 shows a cross section of a CsI(Tl) module.

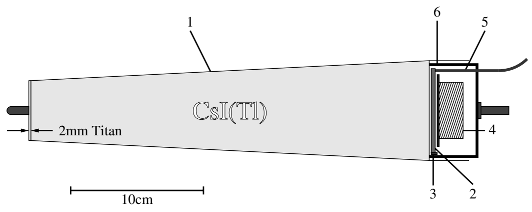

Figure 2.4: Cross section of a CsI(Tl) module: (1) 0.1mm titanium can. (2) printed circuit board. (3) filters for bias and power supplies. (4) preamplifier. (5) light fibre. (6) brass cover (7) wavelength shifter (8) photodiode.

Scintillation light, produced by the interaction of a photon in the crystal, passes through a wavelength shifter before reaching the silicon photodiode where the light is converted into an electrical signal. The wavelength shifter is used to enhance the efficiency of light collection and therefore increase the amplitude of the output signal. A preamplifier is used to enhance the signal further before it leaves the module. Silicon photodiodes, as opposed to photomultiplier tubes, are used to read out the crystal information since the modules are inside the magnet. Each module is encased in a titanium can for protection and to simplify the exchange of modules.

The crystals are 300mm long, (16.1 radiation lengths), thus ensuring that energy loss from the rear of the crystal is less than 1%. The majority of crystals cover 6° in polar and azimuthal angles. Crystals at $\theta < 30^\circ$ and $\theta > 150^\circ$ ie those nearest the beam pipe, have an azimuthal range of 12°. To reduce the amount of material in front of the crystals and therefore the number of photon conversions, the crystals are suspended from the rear.

Signals from the crystal modules are digitized in parallel by two different ADC systems: the FERA[23] system and the 2282[24] system. The FERA system provides a fast readout, necessary for the trigger, and covers the full energy range; $(0 \rightarrow 2000)$MeV. The FERA system has a precision of 1MeV per channel. A precision of 0.1MeV is obtained by the 2282 system which has an energy range of $(0 \rightarrow 400)$MeV. The stability of the readout system is monitored using a lightpulser system. A xenon flash-lamp provides light which is guided into the wavelength shifter of each crystal module via optic fibers. Xenon light is used since it has a similar pulse shape to that of the scintillation light produced by CsI. The lightpulser readout is recorded and checked frequently throughout data taking periods.

The energy resolution, σ_E, of the electromagnetic calorimeter is described by Equation 2.1 where the units of energy are in GeV.

$$\frac{\sigma_E}{E} = \frac{2.5\%}{\sqrt[4]{E}} \tag{2.1}$$

The polar and azimuthal resolution are dependent on energy; for data at rest, they are typically 20mrad. The corresponding mass resolution for the π^0 and η are $\sigma(m_{\pi^0}) = 9.9$MeV and $\sigma(m_\eta) = 16.6$MeV.

2.6 Magnet and Cosmic Ray Counters

The magnet surrounds the electromagnetic calorimeter and wire chambers. It is a conventional solenoid with a maximum field of 1.5T. The solenoid is encased in a box-shaped flux return yoke. When charged-track data are being taken, a 1.5T field is used. A 1.0T field is used when all-neutral data are taken. The field is homogenous over the detection area and symmetrical along the beam axis.

Two identical hodoscopes, made of a 14mm thick segmented plastic scintillator, are used as a cosmic ray telescope. The hodoscopes are positioned outside the magnet, above and below the target. The telescope may be used for test purposes to trigger on cosmic rays when no antiproton beam is available.

2.7 Trigger and Data Acquisition

Signals measured by each detector component are digitized and a trigger is used to filter out unwanted events. Events that are accepted by the trigger are written to tape with the data in a ZEBRA[25] format. The digitization is done by CAMAC and VME modules and a micro-VAX is used to monitor and write data to magnetic tape.

Signals measured by each detector component are digitized using CAMAC and VME modules and sent to a micro-VAX computer where the data are combined, monitored and written to magnetic tape. A schematic diagram of the readout process can be seen in figure 2.5.

A trigger system is used to select various types of events, eg two charged track data, all neutral data, four charged track data etc. The system is designed in three stages in which the complexity of the decision and the decision time increases with each stage. A schematic diagram of the trigger system, including the decision times can be seen in figure 2.6.

The initial trigger level requires an antiproton signal from the beam counters indicating that a $\bar{p}$ enters the liquid hydrogen target but does not reach the veto downstream. The second stage requires a charged particle multiplicity as measured in the PWCs and a specified number of particles measured by the electromagnetic calorimeter. The latter is done using a hardware processor, FACE[26], which includes a variable energy threshold (usually 25MeV) for clusters found in the crystal matrix.

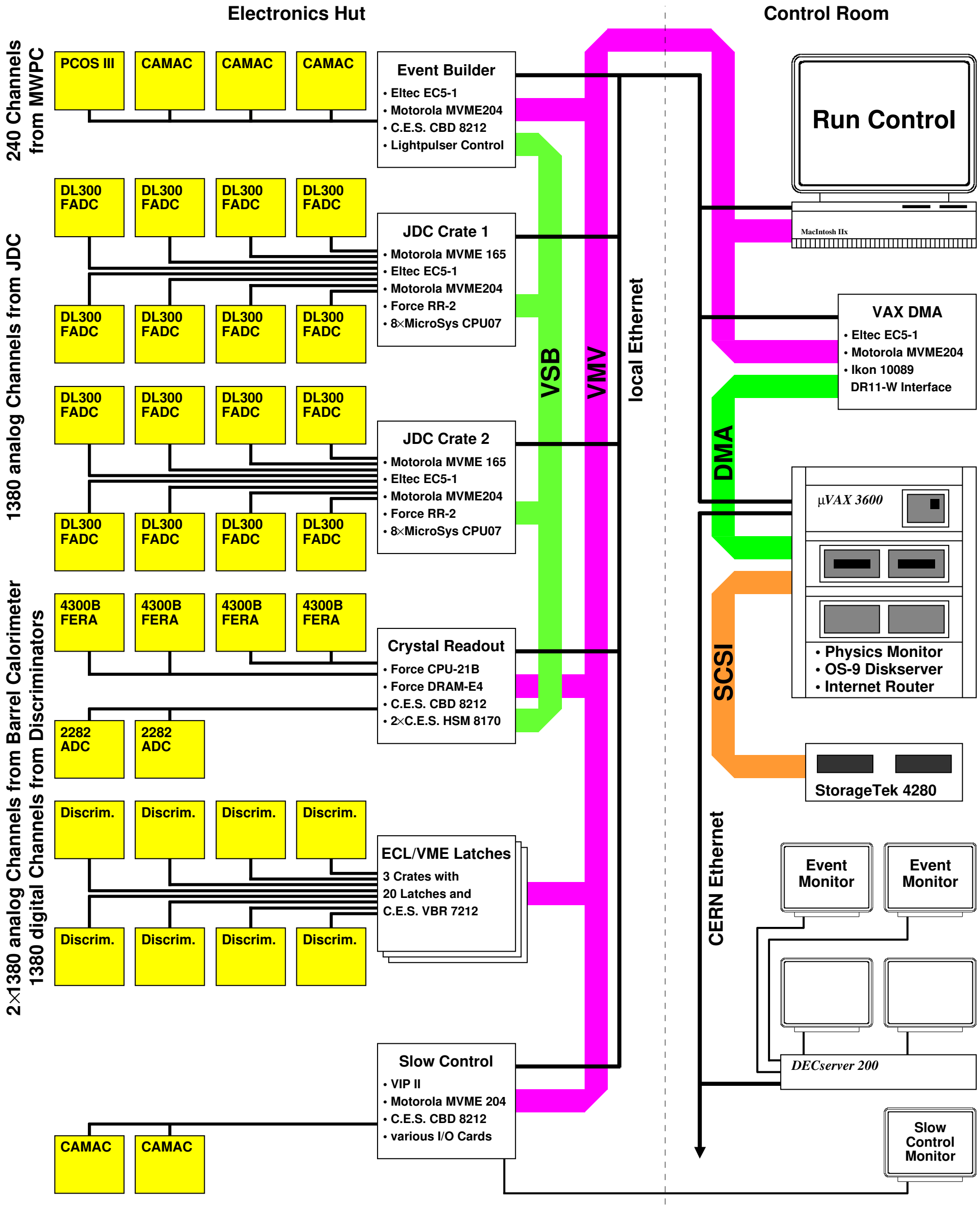

Figure 2.5: Schematic diagram of the detector readout system.

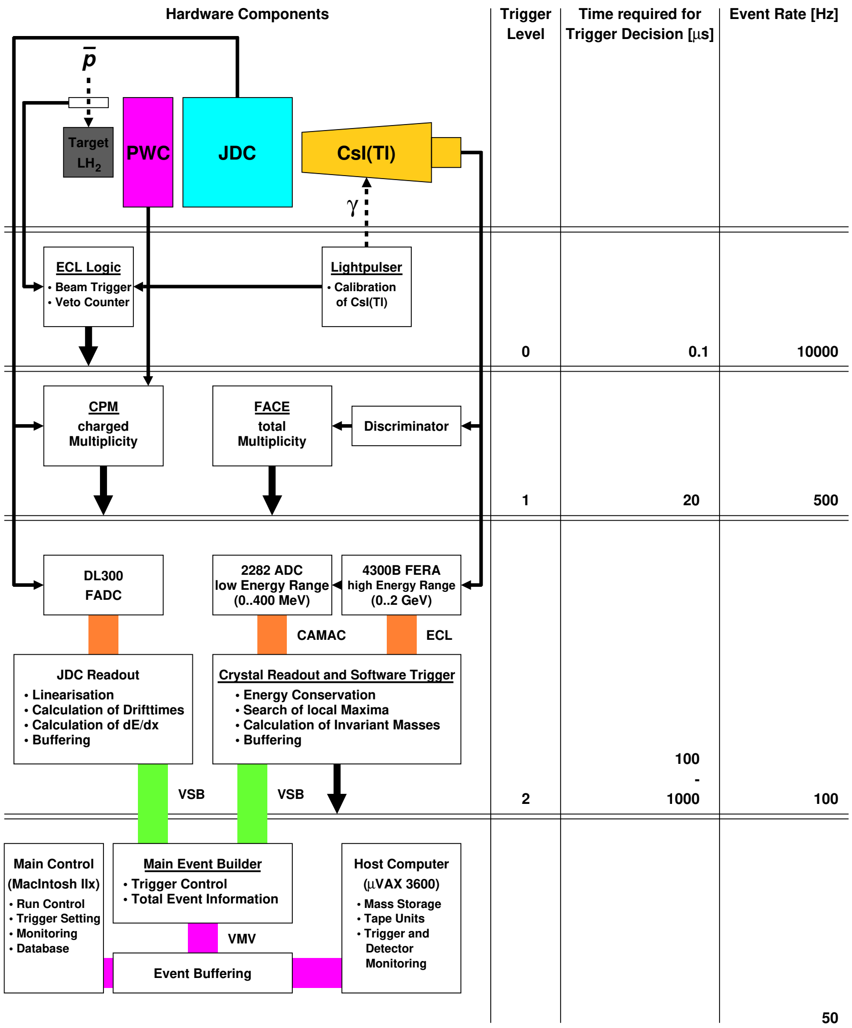

Figure 2.6: Schematic diagram of the trigger system.

Using a 25MeV threshold, the number of FACE clusters measured on-line is equal to the number of particles measured off-line.

The final stage of the trigger includes the JDC and the software trigger. The inner three layers of the JDC may be tested for signals and a charged particle multiplicity can be required. Likewise, the two outer layers may also be used when long charged tracks are wanted. The software trigger uses the crystal information to calculate invariant masses of pairs of clusters. In this way a selection on the number of π^0, η and η' particles may be made, assuming that the η and η' decay into two photons. In addition, the software trigger is used to make an energy window around the ideal event energy.

2.8 Event Reconstruction

The kinematic information of an event is obtained by reconstructing all the final state particles (ie photons and charged particles) from the antiproton-proton annihilation. The reconstruction is done in three separate stages; The raw data from the PWCs and JDC is processed using a Crystal Barrel software package, LOCATER[27][28][29], to provide the kinematic information of the charged particles. The raw data from the electromagnetic calorimeter is processed using BCTRAK[30] to provide the photon kinematic information. The charged track data and the crystal data are then combined, using GTRACK[31] to give a full reconstruction of the event. A more detailed description of each stage can be found in the following sections.

2.8.1 Charged Track Reconstruction.

Raw data from the JDC are converted into drift times and charge amplitudes for each wire signal. The (x,y) coordinates of the signals are calculated using the drift times. Using charge division, the z-coordinates of the hits are calculated from the charge amplitudes. After all the signals are identified and converted into a position in (x,y,z), a search for tracks is made using a circle and helix fit.

Segments of tracks are identified by using two points and successfully predicting a third point. These segments are then combined into tracks and fitted to circles in the x-y (or r-ϕ) plane and straight lines in the r-z plane. The equation used in the circle fit can be seen in Equation 2.2.

$$\frac{r_i}{2qR} + \frac{c^2}{2qRr_i} + sin(\phi_i - \psi_0) = 0 \tag{2.2}$$

R is the distance from the origin to the centre of the circle, ψ_0 is the angle between the tangent at the point of the track's closest approach to the origin and a line parallel to the x-axis. The charge is given by q and the radius of curvature, ρ, is dependent on R; $\rho^2 = R^2 - c^2$. The parameters used in the fit are ψ_0, c^2 and 1/2R. Although equation 2.2 is mathematically unstable, it provides a good first approximation for the parameters involved in the helix fit.

The three equations used in the helix fit can be seen in Equations 2.3, 2.4 and 2.5:

$$x_i = r_0 \cdot sin\psi_0 + \frac{1}{\alpha} \cdot (cos\beta_i + s \cdot sin\psi_0) \tag{2.3}$$

$$y_i = -r_0 \cdot cos\psi_0 + \frac{1}{\alpha} \cdot (sin\beta_i - s \cdot cos\psi_0) \tag{2.4}$$

$$z_i = z_0 - \frac{s \cdot tan\lambda}{\alpha} \cdot (\beta_i - \psi_0 - s \cdot \frac{\pi}{2}) \tag{2.5}$$

Parameters r_0 and z_0 are the distances of the track's closest approach to the origin and α is the reciprocal of the radius of curvature. λ is the dip angle of the helix in the r-z plane. The sign parameter, s, is equal to ± 1. β_i is the azimuthal angle of the point (x_i, y_i, z_i) relative to the centre of the helix. The parameters used in the fit are r_0, z_0, α, tanλ and ψ_0.

From the results of the helix fit the transverse momentum is given by $p_\perp =$ qB/α where B is the magnetic field. The longitudinal momentum is simply $p_{||} =$tan$\lambda \cdot p_\perp$. These are then used to produce a covariance matrix for the momentum components: p_x, p_y, p_z. The matrix is a 3$\times$3 symmetrical matrix with off-diagonal elements and is used in a kinematic fit of tracks to a common vertex. The tracks which are found to start in the first three layers of the JDC are assigned to the first vertex. A search is made for additional vertices for tracks that begin after the third layer of the JDC.

2.8.2 Photon Reconstruction.

The Crystal Barrel software package, BCTRAK[30], is used to process the raw data from the electromagnetic calorimeter and identify energy depositions due to particles ≡ *PED*s. The process begins with the identification of *clusters*. Clusters are pools of energy measured in crystals of the crystal matrix. The minimum energy of a cluster is 10MeV and the crystals belonging to the cluster must share at least one edge with another crystal of the same cluster. The minimum energy of a crystal in a cluster is 1MeV. Once the clusters have been found, the PEDs are identified by finding the local energy maxima within the cluster. The minimum energy of a PED is 20MeV. The majority of clusters contain only one PED. However, with in-flight data, multiple PED clusters become more common due to overlapping clusters. For events including charged tracks, the charged track vertex is used for the PEDs. For all-neutral data, the vertex is assumed to be at the centre of the liquid hydrogen target.

The energy of a single PED cluster, $E_{1.PED}$, is calculated using equation 2.6,

$$E_{1.PED} = E_{cluster} \times F_1(E_{cluster}) \times F_2(\theta_{cluster}) \tag{2.6}$$

where $E_{cluster}$ is the total energy of the cluster. F_1 and F_2 are photon correction factors dependent on the cluster energy and the photon angle respectively. The energy correction factor is required to compensate for the non-linear response for low photon energies (<50MeV). The correction factor dependent on angle is used to compensate for energy leakage from crystals close to the beam line. The energy of a PED, E_{NPED}, from a multiple PED cluster is calculated using equation 2.7.

$$E_{NPED} = \frac{E_9}{\sum_{i=1}^{N} E_{9i}} \cdot E_{cluster} \times F_1(E_{cluster}) \times F_2(\theta_{cluster}) \tag{2.7}$$

where E_9 is the sum of the energy from the PED's central and eight neighboring crystals. The total energy of the cluster is $E_{cluster}$ and N is the number of PEDs within the cluster.

The position of the PED is calculated using the energy depositions and direction cosines of the PED's central and eight neighboring crystals. It is basically the "Centre of Gravity" of the energies, but the energies are weighted according to the crystal position. Further details of the calculation can be found in reference [27].

The two photons from a high energy π^0 have a small opening angle and may produce a cluster containing two PEDs. These pions can be easily identified using the invariant mass (or *shower* mass) of the cluster. The shower mass of a cluster may be calculated using equation 2.8.

$$M = \sqrt{(\sum E_i)^2 - (\sum \vec{p_i})^2} \tag{2.8}$$

Here, E_i is the energy of the i^{th} crystal in the cluster and $\vec{p_i}$ is the corresponding momentum vector. A comparison of the shower masses for single PED clusters and two PED clusters can be seen in figure 2.7.

2.8.3 Global Reconstruction.

The task of the GTRACK[31] software package is to combine the charged track and crystal data and produce data banks for each particle. Using the charged track information, the tracks are extrapolated and the point of intersection with the crystals is calculated. Any PEDs found in the intersection region are associated with the charged track and classed as a *matched* PED. No more than one PED per track may be matched. The remaining *unmatched* PEDs are assumed to be due to either photons or split-offs: extra PEDs whose nature will be explained in the event selection chapter. A typical unmatched PED multiplicity for 0-prong data can be seen in figure 2.8. Here one can see a slight increase in particle multiplicity as the event energy increases from 2.46GeV to 3.09GeV.

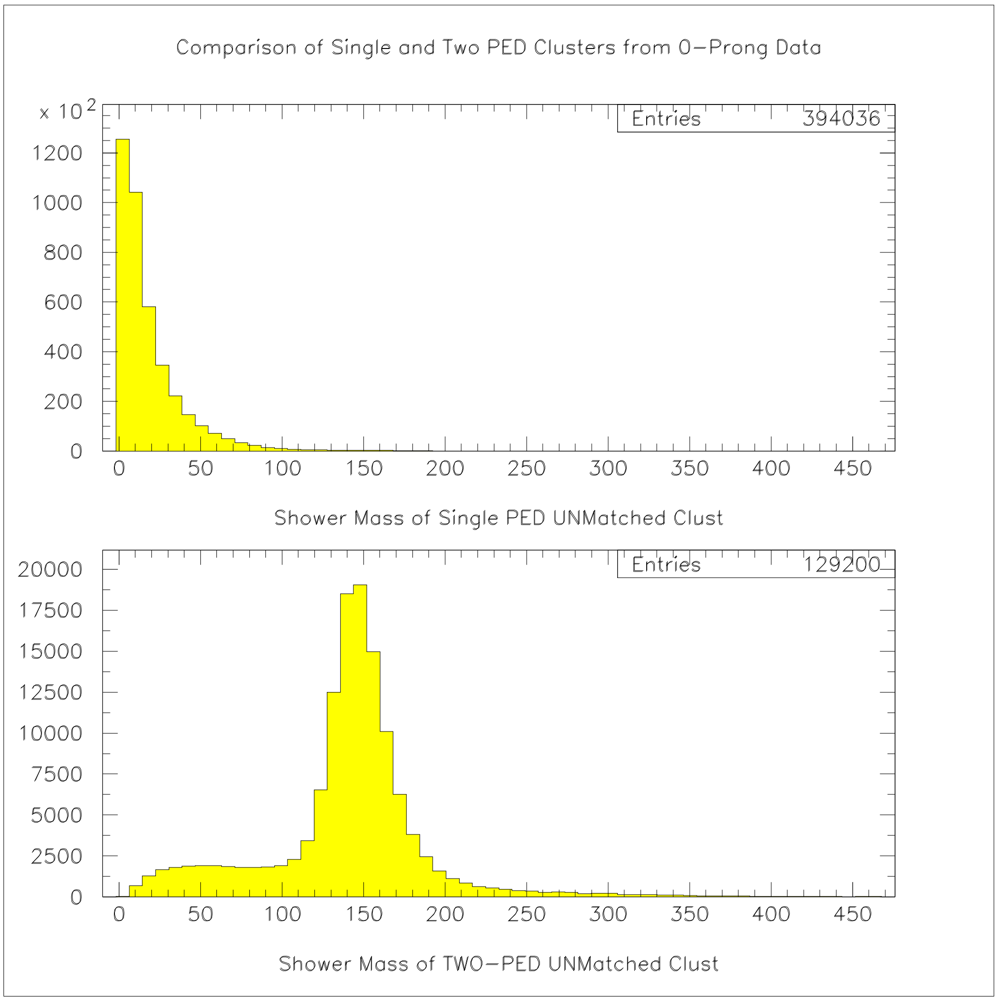

Figure 2.7: Shower masses for single and two PED clusters. The majority of two PED clusters are caused by two photons with a small opening angle from the decay of a high energy π^0.

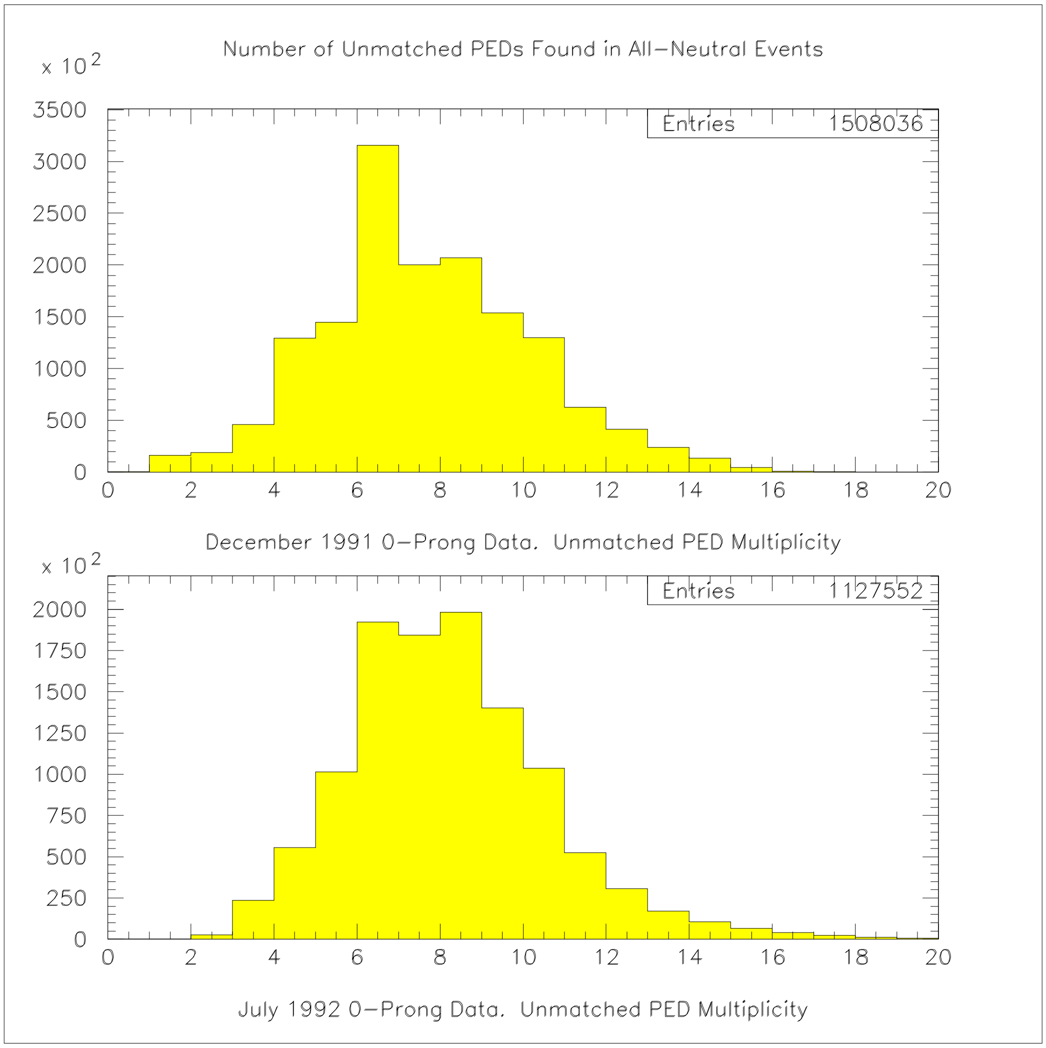

Figure 2.8: Unmatched PED multiplicities for (top) December 91 0-Prong data and (bottom) July 92 0-Prong data. The antiproton momenta were 1.20Gev/c and 1.94Gev/c respectively.

2.9 Calibration

Calibration of the JDC information is done in two parts to obtain the position of hits along a track for the z-axis and the (r,ϕ) positions. The z-coordinate of a hit is calculated using the charge division method seen in equation 2.9 and the wires are calibrated individually:

$$z = z_0 + z_L \cdot \frac{A_+ - \alpha A_-}{A_+ + \alpha A_-} \tag{2.9}$$

The position of the wire centre is given by z_0 and Z_L is half of the wire's electrical length. The measured current amplitudes are A_+ and A_- with α being the relative gain between the two electrical chains. The calibration constants determined for each wire are z_0, Z_L and α. The constants are determined using triggered data in which the trigger requires four long charged tracks with no magnetic field from the magnet. Tracks with at least 10 layers are selected and fitted to straight lines with a common vertex in the target volume. This provides a large sample of measured amplitudes and fitted z-coordinates. This procedure is repeated varying z_0, Z_L and α. All the measured amplitudes and fitted z-coordinates are then fitted to give the best value of z_0, Z_L and α.

The r-ϕ hit positions are calculated using drift times and the calibration procedure uses two-body charged final states (ie $\pi^+\pi^-$ and K^+K^-). For data at rest, the particles are collinear and the two tracks may be treated as a single helix: this provides a strong constraint on the event selection. For in-flight data, two body events are used and a Lorentz transformation into the $\bar{p}p$ rest frame is made to get a single helix. Apart from providing a single helix, the collinear events also ensure a monoenergetic and therefore peaked momentum distribution.

An electrostatic simulation program, GARFIELD[32], is used to generate a set of look-up tables containing drift times to individual wires (for several different drift velocities) and the associated pair of hit coordinates. The variations in drift velocity are due to changes in atmospheric pressure and gas temperature. In the charged track reconstruction, the hit coordinates are determined by a linear interpolation of the look-up table values. The r-ϕ calibration procedure consists of repeatedly reconstructing the charged tracks and calculating the momentum distribution of the collinear particles whilst varying the interpolation factor. The optimal drift time table is found when the width of the momentum peak is at a minimum.

The calibration of the crystal data is required to convert the calorimeter's digitized pulse heights into energy. The calibration is done in two parts: precalibration and the main calibration. The precalibration uses charged track data (with no magnetic field). High energy charged pions may traverse the entire length of a crystal and only lose energy via electromagnetic interactions. For pions this is a monoenergetic loss of 170MeV which is used as a precalibration point for each crystal.

The main calibration uses all-neutral data in which the events have less than eight PEDS and an energy window cut. When the invariant mass of unmatched PED pairs (all combinations) are plotted, the most distinctive feature of the profile is a π^0 peak. The peak arises from the large number of π^0s decaying into two photons. The mean of the peak, ie the π^0 mass, is used to calibrate the crystal data.

An invariant mass of unmatched PED pairs graph is created for each of the 1380 crystals. When, say, crystal number 1 is the central crystal of an unmatched PED in an event, all invariant mass combinations of unmatched PED pairs *that include the PED of crystal 1* are plotted for that particular event in the histogram of crystal number 1. Due to the large number of π^0s from $\bar{p}p$ annihilations it is likely that one of these pairs form a π^0. The remaining pair combinations form a combinatorical background to the resulting π^0 peak. All 1380 histograms are filled in the same manner and are fitted with a Gaussian (for the π^0 peak) and a Chebyshev polynomial (for the combinatorical background).

The position of the π^0 peak is most sensitive to the precalibration of the crystal associated with the histogram since it is included in every entry. The effect of other crystal's precalibration is less since they average out and only contribute to the width of the peak. From the peak position, new calibration factors can be calculated and the process iterated until all the π^0 peaks are in the correct position.

Chapter 3

Data Selection

3.1 Introduction

In order to analyse the $\pi\pi\pi\eta$ final state from antiproton-proton annihilation, four separate data sets have been used:-

Run Period Date	$\bar{p}$ Momenta (Gev/c)	Trigger Type	Events Accumulated
December 91	1.20	Special	1.998M
December 91	1.20	0-Prong	1.599M
July 92	1.94	2-Prong	4.261M
July 92	1.94	0-Prong	1.469M

Table 3.1: Data Sets Used in Analysis.

In-flight data, as opposed to at-rest data, were used since they have the advantage of a larger range of phase space. The data taken in December 1991 were the first large in-flight data set to be accumulated by the Crystal Barrel. The July 1992 data were the first large data set to be taken with an antiproton momentum of 1.94GeV/c. Several different triggers were used in the selection of events to be recorded, though these can be fundamentally divided into two groups: the all-neutral or 0-prong data in which there are no charged particles in the product of the annihilation and the 2-prong data in which two charged particles were measured. A more detailed explanation of the different triggers can be found in the following section.

3.2 Triggers Used in the Data Taking

The data sets used in this analysis were accumulated using the following triggers:-

- **0-Prong**: For an event to be accepted and written to tape, the event had to sequentially pass the following conditions:-
  - No signals (indicating a charged particle) from the PWCs or the JDC.
  - The number of FACE clusters must be greater than one.
  - The sum of the energy measured in the electromagnetic calorimeter must be within a suitable range defined within the software trigger.
- **2-Prong**: For an event to be accepted and written to tape, the event had to sequentially pass the following conditions:-
  - Signals from the PWCs and JDC must indicate that two charged particles come from the antiproton-proton annihilation.
  - The number of FACE clusters must be one or more.
- **Special**: This trigger was designed to reject events that were obviously not of the form $\bar{p}p \rightarrow \pi^+\pi^-\pi^0\eta$ where the charged pions are considered to be stable ie they do not decay in the detector. (The decay mode of the η into two photons (like that of the π^0) was chosen due to its large branching ratio and the event reconstruction efficiency.) The decay of the η into $3\pi^0$ produces six photons, as opposed to two, and therefore the probability of one or more photons going undetected is increased. For an event to be accepted and written to tape, the event had to pass sequentially the following conditions:-

– Signals from the PWCs and JDC must indicate that two charged particles come from the antiproton-proton annihilation.

– The number of FACE clusters must be larger than 4 and less than 9.

– The sum of the energy measured in the electromagnetic calorimeter must be within a suitable range defined within the software trigger.

– The software trigger must find at least one π^0.

The design of the special trigger was limited by the on-line measurement of photons. The on-line measurement of the photon multiplicity had three main problems. The first of these was due to the FACE cluster-recognition being only accurate to ± 1 PED. The second problem was due to charged particles depositing energy in the electromagnetic calorimeter. On-line, these PEDs cannot be associated with the charged particles and therefore are seen as being due to photons. The third problem was due to *split-offs* where an extra PED was measured.

Electromagnetic split-offs arise when the shower, produced in the crystals by the interaction of a photon, does not evolve uniformly and splits into two. Off-line, these are seen as two overlapping PEDs and are easily identified by the ratio of the energy of the parent PED to the split-off PED. *Hadronic split-offs* can occur when a charged particle interacts in a crystal. A nuclear interaction can cause the isotropic production of a neutral particle which then may be measured in the electromagnetic calorimeter as a PED. Off-line, hadronic split-offs are more difficult to identify. Assuming that all the products of the annihilation are measured, then events with hadronic split-offs are found to have excess energy. This is because the charged particle's energy is measured twice; from the JDC information and from the split-off's energy in the electromagnetic calorimeter. The hadronic split-offs can then be identified by using energy-momentum conservation and choosing the PED which has a similar energy-momentum to that of the measured excess.

The software trigger included a mask for the multiplicity of π^0, η and $\eta'(958)$ particles. The number of π^0s required was one or more. A more stringent requirement of only one π^0 would have rejected many of the desired events. This is because the PED pair combinations from photons, charged particles and split-offs often produce an invariant mass in the π^0 mass region. The inclusion of an η particle multiplicity requirement was tested and found to slow the event rate down to an unacceptable level below 5Hz. As with the π^0 search, the combinatorics were large enough to produce a PED pair combination that falls within the η mass region to the extent that virtually every event was found to have at least one η particle. Therefore, no requirement on the η or $\eta'(958)$ multiplicity was made.

The rate of events being accepted by the trigger and written to tape can be seen in Table 3.2.

Trigger Type	Number of $\bar{p}$ at $Si_{2\to5}$	Event Rate Hz
Dec 91 0-Prong	153K	10
Dec 91 Special	131K	15
Jul 92 0-Prong	110K	8
Jul 92 2-Prong	62K	24

Table 3.2: Typical Event Rates for the Different Triggers.

The intensity of the antiproton beam was different for each trigger since the intensity was limited by the JDC. At high $\bar{p}$ intensities the induced current on the JDC wires can cause sparks and therefore damage to the chamber. The wire currents are also sensitive to the stability and precision of the beam steering. 200nA was used as a safe upper limit for the working chamber. In the taking of all-neutral data the JDC is only used as a veto counter and the charged track resolution is not significant. Therefore it is possible to reduce the high voltage (and hence sensitivity) and increase the beam intensity.

3.3 Event Selection

The selection of $\bar{p}p \to \pi^+\pi^-\pi^0\eta$ and $\bar{p}p \to \pi^0\pi^0\pi^0\eta$ events was done in several stages. From the raw data, the events were reconstructed, analysed and written to data summary tapes (DSTs) provided they passed the analysis cuts, ie the event fulfilled certain characteristics of being an $\pi^+\pi^-\pi^0\eta/\pi^0\pi^0\pi^0\eta$ event. This process was repeated with increasingly sophisticated and constraining cuts (to produce DST$'$, DST$''$ etc) until the data samples contained only $\pi^+\pi^-\pi^0\eta/\pi^0\pi^0\pi^0\eta$ events. The selection procedure for $\pi^+\pi^-\pi^0\eta$ events from the December 91 special trigger data was identical to that for the July 92 2-Prong data set. The selection procedure for $\pi^0\pi^0\pi^0\eta$ events was the same for both the December 91 and July 92 0-Prong data sets. A full description of the cuts for both the charged and neutral channels can be found later in this chapter.

Two Crystal Barrel software packages were used to identify split-offs. The electromagnetic split-off suppression package[33] uses the ratio of PED energies for 2-PED clusters to identify split-offs which are generally of low energy (< 50MeV). The opening angle between the two PEDs is used to avoid identifying PEDs from a fast π^0 as split-offs: photons from fast π^0s tend to have a small opening angle and are measured as two PEDs in the same cluster.

CBDROP[34] was used to identify the hadronic split-offs and can be considered in two parts. The first part makes a cut using the quality of the charged tracks in an event. To judge whether a charged track has been well measured, CBDROP uses the following criteria:-

- The total charge of an event must be zero.
- The tracks must traverse at least 10 layers of the JDC.
- Both tracks must have a good fit to a helix.
- Both tracks must begin in the first three layers of the JDC.

- The vertex convergence must be good.

For this analysis, the first four criteria were used.

The second part of CBDROP is the identification of hadronic split-offs. This uses a kinematic fit to the ideal energy and momentum of the event. Initially, all particles measured in an event are used in the kinematic fit to produce a confidence level, CL_0. This is repeated but with one unmatched PED ignored or 'dropped'. All combinations of a single dropped unmatched PED are tried and the combination that gives the highest confidence level, CL_1, is retained. This procedure is repeated again but with two unmatched PEDs dropped. The best combination from dropping two unmatched PEDs, with a confidence level, CL_2, is retained and compared with CL_0 and CL_1. The highest confidence level then indicates whether there are zero, one or two split-offs in an event. For this analysis, the maximum number of unmatched PEDs dropped and hence split-offs ignored was two. An example of a typical confidence level distribution and hadronic split-off multiplicity can be seen in Figure 3.1.

The confidence level distribution gives information on the magnitude of the errors used in the kinematic fit. The confidence level distribution seen in Figure 3.1 is fairly flat after 20%. This indicates that the errors for the measured parameters used in the fit are the correct size. A distribution that rises as the confidence level tends to 100% indicates that the errors are too large. If the errors were too small, the distribution would have a negative slope.

To maximize the number of events with a specified ideal photon multiplicity and save CPU time, the kinematic fitting can be steered to attempt only fits that would leave the ideal number of photons.

CBKFIT[35] was used for the advanced kinematic fitting. The package can fit all-neutral and 2-prong data and begins with a fit to the ideal energy-momentum of the event. The ideal total energy of events, used in the kinematic fits by CBDROP and CBKFIT, for a $\bar{p}$ of momentum 1.20GeV/c was 2.462GeV. The energy used

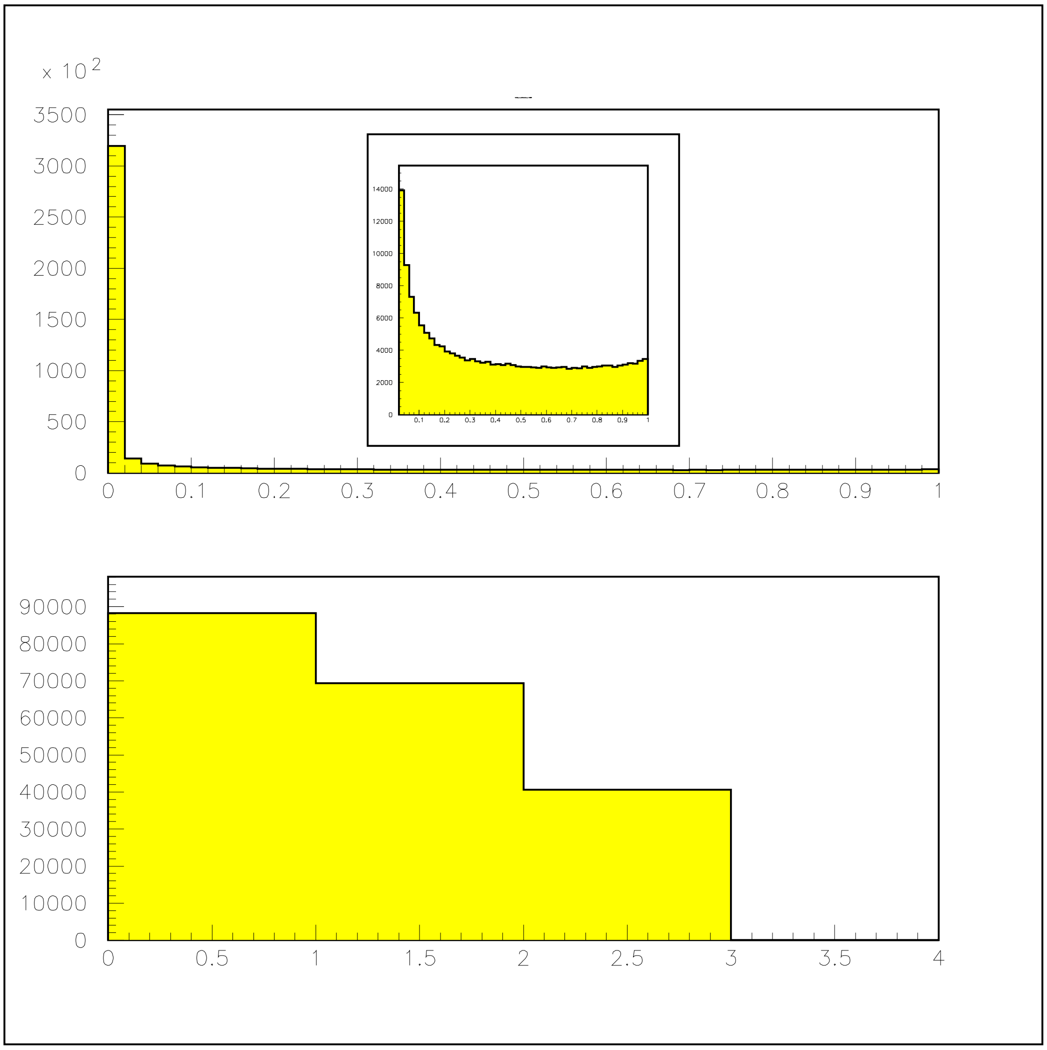

Figure 3.1: Top: Confidence level distribution from CBDROP. Inset: The same confidence level distribution ignoring the spike at 0%. Bottom: Typical hadronic split-off multiplicity for events with up to two split-offs.

for events from the 1.94GeV/c data sets was 3.093GeV. The package is able to fit data to specific channels eg $\pi^+\pi^-\pi^0\eta$ and for channels with identical particles, all combinatorial cases are calculated and tested.

The measured parameters used in fitting photons are ϕ, θ and $\sqrt{E}$. These parameters were chosen since they are the least correlated and produce the most Gaussian-like error distribution. Similarly for charged particles the equivalent parameters are ψ, $\tan(\lambda)$ and $1/P_{xy}$ where λ is $(\pi/2$ - $\theta)$ and P_{xy} is the transverse momentum. For each attempted fit the package produces a *pull* for each parameter and a confidence level. The pull value is proportional to the difference between the measured and ideal parameter value. An example of a pull distribution can be seen in Figure 3.2.

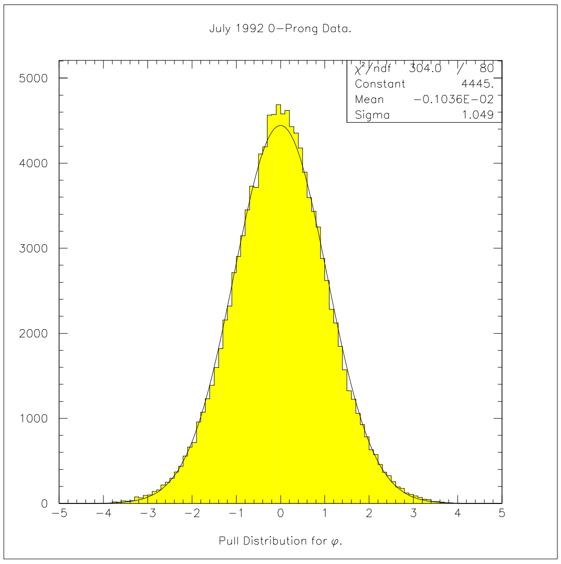

Figure 3.2: A typical pull distribution for the parameter ϕ fitted with a Gaussian distribution.

The mean and sigma, σ, of a pull distribution gives information about the magnitude and associated error for a particular parameter. The mean indicates whether the magnitude of the parameter measurement is, on average, too high or low. Likewise, σ indicates whether the errors have been underestimated or are too large. In an ideal situation where the measured parameters are independent, the data set is completely pure and the error magnitudes are known, the pull distributions for events with a confidence level greater than 0% should be Gaussian with a mean centered on zero and a σ equal to one. A distribution with a mean greater than zero indicates that the parameter has consistently been measured with a lower value than that of the real or ideal value. A mean less than zero indicates that the parameter measurement has been consistently too high. When the errors of a parameter are underestimated, the σ of the distribution is greater than one. A σ less than one indicates that the parameter errors are too large.

Using the confidence level and pull distributions, scaling factors for the parameters and errors were used to ensure that the mean and σ for the pulls were close to zero and one respectively. For real data, the fit to $\pi^+\pi^-\pi^0\gamma\gamma/\pi^0\pi^0\pi^0\gamma\gamma$ was used to get the confidence level and pulls. This fit was used for the following reasons: the process $\bar{p}p \to \pi\pi\pi\gamma\gamma$ has a large branching ratio and so a small sample of data can be used to get large statistics. The events must have passed the energy-momentum fit to be included in the $\pi\pi\pi\gamma\gamma$ fit. The energy-momentum fit rejects most of the large number of events in which one or more particles went undetected. These events cause a bias in the pulls since they lower the mean energy of the events. The scaling factors used and the resulting confidence level and pull distributions for each kinematic fit can be found in Appendix A.

For the $\pi^+\pi^-\pi^0\eta$ final state, the charged pions were assumed to be stable and did not decay whilst in the detector. For both $\pi^+\pi^-\pi^0\eta$ and $\pi^0\pi^0\pi^0\eta$ final states the π^0 and η particles were identified by their decay into two photons. Therefore, assuming that no split-offs occurred or particles went undetected, the charged mode of $\pi\pi\pi\eta$ has an ideal final state of two charged pions and four photons. However, the process $\bar{p}p \to \pi^+\pi^-\pi^0\pi^0$ also has a final state of two charged pions and four photons and this has to be considered as a possible source of background when the four photons from $\pi^+\pi^-\pi^0\pi^0$ can be paired to form an η and π^0. The neutral mode of $\pi\pi\pi\eta$ has eight photons in its ideal final state. Other processes with an eight photon final state and hence possible sources of background are $\bar{p}p \to \pi^0\pi^0\pi^0\pi^0$ and $\bar{p}p \to \omega\omega\pi^0$ where both ω particles decay into $\pi^0\gamma$. To ensure the purity of the $\pi\pi\pi\eta$ data samples, events were rejected if they could be kinematically fitted to these background processes.

3.3.1 Analysis Cuts for $\bar{p}p \to \pi^+\pi^-\pi^0\eta$

In order to obtain a pure sample of $\bar{p}p \to \pi^+\pi^-\pi^0\eta$ events, the events read into the analysis software had to pass the following cuts. The reconstruction software used to do this was: CBOFF 1.22/00, LOCATER 1.52/04, BCTRAK 2.00/03, GTRACK 1.21/099 and CBKFIT 2.09/04.

- Cut1: The event must have two charged tracks.
- Cut2: The number of unmatched PEDs must be greater than 3 and less than 7. This allows for up to 2 split-off PEDs.
- Cut3: Edge crystal cut. The event must not have an unmatched PED whose central crystal (ie the crystal with the maximum energy in the PED) is an edge crystal that lies close to the beam line. This cut is used to maintain the high electromagnetic energy resolution of the detector. PEDs with an edge crystal at their centre have a poor energy resolution due to energy leaking out of the side of the crystal into the beam pipe.
- Cut4: The sum of the charge from the two charged particles must be zero.
- Cut5: CBDROP: The length of the charged tracks must span at least ten radial layers of the JDC and the tracks point to a common vertex. The event must fulfill a kinematic fit to the ideal energy and momentum, with a confidence level greater than 1%. From the hadronic split-off recognition, the event must have 4 photons and less than three split-offs.

- Cut6: The event must fulfill a fit to the hypothesis $\pi^+\pi^-\pi^0\gamma\gamma$ with a confidence level greater than 1%.

- Cut7: The event must fulfill a fit to the hypothesis $\pi^+\pi^-\pi^0\eta$ with a confidence level greater than 1%.

- Cut8: The event must NOT be able to fit to the $\pi^+\pi^-\pi^0\pi^0$ hypothesis, the resulting confidence level must be less than 1%.

3.3.2 Analysis Cuts for $\bar{p}p \rightarrow \pi^0\pi^0\pi^0\eta$

In order to obtain a pure sample of $\bar{p}p \rightarrow \pi^0\pi^0\pi^0\eta$ events, the events read into the analysis software had to pass the following cuts. The reconstruction software used to do this was: CBOFF 1.22/00, LOCATER 1.52/04, BCTRAK 2.00/03, GTRACK 1.21/099 and CBKFIT 2.09/04.

- Cut1: The event must not have any charged tracks.

- Cut2: The event must have 8 unmatched PEDs.

- Cut3: Edge crystal cut. As above.

- Cut4: The event must not have any electromagnetic split-offs.

- Cut5: The event must fulfill a z-vertex fit with a confidence level greater than 0.0001%. The position of the $\bar{p}$ annihilation along the beam line, (z-axis), has a flat distribution along the target. Without the aid of charged tracks to point to a vertex, a kinematic fit is used to find the optimum position. The position of the vertex in the x-y plane is assumed to be at the centre of the target since the beam was steered to the centre of the target with high precision. This cut was deliberately loose since the fit was only used to find the best position of the vertex. A full energy-momentum fit with a more stringent confidence level cut is included in the next fit.

- Cut6: The event must fulfill a fit to the hypothesis $\pi^0\pi^0\pi^0\gamma\gamma$ with a confidence level greater than 1%.
- Cut7: The event must fulfill a fit to the hypothesis $\pi^0\pi^0\pi^0\eta$ with a confidence level greater than 1%.
- Cut8: The event must NOT fulfill a fit to the hypothesis $\pi^0\pi^0\pi^0\pi^0$ ie the confidence level must be less than 1%.
- Cut9: The event must NOT fulfill a fit to the hypothesis $\omega\omega\pi^0$ in which both ω particles decay into a $\pi^0\gamma$. For the event to be accepted, the confidence level from the fit must be less than 1%.

3.4 Monte Carlo Data

Monte Carlo data have been generated and used to give an approximate simulation of the phase space for the pions and η in the $\pi\pi\pi\eta$ final state. The data were generated using a CERN software package; GEANT 3.15 and GCB 4.06/07, and analysed using identical reconstruction and analysis software as that for the real data. By comparing the kinematics of the generated $\pi\pi\pi\eta$ particles with the same reconstructed data set, the geometric effects of the detector and the reconstruction efficiency can be evaluated.

The vertex of the annihilation was generated with a Gaussian distribution with a 2cm sigma to simulate the distribution of real in-flight annihilations within the liquid hydrogen target. Since the annihilations occurred in-flight, the resulting particles are boosted along the beam axis and angular momentum effects may also bias the particles along the beam line direction. The latter effect was not included in the simulation since there are a large number of possible initial states in this energy region. The decays of the η and π^0 were not left free; both particles were forced to decay via two photons 100% of the time.

Table 3.3 shows the number of events generated for the various data sets.

Monte Carlo Data Set	$\bar{p}$ Momenta (Gev/c)	Events Accumulated
MC $\bar{p}p \rightarrow \pi^+\pi^-\pi^0\eta$	1.20	203K
MC $\bar{p}p \rightarrow \pi^0\pi^0\pi^0\eta$	1.20	113K
MC $\bar{p}p \rightarrow \pi^+\pi^-\pi^0\pi^0$	1.20	100K
MC $\bar{p}p \rightarrow \pi^0\pi^0\pi^0\pi^0$	1.20	100K
MC $\bar{p}p \rightarrow \pi^+\pi^-\pi^0\eta$	1.94	150K
MC $\bar{p}p \rightarrow \pi^0\pi^0\pi^0\eta$	1.94	95K
MC $\bar{p}p \rightarrow \pi^+\pi^-\pi^0\pi^0$	1.94	100K
MC $\bar{p}p \rightarrow \pi^0\pi^0\pi^0\pi^0$	1.94	95K

Table 3.3: Monte Carlo data sets generated.

3.5 Selection Efficiency

Tables 3.4, 3.5, 3.6 and 3.7 show the loss of events for real and Monte Carlo data as they pass through the analysis. The number of lost events is given in terms of the percentage of events that failed a particular cut, relative to the number of events going into the cut.

3.5.1 Comparison of the Losses for the 2-Prong Data Sets

The July 1992 2-prong data set loses relatively more events in the initial cuts (up to the energy-momentum fit of CBDROP) than the December 1991 special trigger data. This can be explained by the differences in event energy and trigger between the two data sets. The July data set loses more events in the simple two charged track cut due to an inefficiency in the charged track multiplicity trigger during the run period. The unmatched PED multiplicity cut was more effective for the July data set since the trigger accepted any number of FACE clusters whilst the December

Selection of $\bar{p}p \rightarrow \pi^+\pi^-\pi^0\eta$ at 1.20GeV/c				
	Real Data		MC Data	
Number of Events Analysed	1 997 541		202 993	
Cut	Passed	Lost(%)	Passed	Lost(%)
2 Charged particles	1 491 341	25.3	138 136	32.0
$4 \rightarrow 6$ Unmatched PEDs	971 832	34.8	112 509	18.6
No Edge Crystal PEDs	631 476	35.0	90 341	19.7
$\sum$ Charge $= 0$	563 170	10.8	86 653	4.1
CBDROP: Track Quality	505 135	10.3	70 019	19.2
CBDROP: Energy-Momentum CL $> 1\%$	190 773	62.2	51 380	26.6
CBKFIT: Energy-Momentum CL $> 1\%$	180 289	5.5	50 601	1.5
CBKFIT: $\pi^+\pi^-\pi^0\gamma\gamma$ CL $> 1\%$	171 933	4.6	47 382	6.4
CBKFIT: $\pi^+\pi^-\pi^0\eta$ CL $> 1\%$	24 000	86.0	44 354	6.4
CBKFIT: No fit to $\pi^+\pi^-\pi^0\pi^0$ CL $< 1\%$	19 918	17.0	44 116	0.5

Table 3.4: Loss of events as they pass through the analysis cuts for events of the form $\bar{p}p \rightarrow \pi^+\pi^-\pi^0\eta$ with a $\bar{p}$ momentum of 1.20GeV/c. The real data is from the special trigger data set of December 1991.

Selection of $\bar{p}p \rightarrow \pi^+\pi^-\pi^0\eta$ at 1.94GeV/c				
	Real Data		MC Data	
Number of Events Analysed	4 260 998		150 168	
Cut	Passed	Lost(%)	Passed	Lost(%)
2 Charged particles	2 085 301	51.0	91 890	38.8
$4 \rightarrow 6$ Unmatched PEDs	883 911	57.6	71 191	22.5
No Edge Crystal PEDs	525 161	40.6	51 514	27.6
$\sum$ Charge $= 0$	443 881	15.5	47 886	7.1
CBDROP: Track Quality	286 598	35.4	35 518	25.8
CBDROP: Energy-Momentum CL $> 1\%$	100 297	65.0	24 620	30.7
CBKFIT: Energy-Momentum CL $> 1\%$	94 367	5.9	24 129	2.0
CBKFIT: $\pi^+\pi^-\pi^0\gamma\gamma$ CL $> 1\%$	89 138	5.5	22 380	7.3
CBKFIT: $\pi^+\pi^-\pi^0\eta$ CL $> 1\%$	13 255	85.1	20 648	7.7
CBKFIT: No fit to $\pi^+\pi^-\pi^0\pi^0$ CL $< 1\%$	11 916	10.1	20 554	0.5

Table 3.5: Loss of events as they pass through the analysis cuts for events of the form $\bar{p}p \rightarrow \pi^+\pi^-\pi^0\eta$ with a $\bar{p}$ momentum of 1.94GeV/c. The real data is from the 2-prong trigger data of July 1992.

Selection of $\bar{p}p \rightarrow \pi^0\pi^0\pi^0\eta$ at 1.20GeV/c				
	Real Data		MC Data	
Number of Events Analysed	1 598 707		112 699	
Cut	Passed	Lost(%)	Passed	Lost(%)
No Charged particles	1 508 036	5.7	102 963	8.6
8 Unmatched PEDs	206 811	86.3	51 189	50.3
No Edge Crystal PEDs	131 956	36.2	35 066	31.5
No EM split-offs	123 771	6.2	32 897	6.2
CBKFIT: Z-Vertex Fit CL $> 1\times10^{-4}$%	65 544	47.0	28 445	13.5
CBKFIT: Fit to $3\pi^0\gamma\gamma$ CL $> 1\%$	47 937	26.9	24 992	12.1
CBKFIT: Fit to $3\pi^0\eta$ CL $> 1\%$	10 738	77.6	22 846	8.6
CBKFIT: No fit to $4\pi^0$ CL $< 1\%$	7 432	30.8	22 360	2.1
CBKFIT: No fit to $\omega\omega\pi^0$ CL $< 1\%$	6 838	8.0	20 688	7.5

Table 3.6: Loss of events as they pass through the analysis cuts for events of the form $\bar{p}p \rightarrow \pi^0\pi^0\pi^0\eta$ with a $\bar{p}$ momentum of 1.20GeV/c. The real data is from the 0-prong trigger data of December 1991.

Selection of $\bar{p}p \rightarrow \pi^0\pi^0\pi^0\eta$ at 1.94GeV/c				
	Real Data		MC Data	
Number of Events Analysed	1 469 109		95 419	
Cut	Passed	Lost(%)	Passed	Lost(%)
No Charged particles	1 127 552	23.3	87 401	8.4
8 Unmatched PEDs	198 223	82.4	38 331	56.1
No Edge Crystal PEDs	101 544	48.8	22 543	41.2
No EM split-offs	87 923	13.4	20 336	9.8
CBKFIT: Z-Vertex Fit CL $> 1\times10^{-4}\%$	57 546	34.6	17 029	16.3
CBKFIT: Fit to $3\pi^0\gamma\gamma$ CL $> 1\%$	47 168	18.0	14 642	14.0
CBKFIT: Fit to $3\pi^0\eta$ CL $> 1\%$	11 076	76.5	13 407	8.4
CBKFIT: No fit to $4\pi^0$ CL $< 1\%$	7 598	31.4	13 212	1.5
CBKFIT: No fit to $\omega\omega\pi^0$ CL $< 1\%$	6 933	8.8	11 864	10.2

Table 3.7: Loss of events as they pass through the analysis cuts for events of the form $\bar{p}p \rightarrow \pi^0\pi^0\pi^0\eta$ with a $\bar{p}$ momentum of 1.94GeV/c. The real data is from the 0-prong trigger data of July 1992.

trigger only accepted the events with a FACE cluster multiplicity similar to that of the ideal for $\bar{p}p \rightarrow \pi^+\pi^-\pi^0\eta$ events. The higher $\bar{p}$ momentum of the July data caused the products of the annihilations to be more biased towards the beam line than for the December data. This bias produces more events in which the central crystal of PEDs is an edge crystal, hence more events are lost to the edge-crystal cut.

The July data set loses more events due to the sum of charge cut. This can be understood in terms of the reconstruction of the charged tracks and the average energy of the charged pions from the July data being higher than that of the December data. High energy charged pions tend to produce fairly straight tracks within the JDC and this makes the identification of the charge of a particle more difficult. Therefore the probability of wrongly identifying the charge of a particle is higher for the July data set.

The cut using the error code and energy-momentum fit of CBDROP removes more events in the July data set. This can be explained in the same way as the edge-crystal cut; The stronger bias towards the beam-line of the July data set causes more charged particles to travel along the beam line. This prevents many charged particles from producing a track in the outer layers of the JDC and hence the charged particles are less likely to traverse ten layers of the JDC. Likewise, the bias on all the particles increases the probability of the particles travelling along the beam line and hence going undetected.

Both data sets lose approximately the same fraction of events in the cuts for the CBKFIT fits to energy-momentum, $\pi^+\pi^-\pi^0\gamma\gamma$ and $\pi^+\pi^-\pi^0\eta$. This implies that the π^0 multiplicity in $\pi^+\pi^-\gamma\gamma\gamma\gamma$ events are similar for the two energy regions. Also the branching ratio for $\bar{p}p \rightarrow \pi^+\pi^-\pi^0\eta$ remains approximately the same for both energies.

3.5.2 Comparison of the Losses for the 0-Prong Data Sets

For the charged track multiplicity cut, the July data set loses a larger fraction of events compared with the December data whilst their corresponding Monte Carlo data sets lose approximately the same amount. This discrepancy can be explained by the inefficiency of the charged track trigger during the July data-taking. The December data loses more events than the July data on the unmatched PED cut. This is due to the increase in PED multiplicity with event energy and can be seen by comparing the multiplicities in Figure 2.8 of the detector chapter.

The July data loses more events on the edge-crystal cut and the electromagnetic split-off cut. The photons in the July data set are more biased to the beam direction and have, on average, a higher energy than those in the December data. The probability of an electromagnetic split-off occurring increases with the shower size, and therefore photon energy.

The December data set loses a large fraction of events due to the z-vertex and $3\pi^0\gamma\gamma$ fit compared with that of the July data. For the corresponding Monte Carlo data, the opposite is true. The difference in the real data losses is due to the error scaling; the December and July data pulls suggest that the errors used in the December data were slightly too small and therefore the kinematic fit was given less freedom to accept the December data events. For the Monte Carlo data, the error sizes were scaled more accurately. The $\pi^0\pi^0\pi^0\eta$ events at 1.94GeV/c lose slightly more events because the photons are more strongly biased towards the beam line; this increases the probability of one or more photons going undetected.

Both real data sets lose about the same fraction of events on the $\pi^0\pi^0\pi^0\eta$ cut, implying that the branching for $\bar{p}p \rightarrow \pi^0\pi^0\pi^0\eta$ is approximately the same for both energy regions.

3.6 Background Channels

After the fit to $\pi\pi\pi\gamma\gamma$ the invariant mass of the remaining photon pair was calculated. The resulting invariant mass plots for each data set can be seen in Figure 3.3. These show clearly that the relative branching ratio for 4π and $3\pi\eta$ produced in proton-antiproton annihilation is different for the charged and neutral channels but are not sensitive to the change in energy.

Estimating that the relative branching ratio, (R), for $\bar{p}p \rightarrow \pi\pi\pi\pi$ to $\bar{p}p \rightarrow \pi\pi\pi\eta$ is 25:1 for the charged data and 5:1 for the neutral data at both energies, then the amount of the $\pi\pi\pi\pi$ background channel can be calculated using equation 3.1.

$$\%Background = \frac{R \times \varepsilon(\pi\pi\pi\pi) \times 100\%}{1 \times \varepsilon(\pi\pi\pi\eta)} \tag{3.1}$$

The efficiencies $\varepsilon(\pi\pi\pi\eta)$ and $\varepsilon(\pi\pi\pi\pi)$ for events passing through the $\pi\pi\pi\eta$ analysis cuts have been calculated using Monte Carlo data for three different confidence level cuts for the fit to $\pi\pi\pi\eta$. These efficiencies and the corresponding percentage background can be found in Tables 3.8, 3.9, 3.10 and 3.11.

Background to $\bar{p}p \rightarrow \pi^+\pi^-\pi^0\eta$ at 1.20GeV/c			
Fit to $\pi^+\pi^-\pi^0\eta$	$\varepsilon(\pi^+\pi^-\pi^0\eta)$	$\varepsilon(\pi^+\pi^-\pi^0\pi^0)$	Background
CL Cut: $>$ 1%	21.73%	0.13%	14.6%
CL Cut: $>$ 10%	18.76%	0.06%	7.3%
CL Cut: $>$ 20%	16.67%	0.04%	6.2%

Table 3.8: Background for $\pi^+\pi^-\pi^0\eta$ at 1.20GeV/c.

The few 4π events that do manage to pass through the $\pi\pi\pi\eta$ cuts, despite the veto, have a flat distribution in the $\pi\pi$ versus $\pi\eta$ scatter plots for a 10% confidence level cut on the fit to $\pi\pi\pi\eta$. This is seen for all four data sets (as a typical example, see Figure 3.4) and therefore it is assumed that the 4π channel contributes a

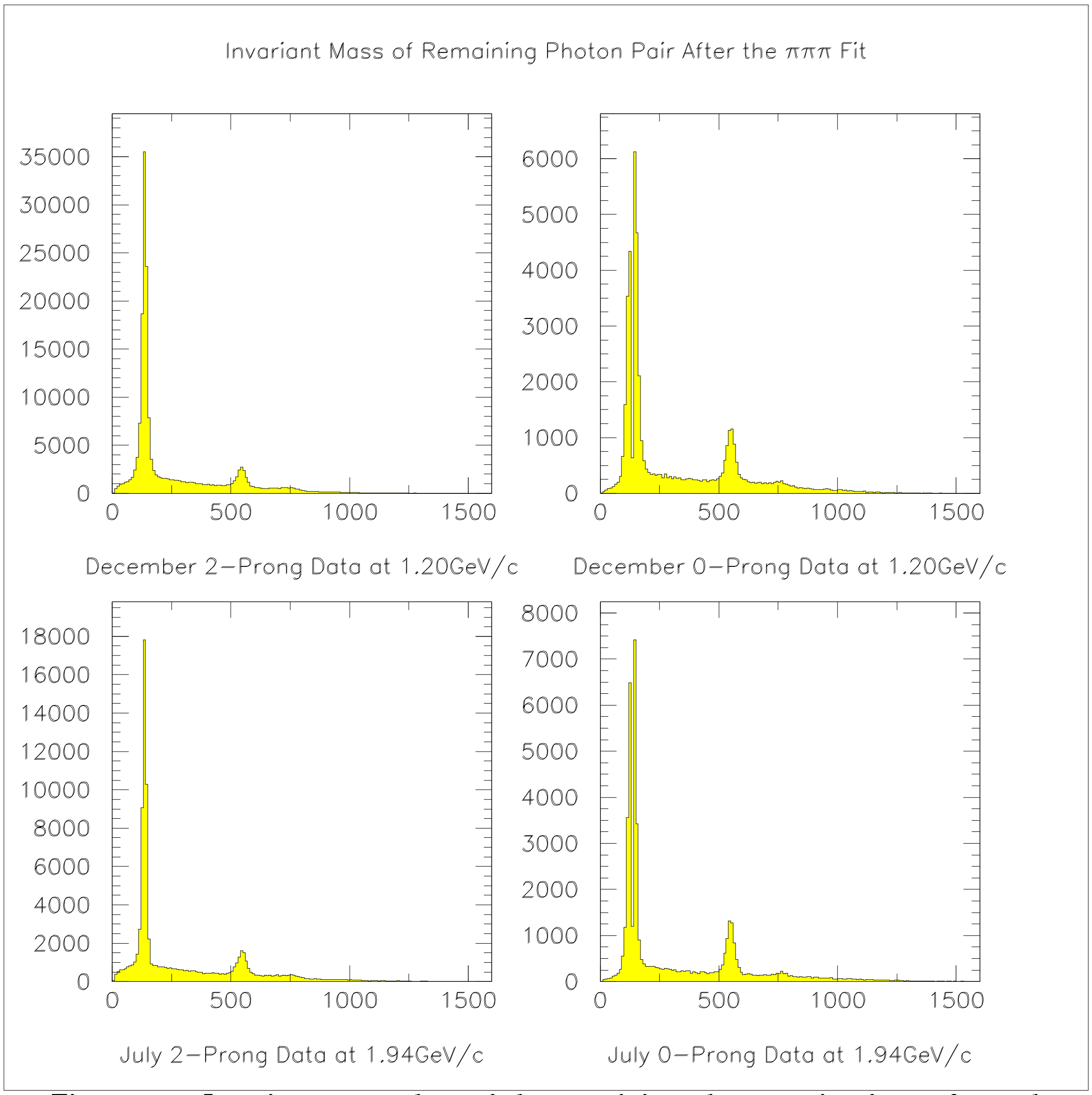

Figure 3.3: Invariant mass plots of the remaining photon pair after a fit to three pions. The two clear peaks are the π^0 and η from $\pi\pi\pi\pi$ and $\pi\pi\pi\eta$ events. The hole in the π^0 peak of the 0-prong data is due to the peak corresponding to the worst measured π^0 of the four π^0s; the best three have already been selected in the fit to $\pi^0\pi^0\pi^0\gamma\gamma$ and removed to leave the remaining photon pair.

Background to $\bar{p}p \to \pi^+\pi^-\pi^0\eta$ at 1.94GeV/c			
Fit to $\pi^+\pi^-\pi^0\eta$	$\varepsilon(\pi^+\pi^-\pi^0\eta)$	$\varepsilon(\pi^+\pi^-\pi^0\pi^0)$	Background
CL Cut: $> 1\%$	13.70%	0.14%	30%
CL Cut: $> 10\%$	11.83%	0.07%	15%
CL Cut: $> 20\%$	10.40%	0.04%	10%

Table 3.9: Background for $\pi^+\pi^-\pi^0\eta$ at 1.94GeV/c.

Background to $\bar{p}p \to \pi^0\pi^0\pi^0\eta$ at 1.20GeV/c			
Fit to $\pi^0\pi^0\pi^0\eta$	$\varepsilon(\pi^0\pi^0\pi^0\eta)$	$\varepsilon(\pi^0\pi^0\pi^0\pi^0)$	Background
CL Cut: $> 1\%$	18.36	0.37	10%
CL Cut: $> 10\%$	14.87	0.15	5%
CL Cut: $> 20\%$	12.76	0.09	4%

Table 3.10: Background for $\pi^0\pi^0\pi^0\eta$ at 1.20GeV/c.

Background to $\bar{p}p \to \pi^0\pi^0\pi^0\eta$ at 1.94GeV/c			
Fit to $\pi^0\pi^0\pi^0\eta$	$\varepsilon(\pi^0\pi^0\pi^0\eta)$	$\varepsilon(\pi^0\pi^0\pi^0\pi^0)$	Background
CL Cut: $> 1\%$	12.43	0.28	11%
CL Cut: $> 10\%$	9.72	0.12	6%
CL Cut: $> 20\%$	8.18	0.08	5%

Table 3.11: Background for $\pi^0\pi^0\pi^0\eta$ at 1.94GeV/c.

structureless background to the $\pi\pi\pi\eta$ data.

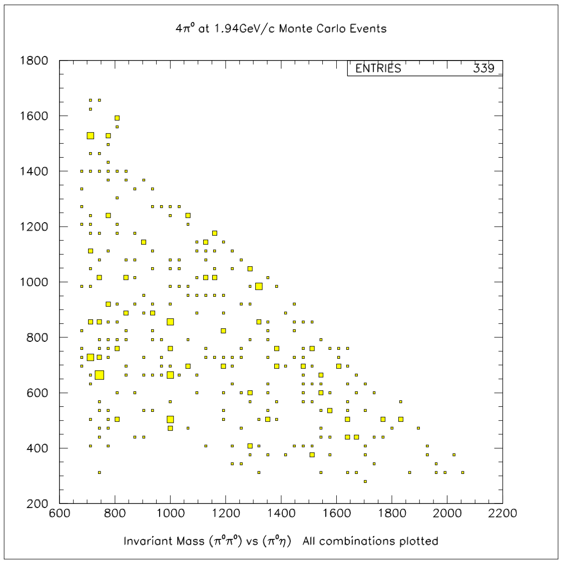

Figure 3.4: Scatter plot for $4\pi^0$ Monte Carlo events that passed the $\pi^0\pi^0\pi^0\eta$ event selection cuts.

The invariant mass distribution for the remaining photon pair, after background channel cuts, can be found in Figure 3.5. Events successfully fitted to $\bar{p}p \rightarrow \pi\pi\pi\pi$, (and in addition, $\omega\omega\pi$ for the all-neutral data) were not included in the latter figure. The η peaks now show a good signal to noise ratio. The remaining background under the η peaks is due to the kinematic fitting package wrongly pairing photons and also the incomplete kinematic reconstruction of channels with a similar final state.

To avoid the four pion background channels a 10% confidence level cut was used for the kinematic fits to $\pi\pi\pi\eta$ when creating the final data sets used for this analysis.

3.7 Mass Resolution

An estimate of the detector's mass resolution has been made using photons produced in the decay of the π^0 and η particles. By calculating and plotting (Figure 3.6 Top)

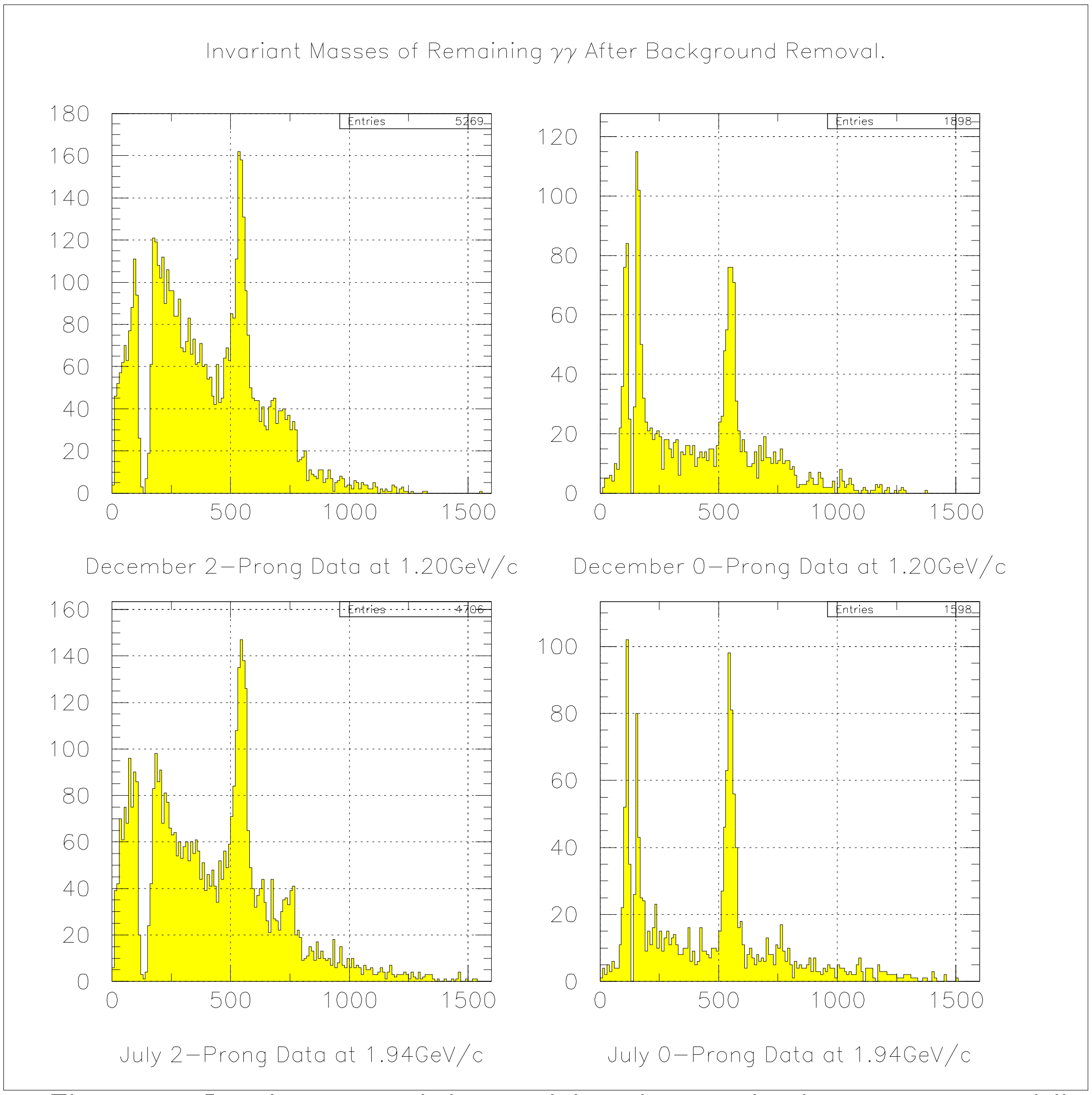

Figure 3.5: Invariant mass of the remaining photon pair after events successfully fitted to background channels have been removed.

the invariant mass of all unmatched PED pair combinations, a π^0 peak can be seen. An η peak can be seen (Figure 3.6 Bottom) when the unmatched PEDs that can form an invariant mass in the π^0 mass region are ignored. These invariant mass plots were produced after the following cuts were made:-

- Charged data.
  - Two charged tracks of equal and opposite sign.
  - $3 <$ Number of unmatched PEDs > 7.
  - No events with an edge-crystal PED.
- All-neutral data.
  - Eight unmatched PEDs, No charged tracks.
  - No events with an edge-crystal PED.
  - No events with electromagnetic split-offs.

The π^0 and η peaks have been fitted with a Gaussian distribution with the background fitted using a 4^{th} order polynomial. The results from the fits can be seen in Tables 3.12 and 3.13.

Data Set	Momentum	m(π^0) MeV	$\sigma(\pi^0)$ MeV	Resolution
2-Prong	1.20	135.95 ± 0.02	10.43 ± 0.03	7.67%
2-Prong	1.94	135.94 ± 0.02	9.71 ± 0.03	7.09%
0-Prong	1.20	136.73 ± 0.04	10.62 ± 0.04	7.77%
0-Prong	1.94	134.95 ± 0.02	9.71 ± 0.03	7.20%

Table 3.12: Mass resolutions calculated using π^0 peaks.

All four different data sets show that the detector has a very good mass resolution and that the fractional energy resolution (ΔE/E) and the position resolution improve

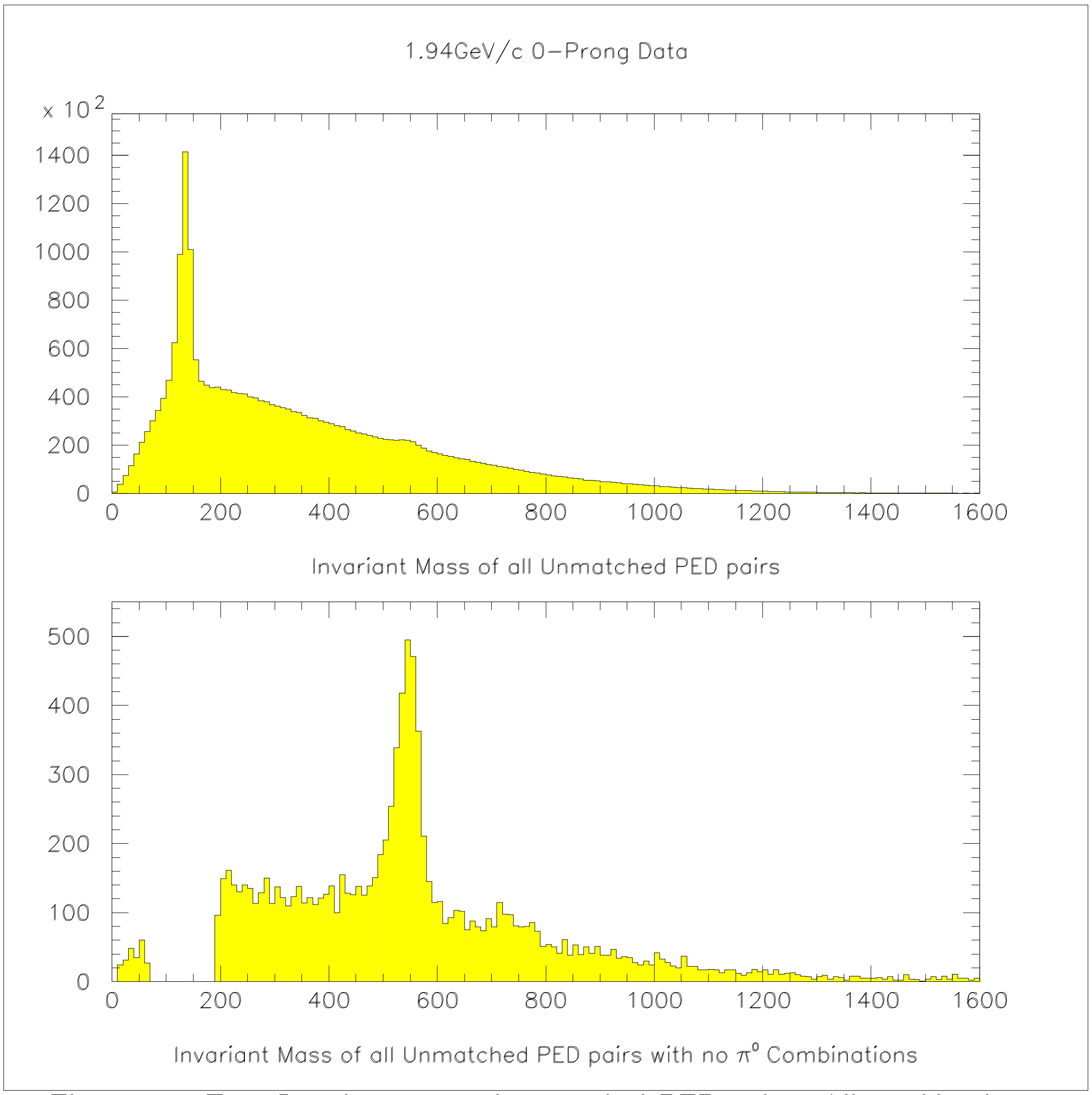

Figure 3.6: Top: Invariant mass of unmatched PED pairs. All combinations are plotted. Bottom: Invariant mass of unmatched PED pairs. All combinations not involved in the π^0 mass region are plotted.

Data Set	Momentum	m(η) MeV	$\sigma(\eta)$ MeV	Resolution
2-Prong	1.20	544.3 $\pm$ 0.4	19.2 $\pm$ 0.5	3.5%
2-Prong	1.94	547.3 $\pm$ 0.4	19.3 $\pm$ 0.7	3.5%
0-Prong	1.20	545 $\pm$ 1	22 $\pm$ 1	4%
0-Prong	1.94	544.5 $\pm$ 0.8	20.7 $\pm$ 0.8	3.8%

Table 3.13: Mass resolutions calculated using η peaks.

with increasing photon energy. This can be explained by the high energy photons producing large showers which have less significant statistical fluctuations and span many crystals.

3.8 Summary of Data Selection

Over 10 million raw data events (9327K of real data and 956K of Monte Carlo data) have been accumulated and processed. Table 3.14 summarizes the data sets used and the fraction of events that passed the standard selection criteria for $\pi^+\pi^-\pi^0\eta$ and $\pi^0\pi^0\pi^0\eta$ events.

The most likely source of background to the $\pi^+\pi^-\pi^0\eta$ data comes from $\pi^+\pi^-\pi^0\pi^0$ events. The $\pi^0\pi^0\pi^0\eta$ data has two channels that may contribute to background: $\pi^0\pi^0\pi^0\pi^0$ and $\omega\omega\pi^0$. All background channels are fitted and events rejected if the resulting confidence level is greater than 1%. Contamination due to the $\omega\omega\pi^0$ channel is thought to be negligible due to it's low branching ratio. Those 4π events that do filter through the analysis cuts do not produce a structured background. To reduce the background channel contamination further, a confidence level of 10% for the fit to $\pi\pi\pi\eta$ was used.

Data Set	$\bar{p}$ Momenta (Gev/c)	Events Analysed	Events Passed	Events Passed (%)
Real: Dec 91 Special	1.20	1 998K	19 918	1.00
Real: Dec 91 0-Prong	1.20	1 599K	6 838	0.43
MC $\bar{p}p \rightarrow \pi^+\pi^-\pi^0\eta$	1.20	203K	44 116	21.73
MC $\bar{p}p \rightarrow \pi^0\pi^0\pi^0\eta$	1.20	113K	20 688	18.36
MC $\bar{p}p \rightarrow \pi^+\pi^-\pi^0\pi^0$	1.20	100K	127	0.13
MC $\bar{p}p \rightarrow \pi^0\pi^0\pi^0\pi^0$	1.20	100K	370	0.37
Real: Jul 92 2-Prong	1.94	4 261K	11 916	0.28
Real: Jul 92 0-Prong	1.94	1 469K	6 993	0.47
MC $\bar{p}p \rightarrow \pi^+\pi^-\pi^0\eta$	1.94	150K	20 554	13.70
MC $\bar{p}p \rightarrow \pi^0\pi^0\pi^0\eta$	1.94	95K	11 864	12.43
MC $\bar{p}p \rightarrow \pi^+\pi^-\pi^0\pi^0$	1.94	100K	142	0.14
MC $\bar{p}p \rightarrow \pi^0\pi^0\pi^0\pi^0$	1.94	95K	267	0.28

Table 3.14: Data Sets Used in the Analysis.

Chapter 4

Mass Distributions

4.1 Introduction

This chapter presents the general invariant mass distributions for the $\pi^+\pi^-\pi^0\eta$ and $\pi^0\pi^0\pi^0\eta$ data sets. Comparisons are made between the charged and neutral channels and also between the data sets at 1.20 GeV/c and 1.94 GeV/c.

The plots have the following conventions: real data distributions are shown with error bars whilst the acceptance corrected phase space Monte Carlo data are given by solid lines; The real data are normalized to one and Monte Carlo are arbitrarily normalized so that the Monte Carlo profiles match the real data profiles in *non-resonant* mass regions. The Monte Carlo data have been smoothed using a smoothing algorithm[36] to reduce any statistical fluctuations.

Both the 2-prong and 0-prong data sets contain a dominant and well understood process:-

- **2-Prong**: $\bar{p}p \to \eta\omega \quad (\omega \to \pi^+\pi^-\pi^0)$ Figure 4.1
- **0-Prong**: $\bar{p}p \to \eta\eta_{(3\pi)} \quad (\eta_{(3\pi)} \to \pi^0\pi^0\pi^0)$ Figure 4.2

The $\bar{p}p \to \eta\omega$ and $\bar{p}p \to \eta\eta$ events are of little interest in this analysis and are not included in the mass plots. The events are easily and safely removed (by using

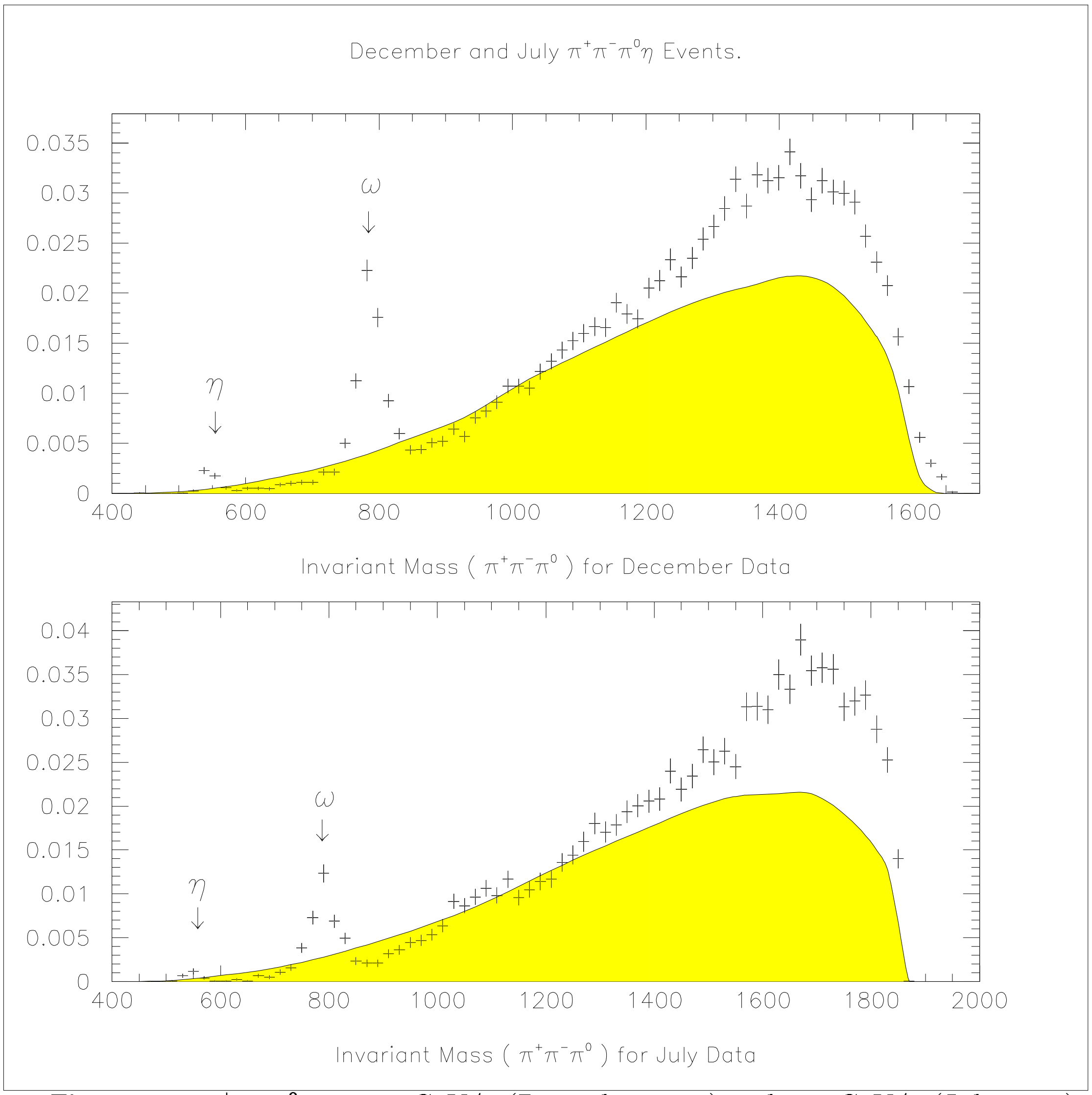

Figure 4.1: $\pi^+\pi^-\pi^0\eta$ at 1.20GeV/c (December 1991) and 1.94GeV/c (July 1992). Both data sets show signals for the η and ω corresponding to $\bar{p}p \to \eta\eta$ and $\bar{p}p \to \eta\omega$ events. The shaded mass distribution represents the Monte Carlo data.

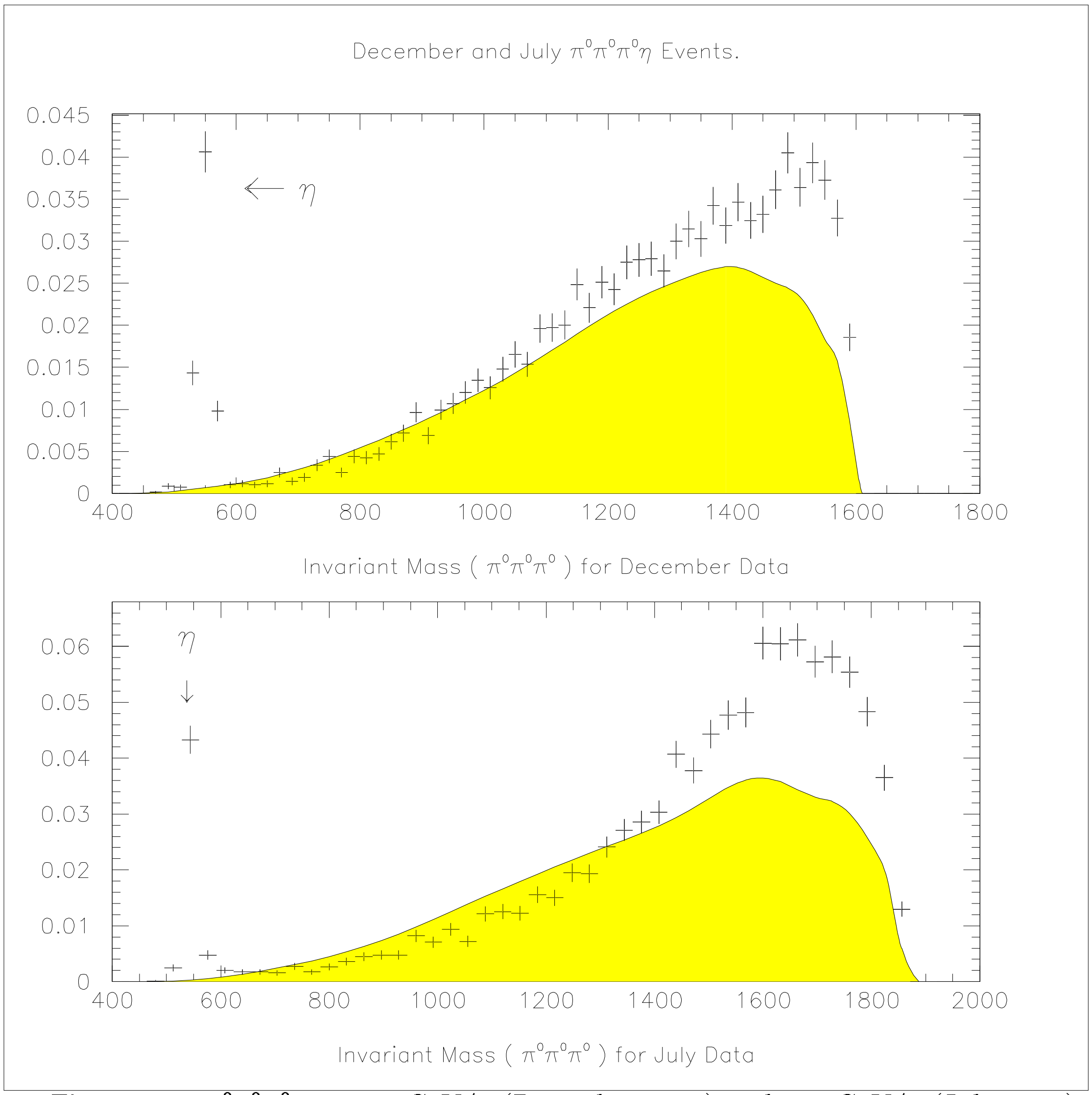

Figure 4.2: $\pi^0\pi^0\pi^0\eta$ at 1.20GeV/c (December 1991) and 1.94GeV/c (July 1992). Both data sets show signals for the η corresponding to $\bar{p}p \rightarrow \eta\eta$ events. The shaded mass distribution represents the Monte Carlo data.

a kinematic fit with a confidence level cut of 1%) since they involve narrow states and have a high signal to background ratio. The number of remaining events left after the $\eta\omega/\eta\eta$ events have been removed can be found in Table 4.1.

Data Set	$\bar{p}$ Momentum (GeV/c)	Events	MC Events
$\pi^+\pi^-\pi^0\eta$	1.20	12 981	37 168
$\pi^+\pi^-\pi^0\eta$	1.94	8 318	17 483
$\pi^0\pi^0\pi^0\eta$	1.20	3 601	16 722
$\pi^0\pi^0\pi^0\eta$	1.94	4 627	9 265

Table 4.1: Event numbers for each data set used in this analysis.

4.2 $\pi^+\pi^-\pi^0\eta$ Mass Distributions

This section contains the invariant mass plots from the $\pi^+\pi^-\pi^0\eta$ data where the antiproton momentum was 1.20 or 1.94 GeV/c. For both data sets the following invariant mass distributions are shown:-

- Invariant Mass ($\pi^+\pi^-\eta$)
- Invariant Mass ($\pi^\pm\pi^0\eta$)
- Invariant Mass ($\pi^+\pi^-\pi^0$)
- Invariant Mass ($\pi^+\pi^-$)
- Invariant Mass ($\pi^0\eta$)
- Invariant Mass ($\pi^\pm\eta$)
- Invariant Mass ($\pi^\pm\pi^0$)
- Invariant Mass ($\pi^\pm\pi^0$ versus $\pi^\mp\eta$)

- Invariant Mass ($\pi^+\pi^-$ versus $\pi^0\eta$).

Each distribution is compared with the corresponding acceptance corrected phase space Monte Carlo data which is represented by the shaded mass distribution. The $\pi^\pm\pi^0$ versus $\pi^\mp\eta$ and $\pi^+\pi^-$ versus $\pi^0\eta$ plots are similar to Dalitz plots. In the former, both charge combinations are plotted. This style of scatter plot was first introduced by Chinowsky and Goldhaber and a discussion of four body kinematic phase space can be found in references [37] and [38].

4.2.1 $\pi^+\pi^-\pi^0\eta$ at 1.20 GeV/c

The mass plots for $\bar{p}p \rightarrow \pi^+\pi^-\pi^0\eta$ at 1.20 GeV/c can be found in Figures 4.3 to 4.7.

Major discrepancies between the Monte Carlo and real data are seen in the mass distributions for $\pi^+\pi^-\eta$, $\pi^\pm\pi^0\eta$ and $\pi^+\pi^-\pi^0$. These may be understood by intermediate resonances (not included in the Monte Carlo simulation) distorting the phase space of the four particle final state. As can be seen in Figures 4.6 and 4.7, the prominent channels of the $\pi^+\pi^-\pi^0\eta$ data are:-

- $\bar{p}p \rightarrow a_2(1320)\rho \rightarrow (\pi\eta)(\pi\pi)$
- $\bar{p}p \rightarrow a_0(980)\rho \rightarrow (\pi\eta)(\pi\pi)$.

Three weaker signals from $\eta'(958)$, $f_1(1285)$ and η can be seen in the following channels:-

- $\bar{p}p \rightarrow \pi^0\eta'(958) \rightarrow \pi^0(\pi^+\pi^-\eta)$
- $\bar{p}p \rightarrow \pi^0 f_1(1285) \rightarrow \pi^0[\pi^\pm a_0^\mp(980)] \rightarrow \pi^0\pi^\pm(\pi^\mp\eta)$
- $\bar{p}p \rightarrow \eta\eta \rightarrow \eta(\pi^+\pi^-\pi^0)$.

Large discrepancies between the real and Monte Carlo data occur in the (1400-1800)MeV region of both the $(\pi^+\pi^-\eta)$ and $(\pi^\pm\pi^0\eta)$ mass distributions. The real data contains a large enhancement around 1400MeV in the $(\pi^+\pi^-\pi^0)$ mass distribution. Assuming that the latter enhancement is not a phase space reflection from the dominant channels, two candidates for the source of the enhancement are the $\omega(1390)$ and $\pi(1300)$ in the following channels:-

- $\bar{p}p \rightarrow \eta\omega(1390) \rightarrow \eta(\pi\rho) \rightarrow \eta\pi(\pi\pi)$
- $\bar{p}p \rightarrow \eta\pi(1300) \rightarrow \eta(\pi\rho) \rightarrow \eta\pi(\pi\pi)$.

No well established mesons with broad widths and a decay mode into $\pi\pi\eta$ can account for the real data enhancements in the $\pi\pi\eta$ mass distributions.

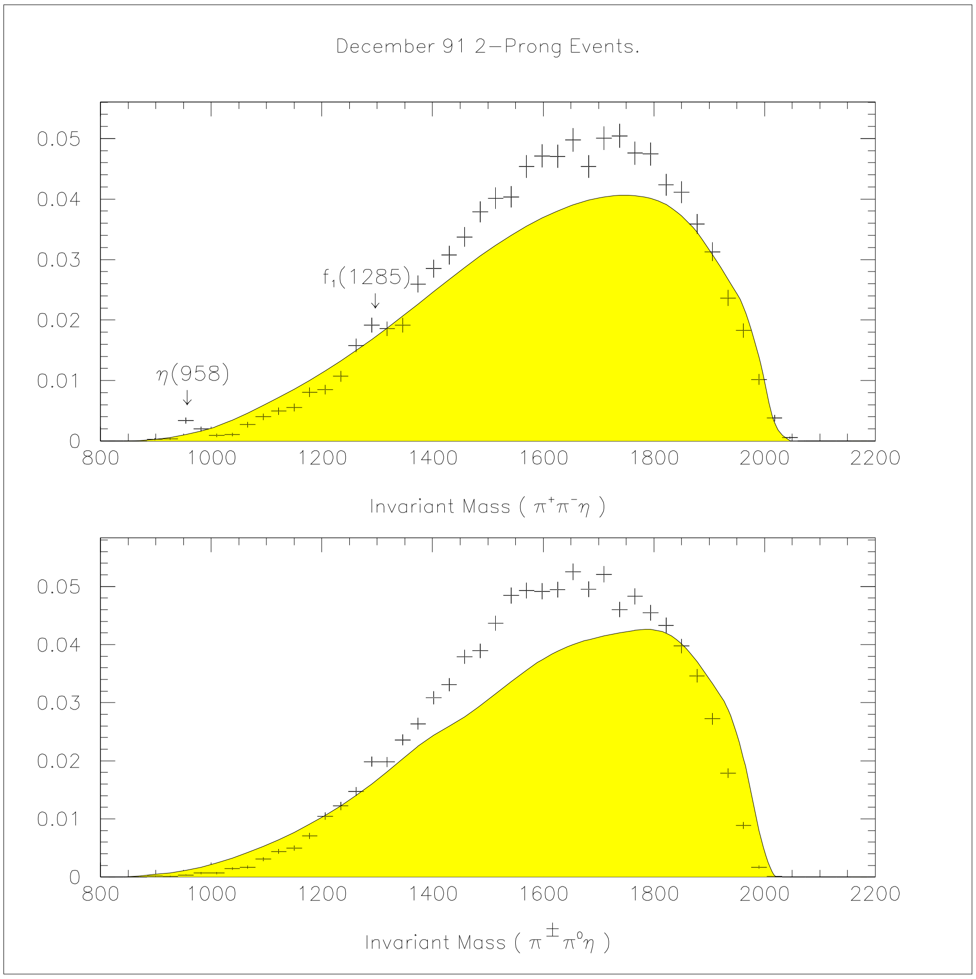

Figure 4.3: 1.20GeV/c data. Top: Invariant Mass of $(\pi^+\pi^-\eta)$. The $\eta'(958)$ and $f_1(1285)$ can be seen clearly. A large discrepancy between the real and Monte Carlo data occurs between 1400 and 1800 MeV. Bottom: Invariant Mass of $(\pi^\pm\pi^0\eta)$. Again there is a discrepancy in the $1400 \rightarrow 1800$ MeV mass region.

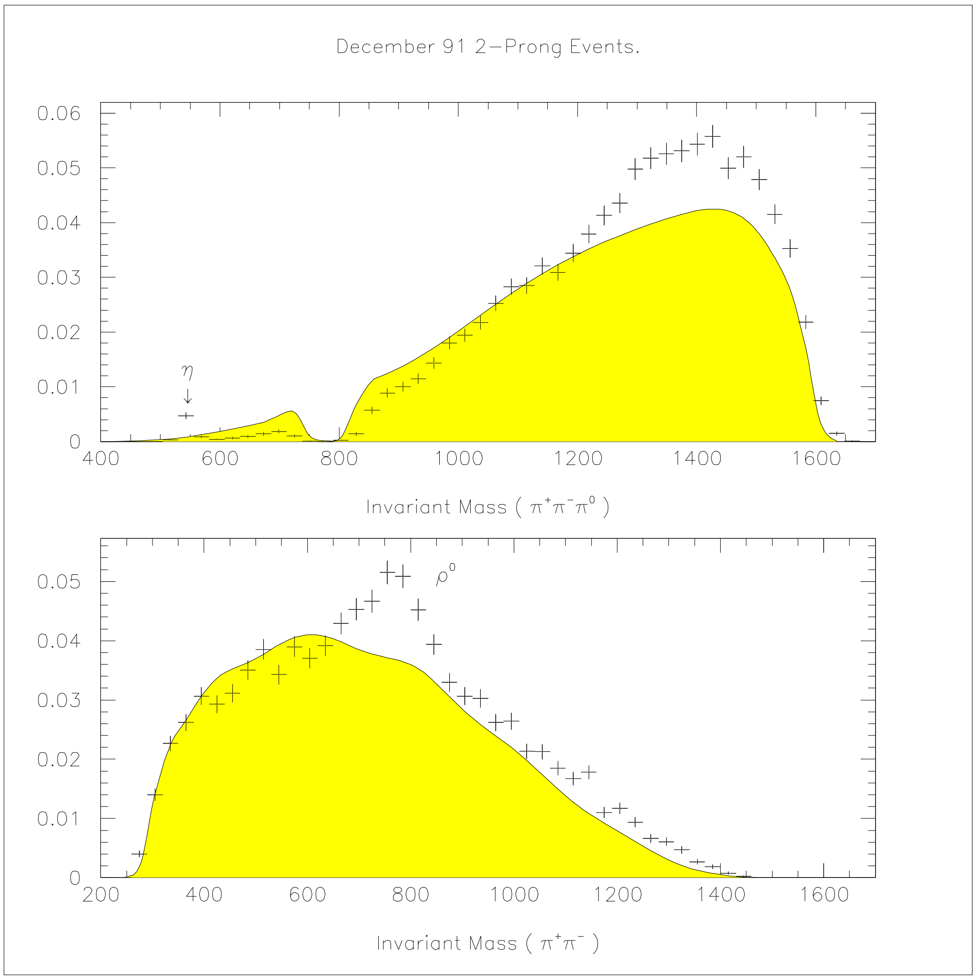

Figure 4.4: 1.20GeV/c data. Top: Invariant Mass of $(\pi^+\pi^-\pi^0)$. A clear η peak can be seen. The hole just below 800 MeV is caused by the removal of the events that were successfully fitted to $\omega\eta$. A large discrepancy occurs around 1400 MeV. Bottom: Invariant Mass of $(\pi^+\pi^-)$. The neutral ρ is seen clearly.

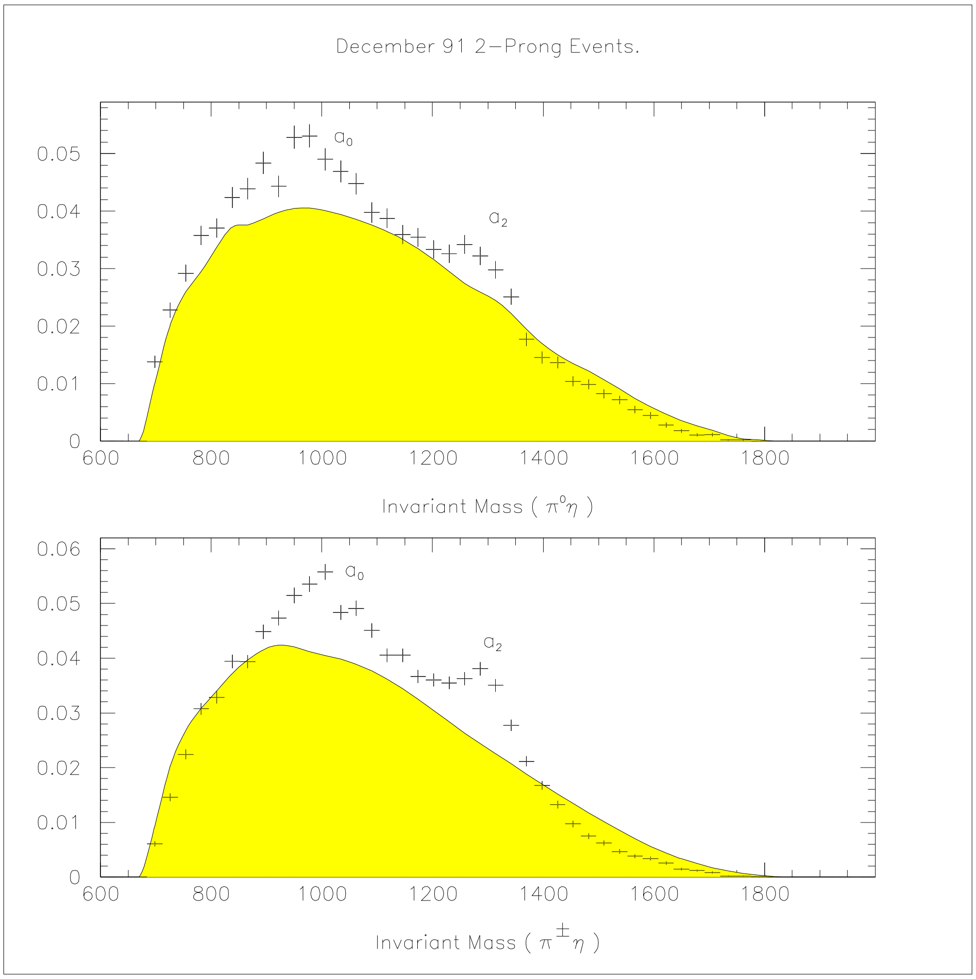

Figure 4.5: 1.20GeV/c data. Top: Invariant Mass of ($\pi^0\eta$). Clear $a_0(980)$ and $a_2(1320)$ peaks can be seen. Bottom: Invariant Mass of ($\pi^{\pm}\eta$). Peaks due to the charged $a_0(980)$ and $a_2(1320)$ are seen.

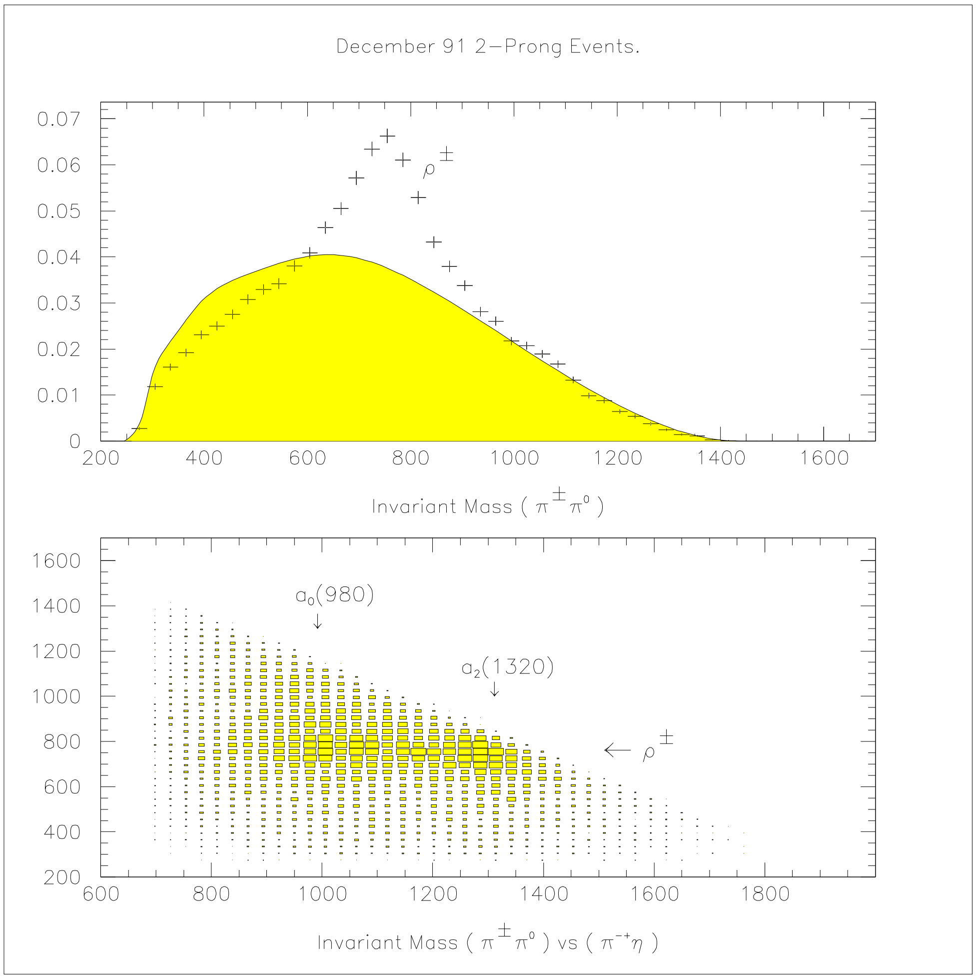

Figure 4.6: 1.20GeV/c data. Top: Invariant Mass of $(\pi^{\pm}\pi^{0})$. The charged ρ dominates this plot. Bottom: Invariant Mass of $(\pi^{\pm}\pi^{0})$ versus $(\pi^{\mp}\eta)$. The prominent channels in this scatter plot are $\rho^{\pm}a_0^{\mp}(980)$ and $\rho^{\pm}a_2^{\mp}(1320)$.

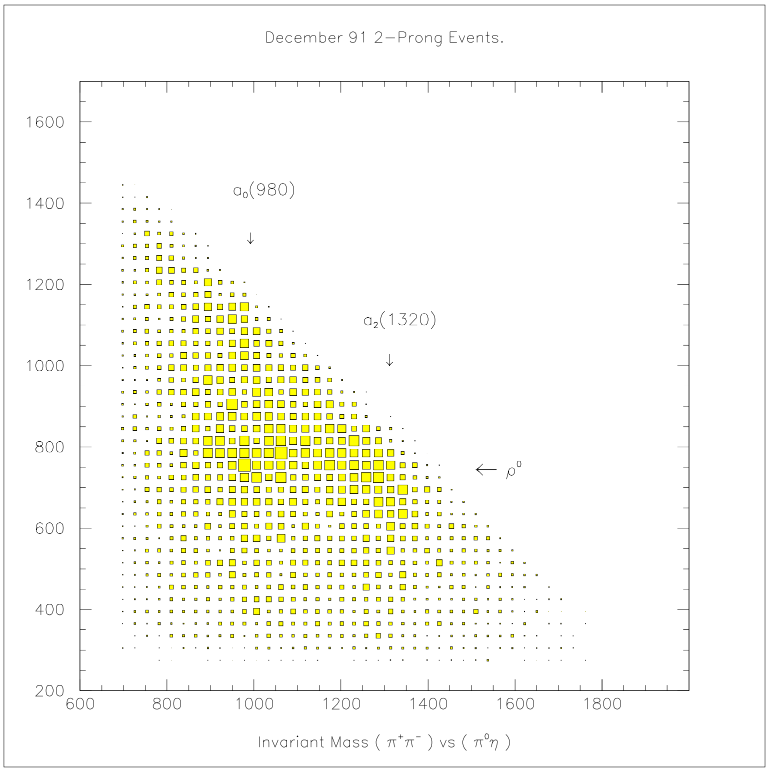

Figure 4.7: 1.20GeV/c data. Invariant Mass of $(\pi^+\pi^-)$ versus $(\pi^0\eta)$. The prominent channels in this scatter plot are $\rho^0 a_0(980)$ and $\rho^0 a_2(1320)$.

4.2.2 $\pi^+\pi^-\pi^0\eta$ at 1.94 GeV/c

The mass plots for $\bar{p}p \rightarrow \pi^+\pi^-\pi^0\eta$ at 1.94 GeV/c (Figures 4.8 to 4.12) are presented in the same format as the 1.20 GeV/c data set.

Major differences between the Monte Carlo and real data are seen in the mass distributions for $\pi^+\pi^-\eta$, $\pi^\pm\pi^0\eta$ and $\pi^+\pi^-\pi^0$. These may be understood by intermediate resonances (not included in the Monte Carlo simulation) distorting the phase space of the four particle final state. As can be seen in Figures 4.11 and 4.12, the prominent channels of the $\pi^+\pi^-\pi^0\eta$ data are:-

- $\bar{p}p \rightarrow a_2(1320)\rho \rightarrow (\pi\eta)(\pi\pi)$
- $\bar{p}p \rightarrow a_0(980)\rho \rightarrow (\pi\eta)(\pi\pi)$
- $\bar{p}p \rightarrow a_0^0(980)f_2(1270) \rightarrow (\pi^0\eta)(\pi^+\pi^-)$.

Weaker signals from the $\eta'(958)$ and η can be seen in the following channels:-

- $\bar{p}p \rightarrow \pi^0\eta'(958) \rightarrow \pi^0(\pi^+\pi^-\eta)$
- $\bar{p}p \rightarrow \eta\eta \rightarrow \eta(\pi^+\pi^-\pi^0)$.

A large discrepancy between the real and Monte Carlo data occurs in the $(\pi^+\pi^-\eta)$ (1600-2100)MeV mass region. The $(\pi^\pm\pi^0\eta)$ mass distribution shows an enhancement in the real data between (1400-1900)MeV. A strong discrepancy in the $(\pi^+\pi^-\pi^0)$ mass distributions occurs around 1700MeV. Assuming that the latter enhancement is not due to phase space reflections from the dominant channels, a candidate for the source of this enhancement is the $\pi_2(1670)$ in:-

- $\bar{p}p \rightarrow \eta\pi_2(1670) \rightarrow \eta[\pi^0 f_2(1270)] \rightarrow \eta\pi^0(\pi^+\pi^-)$
- $\bar{p}p \rightarrow \eta\pi_2(1670) \rightarrow \eta(\pi\rho) \rightarrow \eta\pi(\pi\pi)$.

No well established mesons with broad widths and a decay mode into $\pi\pi\eta$ can account for the real data enhancements in the $\pi\pi\eta$ mass distribution.

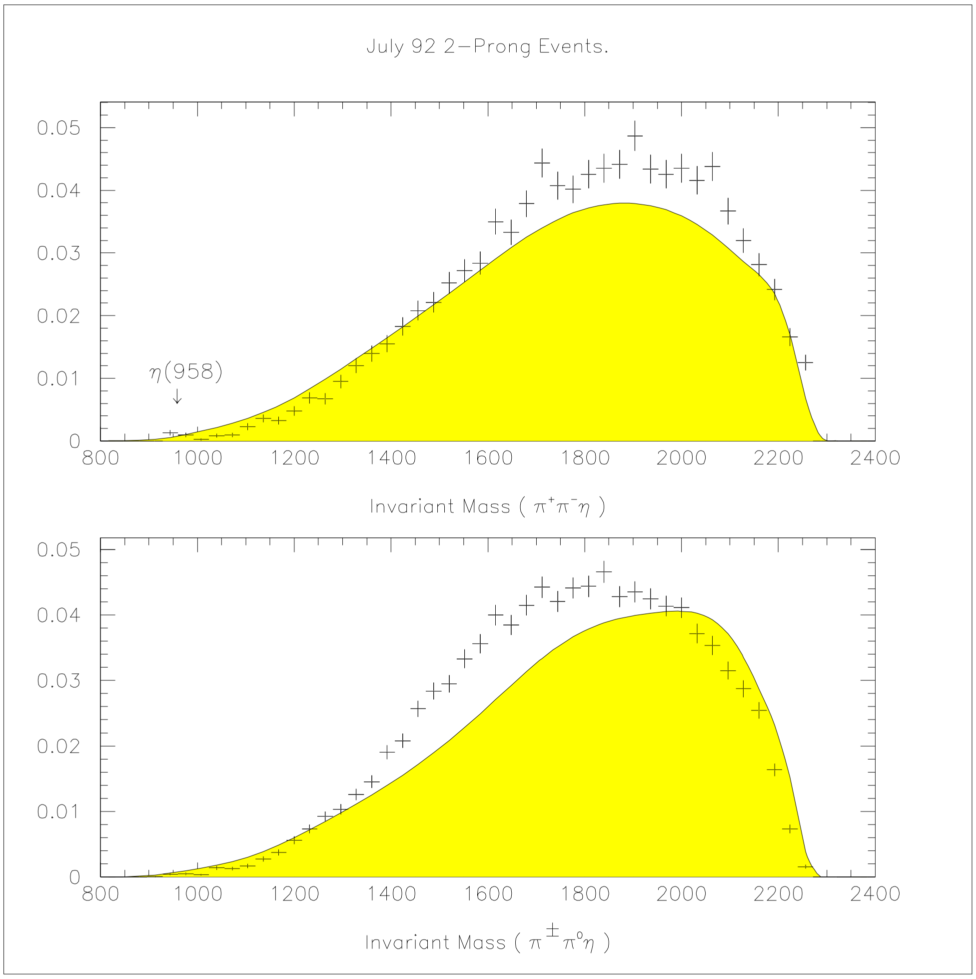

Figure 4.8: 1.94GeV/c data. Top: Invariant Mass of $(\pi^+\pi^-\eta)$. The $\eta'(958)$ can just be seen at the edge of phase space. A large discrepancy between the real and Monte Carlo data occurs between 1600 and 2100 MeV. Bottom: Invariant Mass of $(\pi^\pm\pi^0\eta)$. Here the discrepancy arises in the $1400 \rightarrow 1900$ MeV mass region.

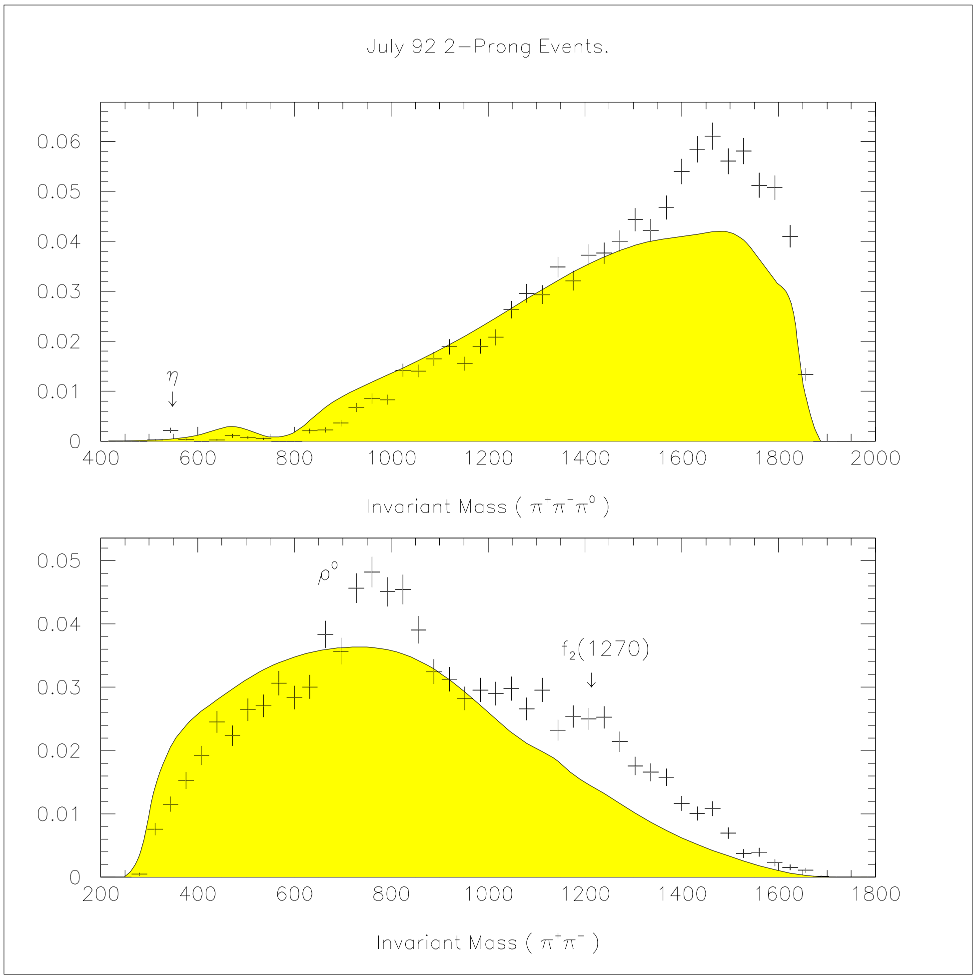

Figure 4.9: 1.94GeV/c data. Top: Invariant Mass of $(\pi^+\pi^-\pi^0)$. An η peak can be seen at the edge of phase space. The hole just below 800 MeV is caused by the removal of the events that were successfully fitted to $\omega\eta$. A large discrepancy occurs around 1600 MeV. Bottom: Invariant Mass of $(\pi^+\pi^-)$. The neutral ρ and $f_2(1270)$ are seen clearly.

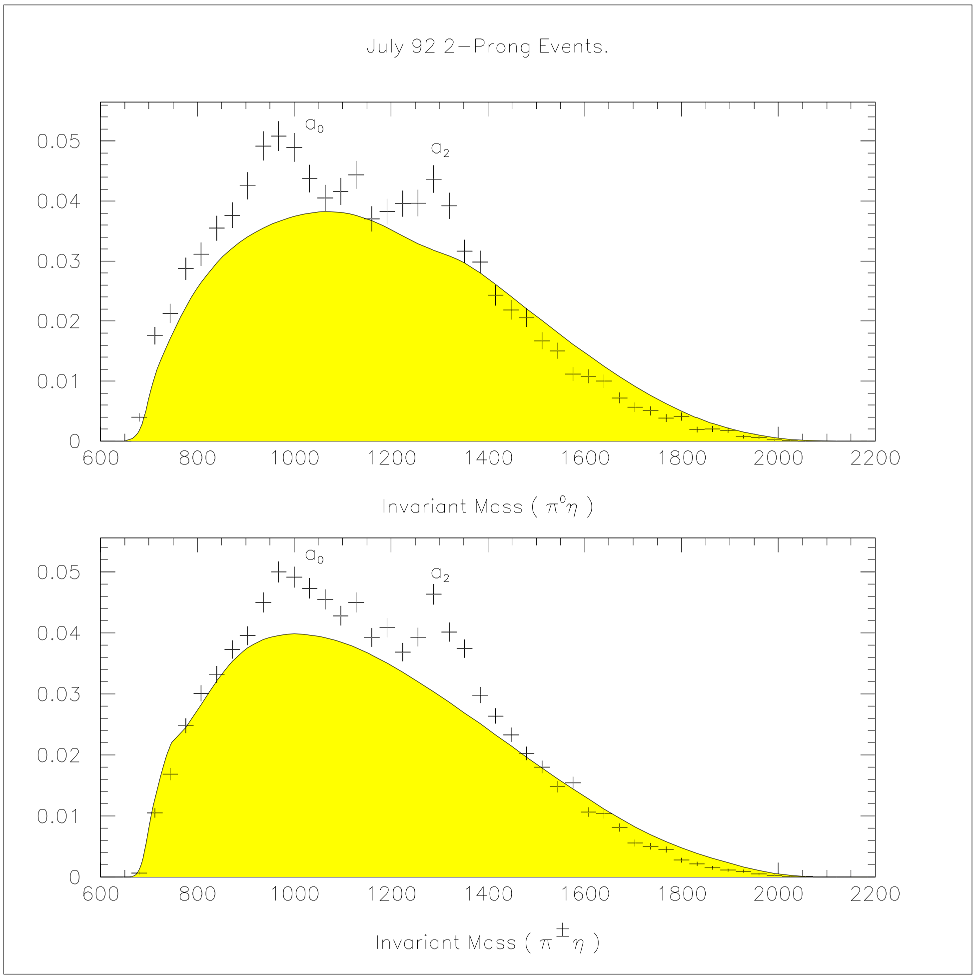

Figure 4.10: 1.94GeV/c data. Top: Invariant Mass of $(\pi^0\eta)$. Clear $a_0(980)$ and $a_2(1320)$ peaks can be seen. Bottom: Invariant Mass of $(\pi^\pm\eta)$. Peaks due to the charged $a_0(980)$ and $a_2(1320)$ are seen.

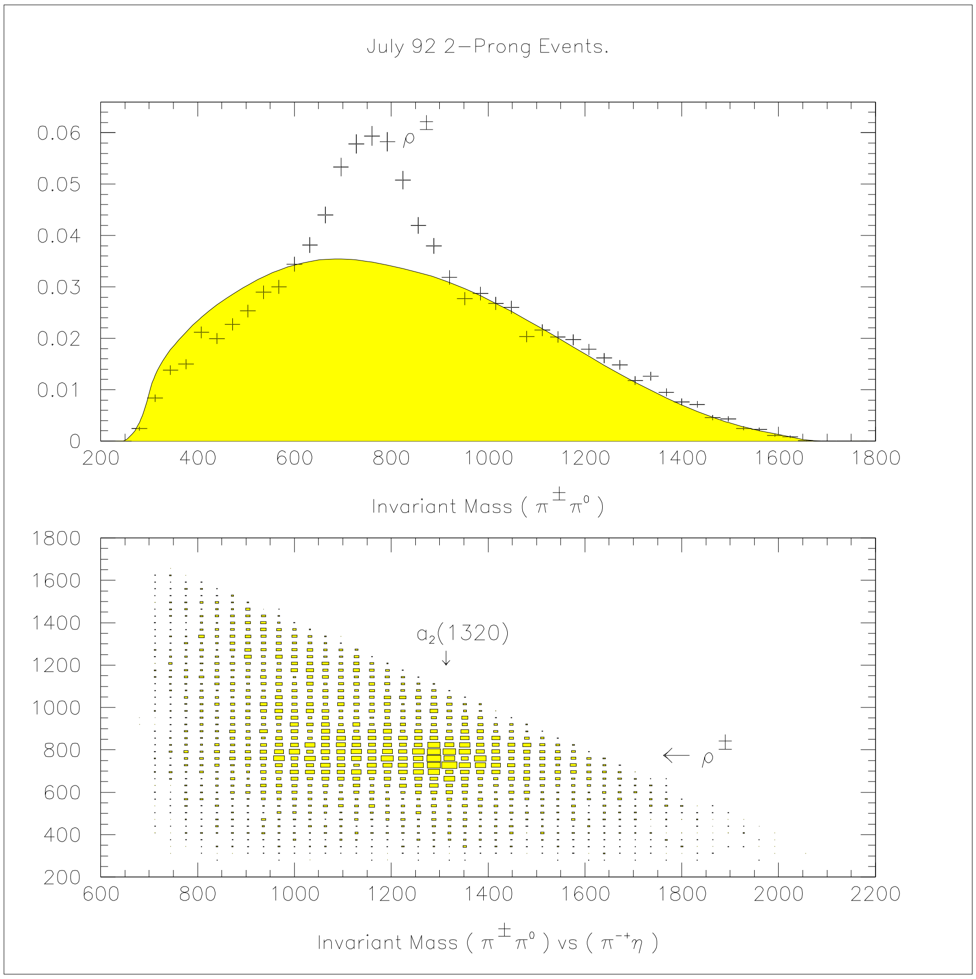

Figure 4.11: 1.94Ge/c data. Top: Invariant Mass of $(\pi^{\pm}\pi^{0})$. The charged ρ dominates this plot. Bottom: Invariant Mass of $(\pi^{\pm}\pi^{0})$ versus $(\pi^{\mp}\eta)$. The prominent channel in this scatter plot is $\rho^{\pm}a_2^{\mp}(1320)$.

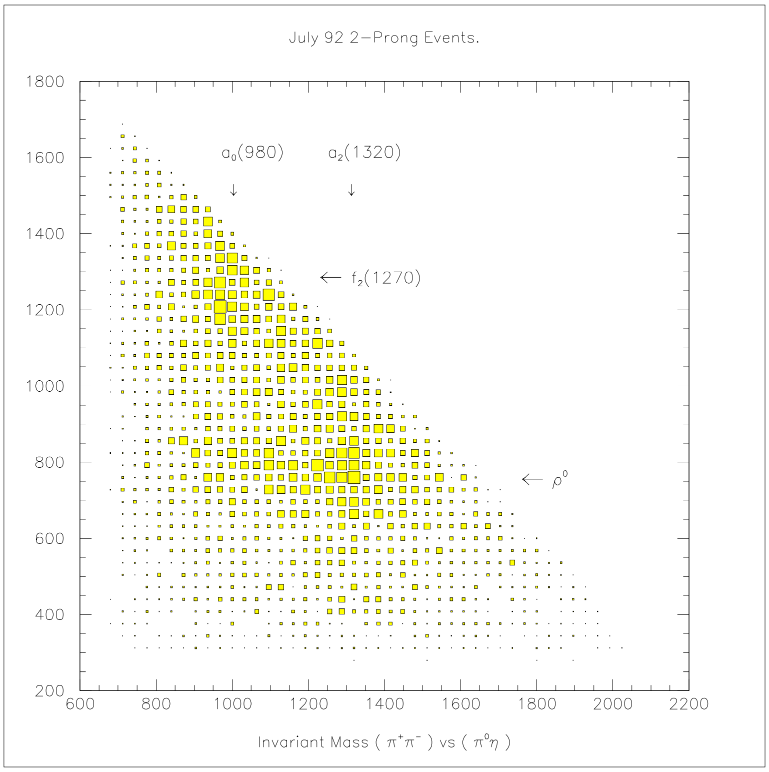

Figure 4.12: 1.94GeV/c data. Invariant Mass of $(\pi^+\pi^-)$ versus $(\pi^0\eta)$. The prominent channels in this scatter plot are $f_2(1270)a_0(980)$ and $\rho^0 a_2(1320)$.

4.2.3 Comparison of $\bar{p}p \to \pi^+\pi^-\pi^0\eta$ at 1.20 and 1.94 GeV/c

The main difference between the two data sets is the change in prominent channels that include the $a_0(980)$. At 1.20 GeV/c both the charged and neutral $a_0(980)\rho$ channels are seen clearly but at 1.94 GeV/c this is replaced by $\bar{p}p \to a_0^0(980)f_2(1270)$. Very few $a_0^\pm\rho^\mp$ events are observed: the only enhancement along the $\rho^\pm$ band is due to the $a_2^\mp(1320)$.

In terms of similarities, both data sets contain enhancements in the $\pi\pi\eta$ (1600-1800)MeV mass regions. Also, the scatter plots show a charged and neutral ρ band. These two characteristics of the data are suggestive of an isospin, I=1 resonance with a mass between (1600-1800)MeV decaying into $\rho\eta$.

4.3 $\pi^0\pi^0\pi^0\eta$ Mass Distributions

This section contains the invariant mass plots from the $\pi^0\pi^0\pi^0\eta$ data where the antiproton momentum was 1.20 and 1.94 GeV/c. For both data sets the following invariant mass distributions are shown:-

- Invariant Mass ($\pi^0\pi^0\pi^0$)
- Invariant Mass ($\pi^0\pi^0\eta$)
- Invariant Mass ($\pi^0\eta$)
- Invariant Mass ($\pi^0\pi^0$)
- Invariant Mass ($\pi^0\pi^0$ versus $\pi^0\eta$).

Each distribution is compared with the corresponding acceptance corrected phase space Monte Carlo data which are represented by the shaded mass distributions.

4.3.1 $\pi^0\pi^0\pi^0\eta$ at 1.20 GeV/c

The mass plots for $\bar{p}p \to \pi^0\pi^0\pi^0\eta$ at 1.20GeV/c can be found in Figures 4.13 to 4.15. These show the prominent channels to be:-

- $\bar{p}p \to a_0(980)\sigma \to (\pi^0\eta)(\pi^0\pi^0)$
- $\bar{p}p \to a_2(1320)\sigma \to (\pi^0\eta)(\pi^0\pi^0)$.

where σ represents the $\pi^0\pi^0$ S-wave amplitude.[39] Weaker signals from the $\eta'(958)$ and $f_1(1285)$ are seen in:-

- $\bar{p}p \to \pi^0\eta'(958) \to \pi^0(\pi^0\pi^0\eta)$
- $\bar{p}p \to \pi^0 f_1(1285) \to \pi^0[a_0(980)\pi^0] \to \pi^0(\pi^0\eta)\pi^0$.

A large enhancement in the real data is seen in the $(\pi^0\pi^0\pi^0)$ mass distribution above 1400MeV. This may be attributed to the bias in phase space by the dominant channels in the data.

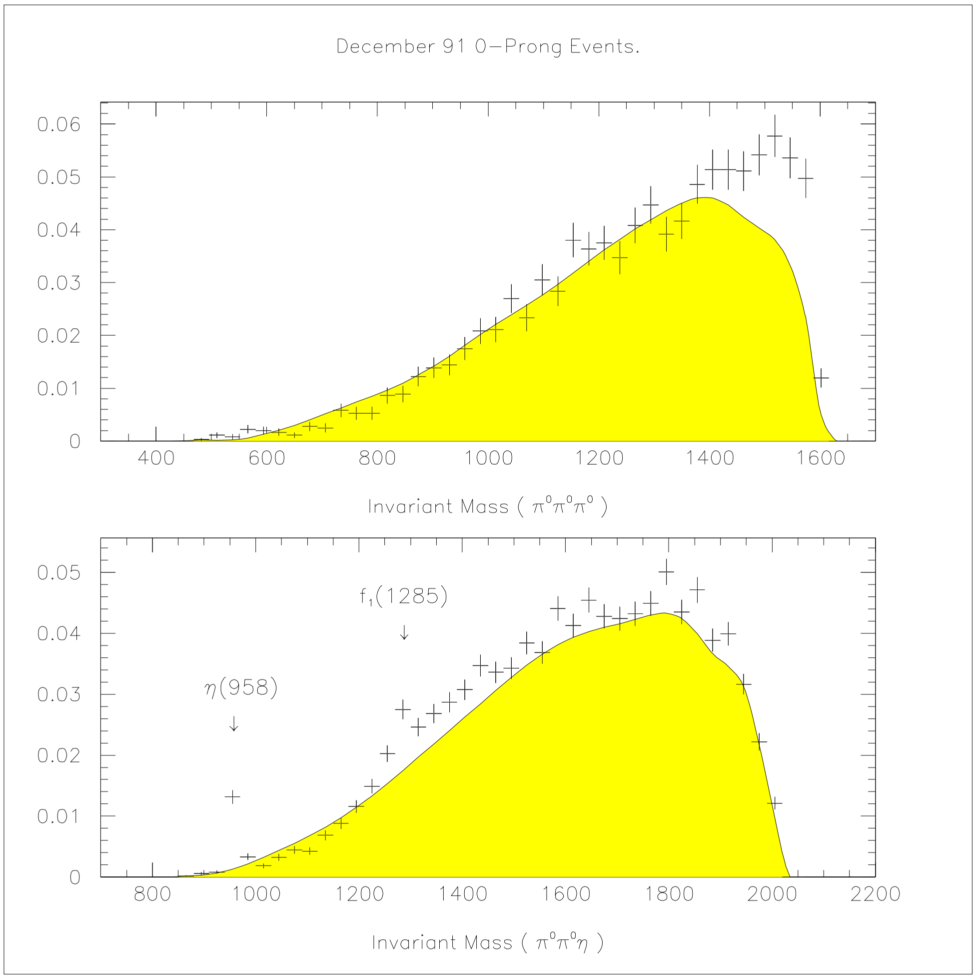

Figure 4.13: 1.20GeV/c data. Top: Invariant Mass of $(\pi^0\pi^0\pi^0)$. Above 1400 MeV the MC data does not simulate the real data. Bottom: Invariant Mass of $(\pi^0\pi^0\eta)$. Peaks due to the $\eta'(958)$ and $f_1(1285)$ are seen.

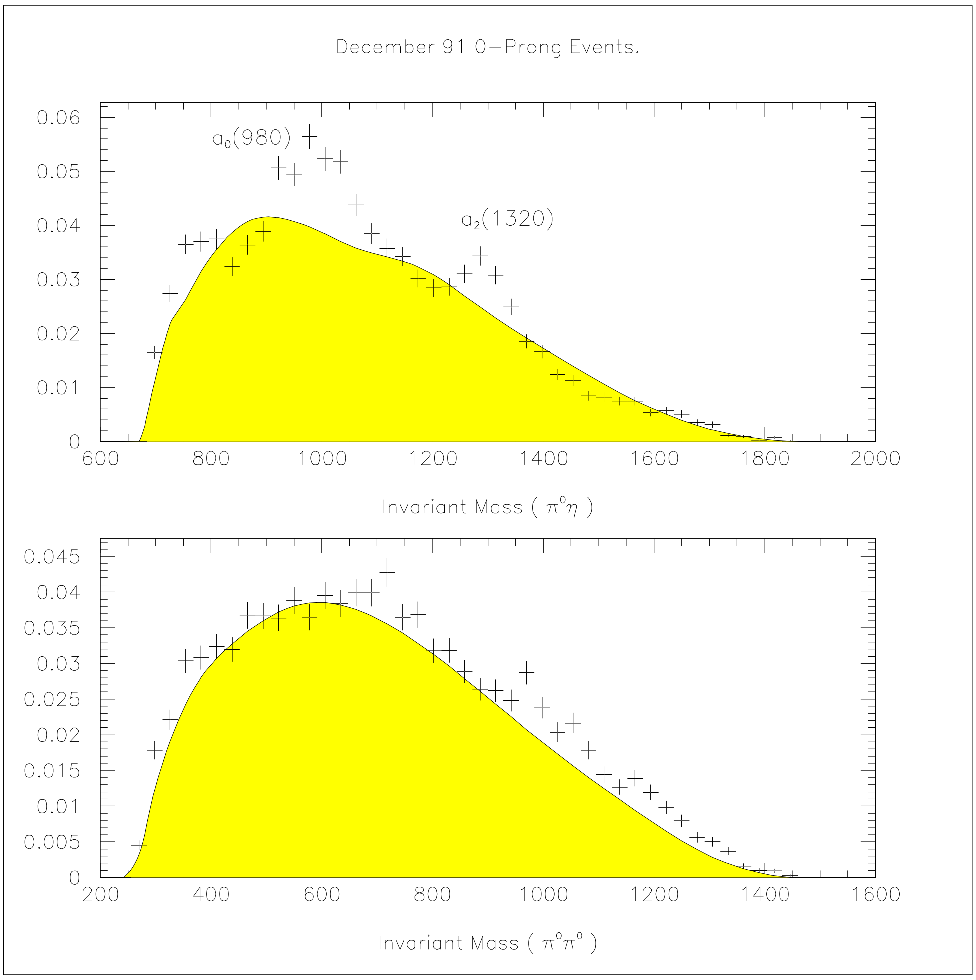

Figure 4.14: 1.20GeV/c data. Top: Invariant Mass of $(\pi^0\eta)$. Peaks due to the $a_0(980)$ and $a_2(1320)$ are seen. The discrepancy between the real and MC data at 800MeV is caused by low energy pions from the $\eta'(958)$. Bottom: Invariant Mass of $(\pi^0\pi^0)$. A small $f_0(975)$ peak can be seen.

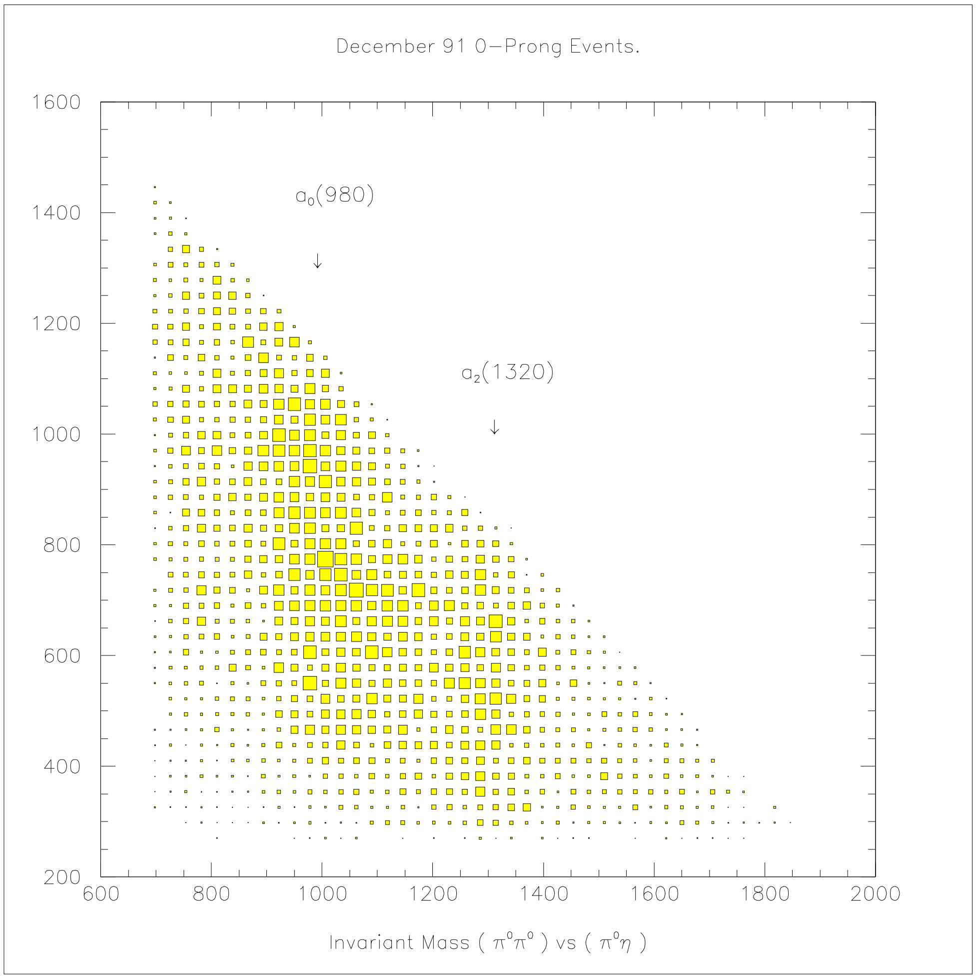

Figure 4.15: 1.20GeV/c data. Invariant Mass of $(\pi_i^0\pi_j^0)$ versus $(\pi_k^0\eta)$ showing the $a_0(980)$ and $a_2(1320)$ bands. Six combinations of i, j and k are summed in this plot.

4.3.2 $\pi^0\pi^0\pi^0\eta$ at 1.94 GeV/c

The mass plots for $\bar{p}p \to \pi^0\pi^0\pi^0\eta$ at 1.94 GeV/c (Figures 4.16 to 4.18) are presented in the same format as the 1.20 GeV/c data set.

The prominent channels in the data are:-

- $\bar{p}p \to a_0(980)f_2(1270) \to (\pi^0\eta)(\pi^0\pi^0)$
- $\bar{p}p \to a_2(1320)\sigma \to (\pi^0\eta)(\pi^0\pi^0)$.

Peaks in the $(\pi^0\pi^0\eta)$ mass distribution show the $\eta'(958)$ and $f_1(1285)$ in the channels:-

- $\bar{p}p \to \pi^0\eta'(958) \to \pi^0(\pi^0\pi^0\eta)$
- $\bar{p}p \to \pi^0 f_1(1285) \to \pi^0[a_0(980)\pi^0] \to \pi^0(\pi^0\eta)\pi^0$.

A discrepancy between the real and Monte Carlo data can be seen in the $(\pi^0\pi^0\eta)$ (1500-1900)MeV mass region and also in the $(\pi^0\pi^0\pi^0)$ (1500-1900)MeV mass region. A possible source of the latter enhancement is the $\pi_2(1670)$ in:-

- $\bar{p}p \to \eta\pi_2(1670) \to \eta[\pi^0 f_2(1270)] \to \eta\pi^0(\pi^0\pi^0)$.

No well established mesons with broad widths and a decay mode into $(\pi^0\pi^0\eta)$ can account for the enhancement in the $(\pi^0\pi^0\eta)$ mass distribution.

4.3.3 Comparison of $\bar{p}p \to \pi^0\pi^0\pi^0\eta$ at 1.20 and 1.94 GeV/c

As for the charged data, the increase in phase space produces a large $a_0(980)f_2(1270)$ signal in the 1.94GeV/c data. The higher energy data set exhibits a strong enhancement in the $(\pi^0\pi^0\eta)$ (1500-1900)MeV mass region not evident in the 1.20GeV/c data set. This may be attributed to several possibilities: (a) The strong $a_0(980)f_2(1270)$ and/or $\eta\pi_2(1670)$ signal(s) contributes a considerable phase space distortion, thus the $(\pi^0\pi^0\eta)$ enhancement may be a reflection. (b) The increased strength of the $a_2(1320)\sigma$ signal may be the source of the enhancement. (c) The enhancement may be due to one or more resonances decaying into $(\pi^0\pi^0\eta)$.

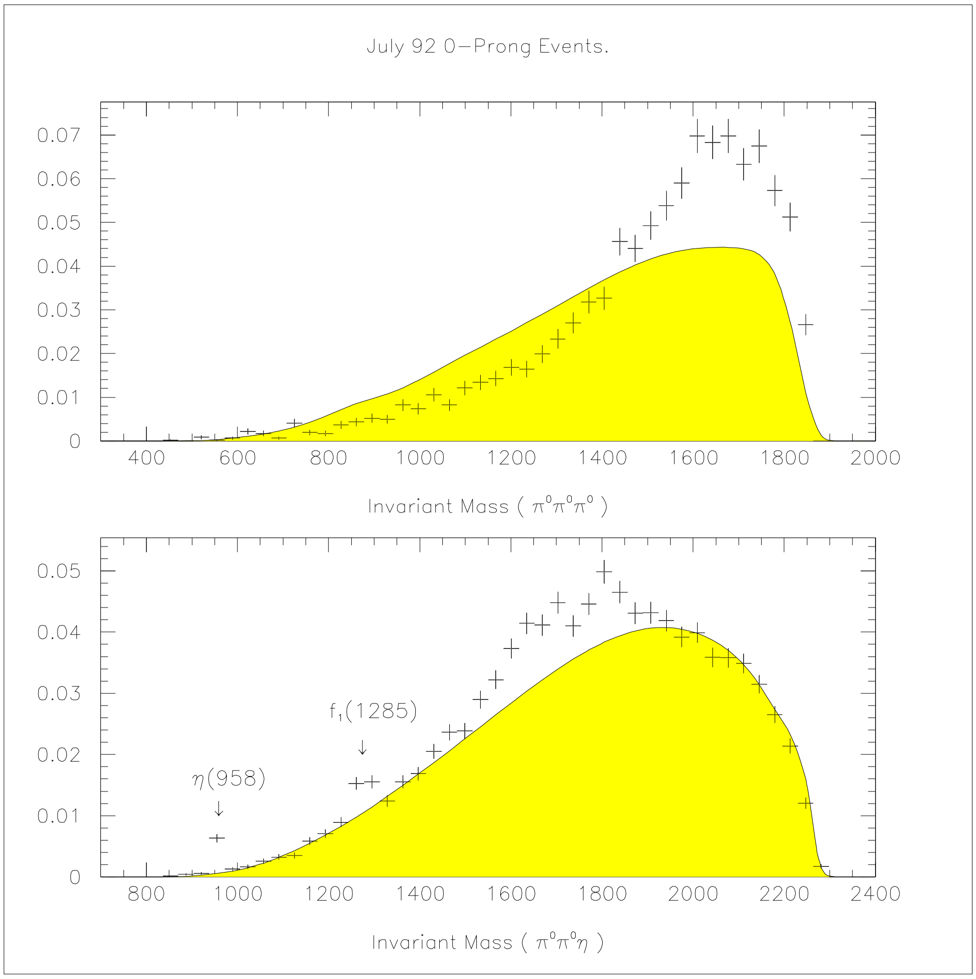

Figure 4.16: 1.94GeV/c data. Top: Invariant Mass of $(\pi^0\pi^0\pi^0)$. The MC and real data greatly differ above 1500 MeV. Bottom: Invariant Mass of $(\pi^0\pi^0\eta)$. Peaks due to the $\eta'(958)$ and $f_1(1285)$ are seen. A large discrepancy occurs between 1500 and 1900 MeV.

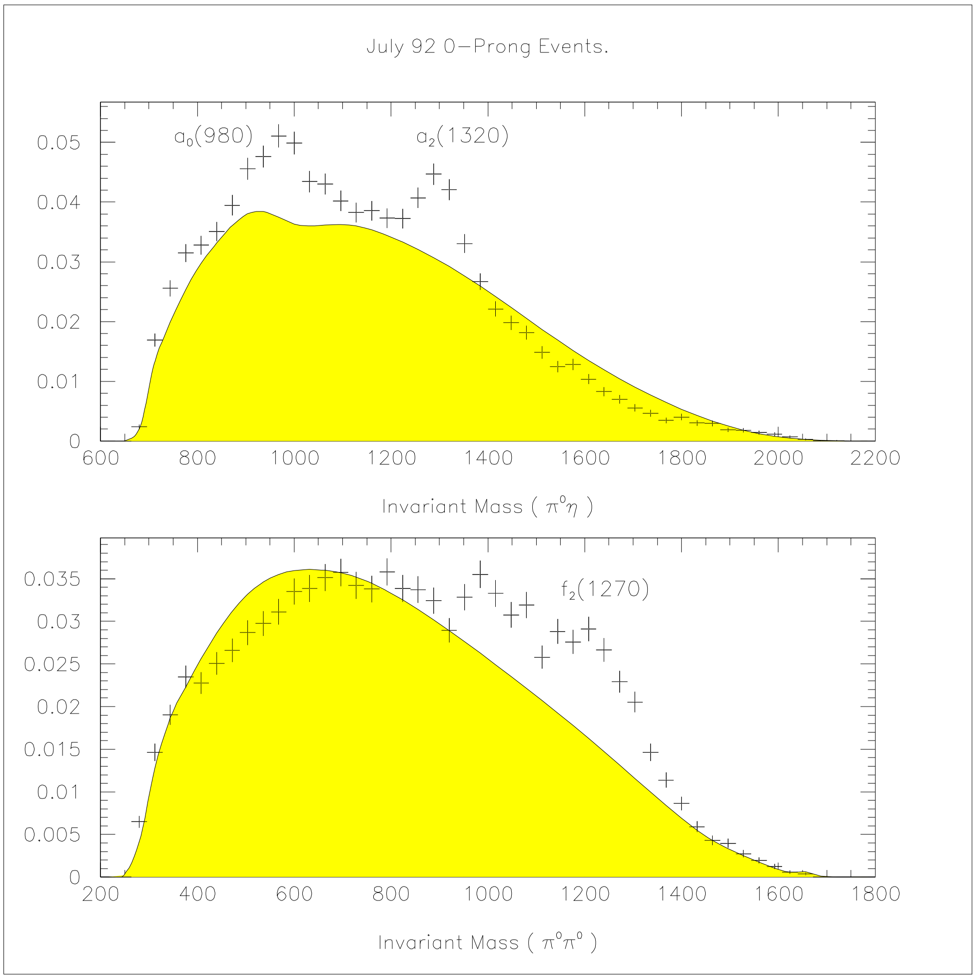

Figure 4.17: 1.94GeV/c data.Top: Invariant Mass of $(\pi^0\eta)$. Peaks due to the $a_0(980)$ and $a_2(1320)$ are seen. Bottom: Invariant Mass of $(\pi^0\pi^0)$ showing a signal for the $f_2(1270)$.

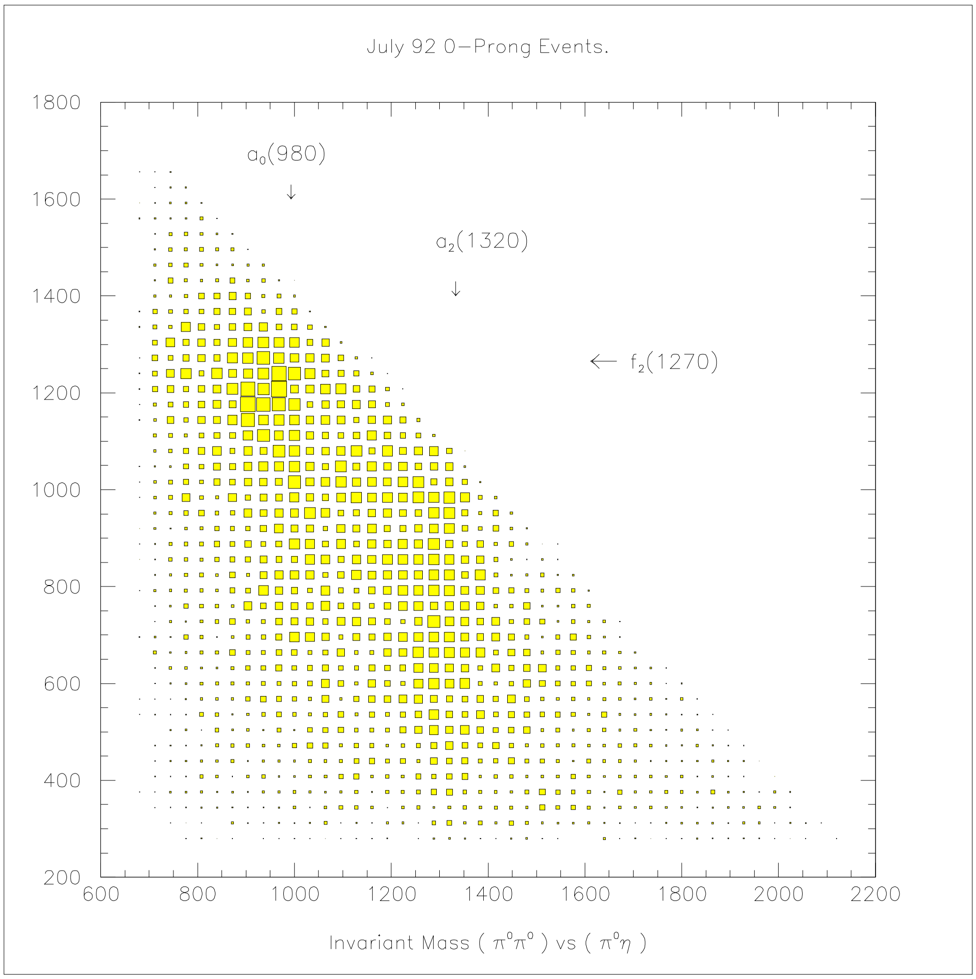

Figure 4.18: 1.94GeV/c data. Invariant Mass of $(\pi^0_i\pi^0_j)$ versus $(\pi^0_k\eta)$ showing the $a_0(980)$ and $a_2(1320)$ bands. A strong signal for $a_0(980)f_2(1270)$ events is seen. Six combinations of i, j and k are summed in this plot.

4.4 Summary

The narrow peaks in the invariant mass distributions showing the $\omega\eta$ and $\eta\eta$ channels in Figures 4.1 and 4.2 illustrate the good mass resolution of the data. Events successfully fitted to these channels are removed since they are of no interest in this analysis.

The charged data shows strong signals in the channels:-

- $\bar{p}p \rightarrow a_2(1320)\rho$
- $\bar{p}p \rightarrow a_0(980)\rho$
- $\bar{p}p \rightarrow a_0(980)f_2(1270)$.

The neutral data shows strong signals in the channels:-

- $\bar{p}p \rightarrow a_2(1320)\sigma$
- $\bar{p}p \rightarrow a_0(980)\sigma$
- $\bar{p}p \rightarrow a_0(980)f_2(1270)$.

The charged data has evidence suggestive of a resonance with mass between (1600-1800)MeV that decays into all charge combinations of $\eta\rho$. The 1.94GeV/c all neutral data has a large enhancement in the (1500-1900)MeV $(\pi^0\pi^0\eta)$ mass region. Both features are very interesting prospects for the 2^- pseudotensor mesons but the all neutral data enhancement was chosen for particular attention because of the simplified spin analysis: the charged data is more complex since it contains isospin I=1 resonances.

The following chapter presents the spin analysis of the $\pi^0\pi^0\pi^0\eta$ data at 1.94GeV/c and demonstrates that the $(\pi^0\pi^0\eta)$ enhancement is due to two $J^{PC}=2^{-+}$ states.

Chapter 5

Spin Analysis

5.1 Maximum Likelihood Method

The $\bar{p}p \to \pi^0\pi^0\pi^0\eta$ 1.94GeV/c data were fitted using the maximum likelihood minimisation method[40]. The fitting package allows up to 100 parameters (70 may be free) and returns the negative log likelihood, s, given by equations 5.1 and 5.2.

$$s = \sum_{i=1}^{M} - \ln Y_i \tag{5.1}$$

$$Y_i = \frac{\mid f_A(x_i, \Theta) + f_B(x_i, \Theta) \mid^2}{\sum_{j=1}^{N} \mid f_A(x_j, \Theta) + f_B(x_j, \Theta) \mid^2} \tag{5.2}$$

Here, the indices i and j sum over the total number of real and Monte Carlo data events respectively. In this example, f_A and f_B represent the amplitudes of two channels. The measured quantities $\mathbf{x}$ are masses (like m($\pi^0\eta$), m($\pi^0\pi^0$), m($\pi^0\pi^0\eta$) etc) and various angles to describe the decay of $a_2(1320)$, $f_2(1270)$ etc. The strength of the amplitudes are dependent on the mass and width of resonances involved in the channel. These parameters are included in the term Θ. If the mass and width of resonances involved in the fit are fixed, then the free parameters can be reduced to channel coupling strengths, momentum transfer and interference terms.

The zero point for the scale of s is arbitrary and therefore it is the change in

s that is used to determine whether a channel contributes to the data. For this analysis, a significant improvement to a fit was implied by a *reduction* in the value of s, namely by at least 20.

5.2 Basic Fit to $\bar{p}p \rightarrow \pi^0\pi^0\pi^0\eta$

To outline the spin analysis procedure, the process

$$\bar{p}p \rightarrow \mathrm{X}\pi^0 \rightarrow [a_2(1320)\pi^0]\pi^0 \rightarrow (\eta\pi^0)\pi^0\pi^0$$

is used as an illustration. An arbitrary J^P for particle X is allowed. Since the data were in-flight, many initial angular momentum states of the antiproton and proton system are possible. No attempt to include a rigorous representation of the production process is made in the fit. Instead, it is assumed that X is produced with helicity, λ, along the beam direction, and the density of states is described by a density matrix, $\rho(\lambda\lambda')$ which is averaged over all production angles of X. The decay of X is analysed in full.

Suppose X is produced at angles (θ,ϕ) to the beam (with the z-axis along the beam direction). These angles are determined from the kinematics of the event for all six combinations of $(\eta\pi_i^0)\pi_j^0$. Suppose the production amplitude for helicity λ is f_λ^X. If the axes are rotated such that the new z-axis lies in the direction of X, the amplitude is multiplied by a D matrix, $\mathrm{D}^J_{\lambda\lambda'}(\theta,\phi)$. The amplitude is then invariant[41] under a Lorentz boost to the rest frame of X. However, the D matrix can be removed by rotating the axes back through angles (-θ,-ϕ) in the rest frame of X. This process is the Wick rotation, (described in reference [41]), between the laboratory frame and rest frame of X.

If the particle X decays to $a_2(1320)\pi^0$, the decay process can be described in the usual way using Clebsch-Gordan coefficients:

$$f_\lambda = (J,\lambda \mid L,m,2,\lambda-m)P_L^m(\gamma,\epsilon) \mid 2,\lambda-m > \quad (5.3)$$

where γ and ϵ are the angles for $a_2(1320)$ with respect to the beam direction in the rest frame of X. The decay X $\rightarrow a_2(1320)\pi^0$ may now be treated as in the previous paragraph, with a second Wick rotation to the rest frame of $a_2(1320)$. Finally, the decay $a_2(1320) \rightarrow \eta\pi^0$ is described by Legendre polynomials $P_2^{\lambda-m}(\alpha,\beta)$, where (α,β) are the angles of η with respect to the beam direction in the rest frame of $a_2(1320)$. The result of this procedure is the following expression:

$$f_\lambda = (J,\lambda \mid L,m,2,\lambda-m)P_L^m(\gamma,\epsilon)P_2^{\lambda-m}(\alpha,\beta) \tag{5.4}$$

where Wick rotations are included in (γ,ϵ) and (α,β). The initial $\bar{p}p$ state can have at most helicity λ=1. Therefore, channels with λ=2 contain an additional sinθ term due to one unit of orbital angular momentum in the final state. Helicity 3 was tried where necessary but rejected due to it's negligible contribution to the fit.

Interference amongst all channels with the same helicity were included in the fit. For interference between two channels, the interference terms were retained if the interference improved the fit by more than Δs=-10. The interference will be complete only if the initial state is the same for both channels. Since there are many possible initial states, the interference was constrained to lie within the range 0 (no coherence) to 1 (full coherence). Interference amongst channels with different values of helicity were not included in the fit due to their negligible contribution.

The only attempt to model the production process was the inclusion of a factor to describe the production angular distribution:

$$e^{\alpha\tau^2} \quad where \quad \tau = 2p_1p_2cos(\theta) \tag{5.5}$$

Here p_1 and p_2 are the centre of mass momenta of the initial antiproton and X.

The Wick rotation procedure is equivalent to using D matrices but has the advantage that it is faster to compute once the geometrical rotations have been calculated for any individual event. Also, the information concerning the initial helicity is preserved: for X(J^{PC}=2^{-+}) $\rightarrow a_2(1320)\pi^0$, where L=0, the helicity of X is transferred directly to the $a_2(1320) \rightarrow \eta\pi^0$ decay. Typically, a fit takes less than one minute of real time to converge.

5.2.1 The Basic Fit Ingredients

The first fit included the obvious channels:

$$\bar{p}p \rightarrow \mathrm{f}_2(1270).a_0(980) \rightarrow (\pi^0\pi^0)(\pi^0\eta) \qquad \text{Channel 1}$$

$$\bar{p}p \rightarrow \sigma.a_2(1320) \rightarrow (\pi^0\pi^0)(\pi^0\eta) \qquad \text{Channel 2}$$

resulting in a log likelihood of s=326. The σ represents the $\pi^0\pi^0$ S-wave amplitude. The parameterisation of the $\pi^0\pi^0$ S-wave amplitude can be found in reference [39]. When one of the two channels is removed from the fit, the remaining channel's coupling strengths show little variation: evidence that the two channels are only slightly correlated and that interference between the two channels is negligible.

Further channels were included in the fit:

$$\bar{p}p \rightarrow \pi^0 f_1(1285) \rightarrow \pi^0[\pi^0 a_0(980)] \rightarrow \pi^0\pi^0(\pi^0\eta) \qquad \text{Channel 3}$$

$$\bar{p}p \rightarrow \sigma.a_0(980) \rightarrow (\pi^0\pi^0)(\pi^0\eta) \qquad \text{Channel 4}$$

and improve the log likelihood by Δs=-70 and Δs=-185 respectively. The removal of channel 3 from the fit increases the log likelihood by only Δs=+39. This suggests that channel 4 compensates to some extent for the removal of channel 3. The magnitude of the change in log likelihood gives an idea of the sensitivity of the fit; The $f_1(1285)$ peak is narrow and clearly seen by eye in Figure 4.16 (and later in Figure 5.9) and therefore may be considered as a highly significant signal.

A comparison of the real data and Monte Carlo data biased by the fit parameters, (Figure 5.1), shows a discrepancy in the $\pi^0\eta$ mass projection. The real data contains a broad enhancement in the mass region between the $a_0(980)$ and $a_2(1320)$ peaks. To remove this difference it was found necessary to include a term that describes an incoherent phase space background in the real data. Monte Carlo simulations show that all of the resonances expected around 1700MeV and 2000-2100MeV in $\eta\pi\pi$ tend to give $(\eta\pi)$ combinations with a broad peak from 1000-1500MeV. The background term may be due to these resonances, presently invisible. Whatever it's origin, this background term gave a large improvement to the fit, Δs=-327. However, it plays no role in the identification of the resonances now to be discussed.

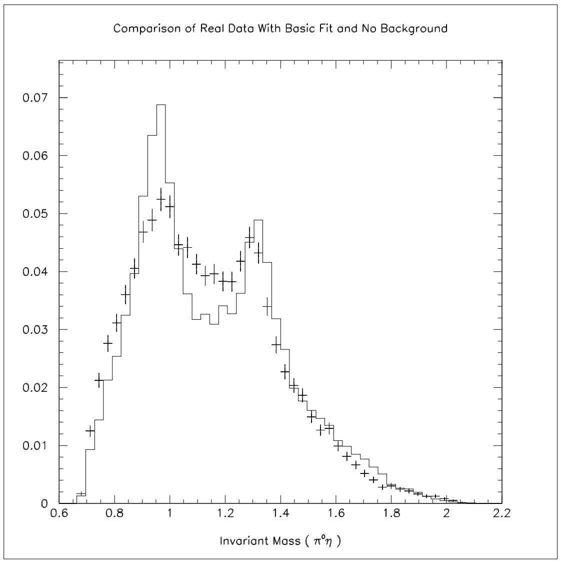

Figure 5.1: Comparison of $(\eta\pi^0)$ mass distribution for the real data and fit. The real data are represented by error bars. The fit contains channels 1→4.

5.3 Inclusion of $\eta_2(1650)$

As stated in the introduction, the motivation for this analysis is to find states with J^{PC}=2^{-+}. A 2^{-+} meson can be formed by combining an $a_2(1320)$ [J^{PC}=2^{++}] with a π^0 [J^{PC}=0^{-+}], assuming zero orbital angular momentum between the $a_2(1320)$ and π^0. With zero electric charge, the 2^{-+} state has isospin, I=0. According to the naming convention of the Particle Data Group, this state is called the η_2. Within this section, evidence for the first observation of the η_2 is presented.

The comparison of the $(\pi^0\pi^0\eta)$ mass distribution for the real and acceptance corrected phase space Monte Carlo data (Figure 4.16) shows a large enhancement in the (1500-1900)MeV mass region. This mass region was investigated by selecting several mass bands of $(\pi^0\pi^0\eta)$. In the case that the $\pi_i^0\pi_j^0\eta$ combination occurred in a selected mass band, then $(\pi_i^0\pi_j^0)$ was plotted versus $(\pi_i^0\eta)$ and $(\pi_j^0\eta)$. These scatter plots can be found in Figure 5.2. There is an important distinction between these scatter plots and Figure 4.18. On the latter figure, the pion used in the $\eta\pi$ combination is distinct from the two pions used in the combination plotted vertically. In all, six combinations contribute to this figure. On Figure 5.2, the objective is to study $X \rightarrow \eta\pi_i^0\pi_j^0$; the third pion, π_k^0, is the spectator. Along the horizontal axis the η is combined with both π_i^0 and π_j^0 forming X (2 combinations).

Figure 5.2 reveals an enhanced $a_2(1320)$ signal in the (1550-1750)MeV $\pi^0\pi^0\eta$ mass region relative to the (1350-1550)MeV and (1750-1950)MeV $\pi^0\pi^0\eta$ mass regions. This suggests a resonance in the (1550-1750)MeV mass region that decays into $a_2(1320)\pi^0$. Based on this evidence, the channel involving the η_2 decaying into $a_2(1320)\pi^0$ was included:

$$\bar{p}p \rightarrow \pi^0\eta_2 \rightarrow \pi^0[\pi^0 a_2(1320)] \rightarrow \pi^0\pi^0(\pi^0\eta) \qquad \text{Channel 5}$$

The mass and width of the η_2 were found to be M(η_2)=1650MeV and $\Gamma(\eta_2)$=180MeV. The addition of the η_2 hypothesis without interferences improved the fit by Δs=-13. Allowing interference between $\bar{p}p \rightarrow \pi^0\eta_2$ and $\bar{p}p \rightarrow \sigma.a_2(1320)$ improved the log likelihood further by Δs=-63. The mass of the η_2 was varied to ascertain the optimum mass. Figure 5.3 shows the variation of log likelihood with η_2 mass, with and without the phase space term. The removal of the background term increases the log likelihood by Δs=+221. The log likelihood profile without the background term has had 221 subtracted from the log likelihood values so that the two profiles have the same value when the fitted η_2 mass was 1650MeV.

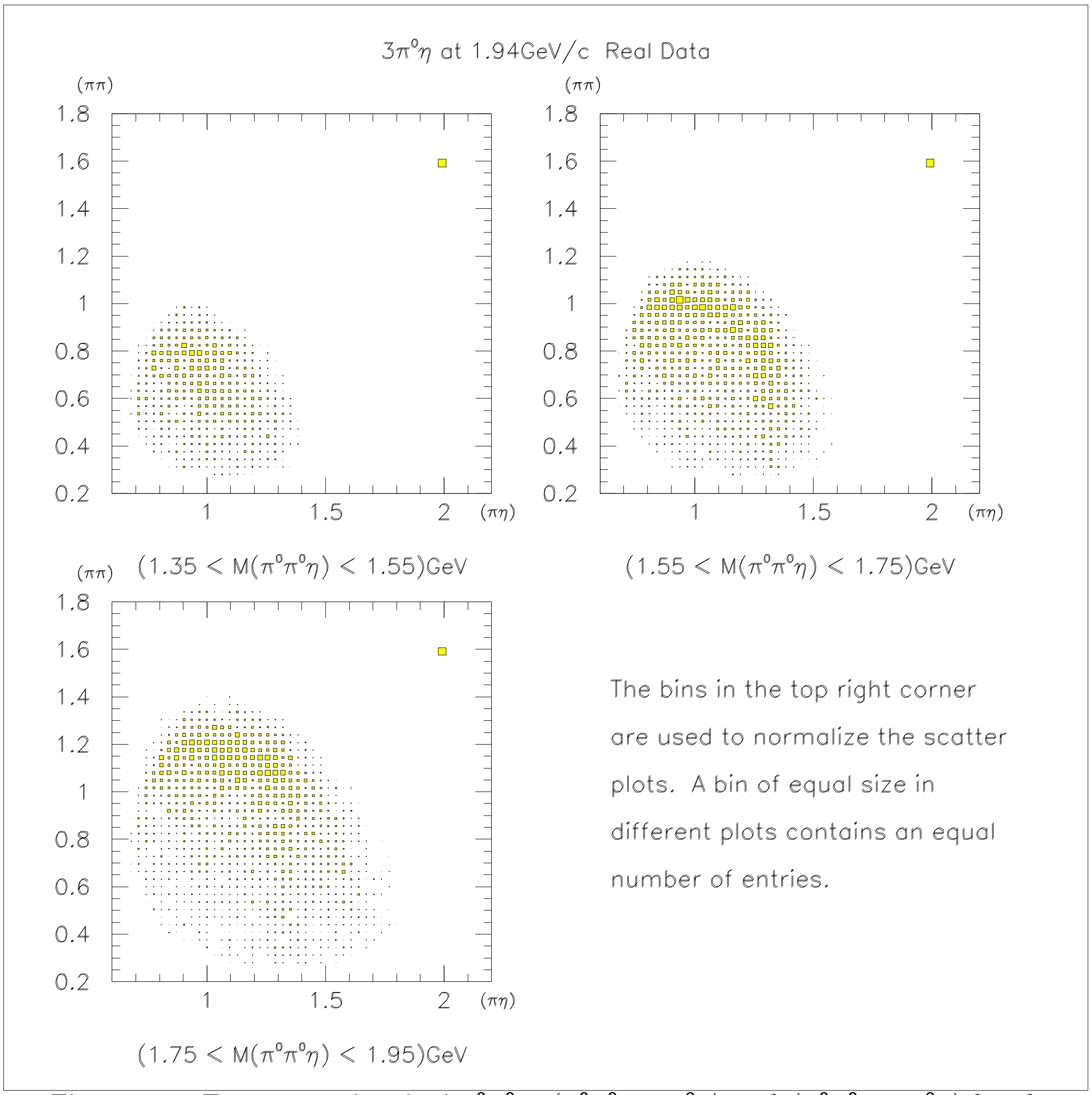

Figure 5.2: For a mass band of $\pi_i^0\pi_j^0\eta$, ($\pi_i^0\pi_j^0$ vs $\pi_i^0\eta$) and ($\pi_i^0\pi_j^0$ vs $\pi_j^0\eta$) has been plotted. The (1.55-1.75)GeV mass band shows an enhanced $a_2(1320)$ signal relative to the lower and upper $\pi^0\pi^0\eta$ mass bands.

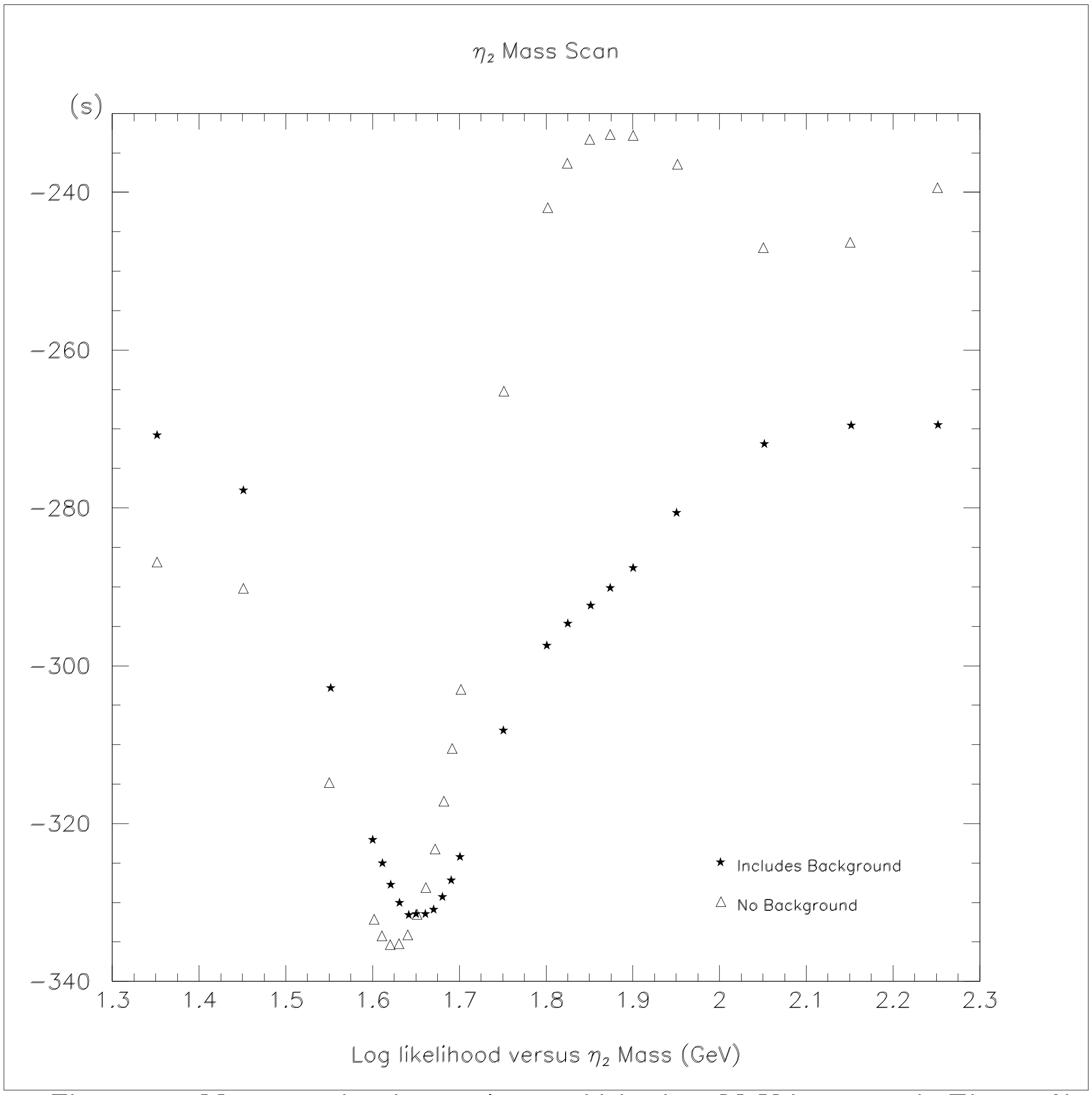

Figure 5.3: Mass scan for the η_2. An η_2 width of 180MeV is assumed. The profile with triangular data points represents the mass scan without the phase space term and has had the log likelihood values adjusted to agree with the plot including background at 1650MeV.

Both the log likelihood profiles show a large dip at about 1650MeV. The depth and gradient of the dips strongly suggest that a resonance is required in this mass region. Using the fit that includes the background term, the resonance mass is 1650MeV. This profile was chosen since (a) it gives a better log likelihood, (b) the sides of the dip are more evenly balanced and (c) the dip appears in both profiles and therefore is not a feature produced by the background term.

The mass scan profile without the background term shows a wide dip around 2135MeV. The mass scan profile including the background term appears to have a linear region between 1800 and 1900MeV. Both these features are discussed in later sections and correspond to further resonances.

The width of the η_2 was varied assuming a mass of 1650MeV. The η_2 width shows (Figure 5.4) little variation with log likelihood, but a value of 180MeV gives the best fit. The background term increases the width of the dip, but has only a small effect on the optimum.

The sharp mass definition is explained by the interference between the $\pi^0\eta_2(1650)$ and $a_2(1320)\sigma$ channels. The width is less well defined because other ingredients in the fit are capable of taking up the slack when the width is altered.

To test the hypothesis of the resonance being $J^{PC}=2^{-+}$, alternative spin states were substituted and the assumed mass of the resonance was varied. The log likelihood values corresponding to resonance mass and spin, (assuming a width of 180MeV), can be found in Table 5.1.

The results in Table 5.1 provide strong evidence that the resonance has $J^{PC}=2^{-+}$ with a mass of 1650MeV. Additional (and alternative) channel combinations were included with (or replaced) the $\pi^0\eta_2(1650)$ channel. Such channels (eg $X \to a_0(980)\pi^0$ and $X \to a_2(1320)\pi^0$) with orbital angular momentum L=0,1,or 2 gave no significant signal.

Assuming that the resonance is a normal $q\bar{q}$ state, then this constitutes the first observation of the η_2. A discussion of the errors in the measurement of the η_2 mass and width can be found in a later section.

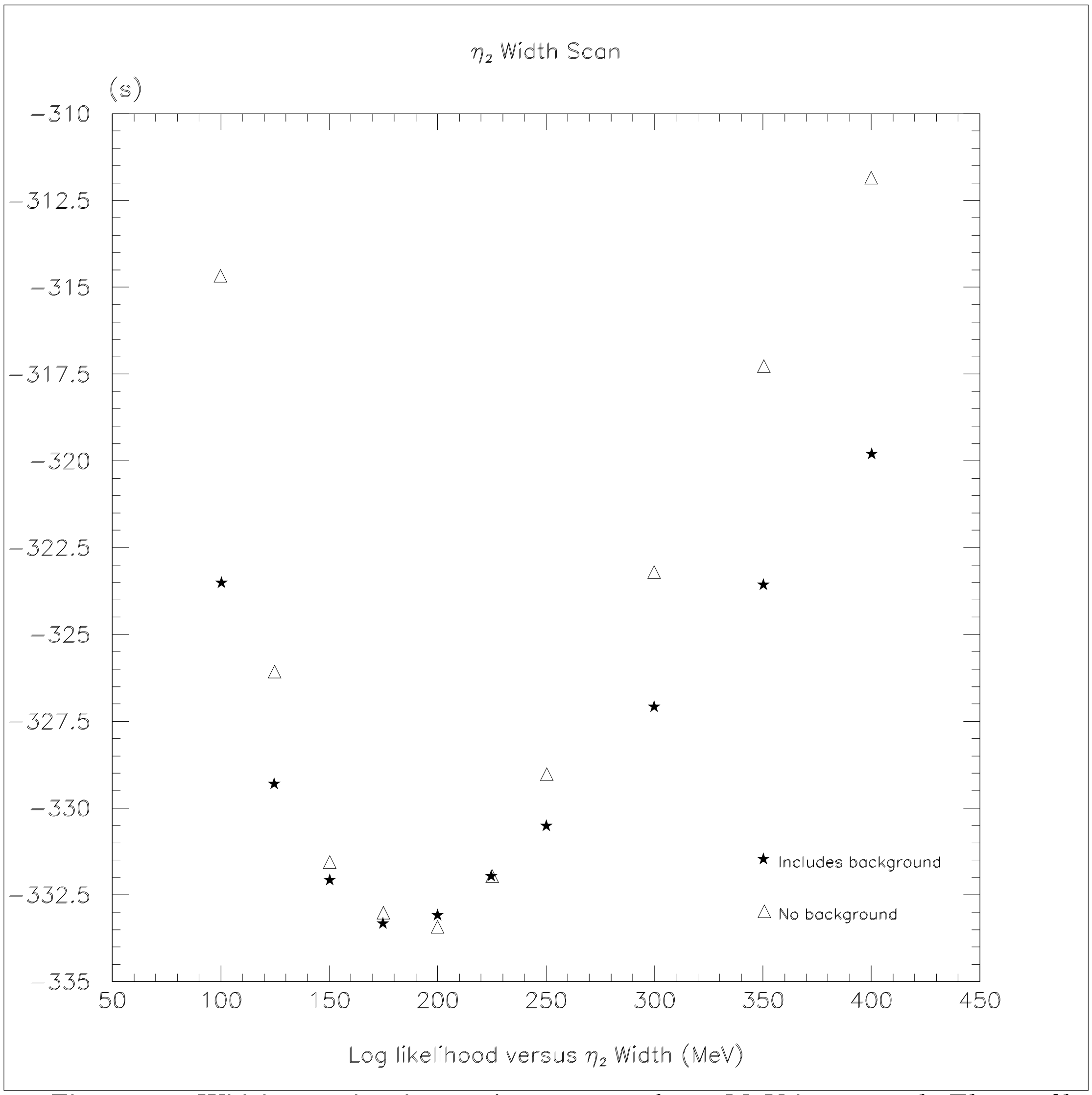

Figure 5.4: Width scan for the η_2. An η_2 mass of 1650MeV is assumed. The profile with triangular data points represents the mass scan without the background term and has had the log likelihood values adjusted for the benefit of comparison.

$M(\pi^0\pi^0\eta)$ (MeV)	2^{-+} $[a_2(1320)\pi^0]_{L=0}$	1^{++} $[a_2(1320)\pi^0]_{L=1}$	2^{++} $[a_2(1320)\pi^0]_{L=1}$	3^{++} $[a_2(1320)\pi^0]_{L=1}$
1350	-271	-258	-206	-263
1450	-278	-271	-205	-266
1550	-303	-279	-209	-268
1650	-332	-261	-213	-254
1750	-308	-227	-209	-221
1850	-292	-205	-206	-201

Table 5.1: The log likelihood values determined using various spin and mass assumptions. The L=1 centrifugal barrier used a radius of interaction of 0.6fm.

5.4 Inclusion of $\pi_2(1670)$

The comparison of the $(\pi^0\pi^0\pi^0)$ mass distribution for the real and acceptance corrected phase space Monte Carlo data (Figure 4.16) shows a large discrepancy around 1700MeV. A candidate for the source of this enhancement in the real data is the isospin I=1 partner of the $\eta_2(1650)$. Assuming the strongest decay mode of the $\pi_2(1670)$ into $f_2(1270)\pi$, the $\eta\pi_2(1670)$ channel was included in the fit:

$$\bar{p}p \to \eta\pi_2(1670) \to \eta[\pi^0 f_2(1270)] \to \eta\pi^0(\pi^0\pi^0) \qquad \text{Channel 6}$$

The addition of the $\eta\pi_2(1670)$ channel improves the fit by Δs=-142. Including interference with other channels, $a_0(980)f_2(1270)$ and $\pi^0\eta_2(1650)$ further improves the fit by Δs=-25.3 and Δs=-10.4 respectively. For further evidence of the $\pi_2(1670)$, a cut on events with $f_2(1270)$ was made. If a $(\pi^0\pi^0)$ mass was measured to be between (1100-1400)MeV and the $(\pi^0\eta)$ mass was not in the $a_2(1320)$ [(1318.2$\pm$75)MeV] mass region, the $(\pi^0\pi^0\pi^0)$ was plotted: see bottom of Figure 5.13. No $\pi_2(1670)$ peak is evident in this $(\pi^0\pi^0\pi^0)$ mass distribution. However, due to the significant improvement to the log likelihood and the $(\pi^0\pi^0\pi^0)$ enhancement in the complete mass distribution plot, the $\pi_2(1670)$ was retained in the fit.

5.5 Inclusion of X(2135)

The log likelihood profile in the $\eta_2(1650)$ mass scan (without the background term), Figure 5.3, reveals a dip as the fitted η_2 (*ie* $\pi^0\pi^0\eta$) mass is scanned at a high mass. To identify the source of this dip, scatter plots (of the same format as those found in Figure 5.2) were constructed for three mass regions of $\pi^0\pi^0\eta$ and can be found in Figure 5.5.

In the $\pi^0\pi^0\eta$ (1950-2150)MeV mass region, a large $a_2(1320)$ and $f_2(1270)$ enhancement occurs where the two signals cross. This suggests interference between

$$X \rightarrow a_2(1320)\pi^0 \qquad \text{Channel 7}$$

and

$$X \rightarrow f_2(1270)\eta \qquad \text{Channel 8}$$

It is not due to $a_2(1320)f_2(1270)$. The threshold for this process is at 2590MeV, far above the available centre of mass energy 2409MeV. Trials were made adding this channel to the analysis, but it gave negligible improvement. If this process were important, it should show up on the right-hand edge of Figure 4.18, near the intersection of $a_2(1320)$ and $f_2(1270)$ bands, but no strong signal is evident there.

The magnitude of the enhancement is also too large to be produced by interference between channels 1 and 2 and therefore one or more resonances in this high $\pi^0\pi^0\eta$ mass region are required. The quark model predicts several mesons in the 2000-2100MeV mass range: ${}^3F_4(4^{++})$, ${}^3F_3(3^{++})$ and ${}^3F_2(2^{++})$. Also predicted is the ${}^1G_4(4^+)$ which is expected in the (2200-2350)MeV mass region. To determine the *dominant* contribution to the $a_2(1320).f_2(1270)$ interference cross, a single resonance was included into the fit and a large number of spin states tested. Fully coherent interference between channel 6 and 7 was assumed. For $X \rightarrow a_2(1320)\pi^0$ and X

Figure 5.5: For a mass band of $\pi_i^0\pi_j^0\eta$, ($\pi_i^0\pi_j^0$ vs $\pi_i^0\eta$) and ($\pi_i^0\pi_j^0$ vs $\pi_j^0\eta$) has been plotted.

$\rightarrow f_2(1270)\eta$ with orbital angular momentum, L=0,1 or 2, there are the following possibilities:-

- 2^{-+} [L=0]
- 3^{++}, 2^{++}, 1^{++} [L=1]
- 4^{-+}, 3^{-+}, 2^{-+}, 1^{-+}, 0^{-+} [L=2]

These and several more spin states were tested and the resulting improvements to the log likelihood can be found below.

- **L = 3**
  - 4^{++} Δs = -0.2
- **L = 2**
  - 4^{-+} Δs = -3.4
  - 3^{-+} Δs = -8.0
  - 2^{-+} Δs = -1.1
  - 1^{-+} Δs = -1.6
  - 0^{-+} Δs = -10.3
- **L = 1**
  - 3^{++} Δs = -10.0
  - 2^{++} Δs = -46.0 $\rightarrow$ Only significant contribution.
  - 1^{++} Δs = -6.1
- **L = 0**
  - 2^{-+} Δs = -13.0

The only significant signal (Δs=-46) comes from 2^{++}. This is surprising since a 2^{++} resonance is expected to decay preferentially into $\pi\pi$ and 4π. The optimised mass and width for the 2^{++} state are 2135MeV and 250MeV respectively. It can be construed that this is the same resonance seen by GAMS[42] in $X \rightarrow \eta\eta$ with a mass of (2175$\pm$20)MeV and width (150$\pm$35)MeV. Substituting the GAMS resonance for the optimum fit, the log likelihood deteriorates by just Δs=+5.

It is found that the $\eta\pi_2(1670)$ channel has similar kinematics to the $\pi^0X(2135)$ channel and is therefore able to compensate within the fit when the $\pi^0X(2135)$ channel is removed. Without the inclusion of the $\eta\pi_2(1670)$ channel, the removal of the $\pi^0X(2135)$ channel makes the fit deteriorate by Δs=+105. Therefore the already significant contribution of the $\pi^0X(2135)$ channel with Δs=-46 should be considered as a lower limit.

The effect of the $\pi^0X(2135)$ channel upon the $\pi^0\eta_2(1650)$ channel is found to be negligible. The mass and width scan for the $X(2135)$ can be seen in Figure 5.6. The mass scan assumed an $X(2135)$ width of 250MeV and the corresponding width scan assumed a mass of 2135MeV. Similar to the $\eta_2(1650)$ width scan, the log likelihood is fairly insensitive to the assumed width of the $X(2135)$. Note that the mass and width scans were carried out with the optimum fit (including the $\pi_2(1670)$) which is described in the summary.

5.6 Inclusion of X(1850)

The scatter plot from the (1.75-1.95)GeV $\pi^0\pi^0\eta$ mass region in Figure 5.5 has a strong $f_2(1270)$ band, corresponding to $X \rightarrow f_2(1270)\eta$. The mass of the $f_2(1270)$ appears to be low, in this plot and in Figure 4.18, suggesting that the $f_2(1270)$ is strongly produced at threshold. With this in mind (and the strangely linear region of the log likelihood profile from the $\eta_2(1650)$ scan), events with a $(\pi^0\pi^0)$ mass in the region (1075-1425)MeV *ie* the $f_2(1270)$ region, were selected and the corresponding $(\pi^0\pi^0\eta)$ mass plotted. Figure 5.7 compares the above $(\pi^0\pi^0\eta)$ mass distribution with

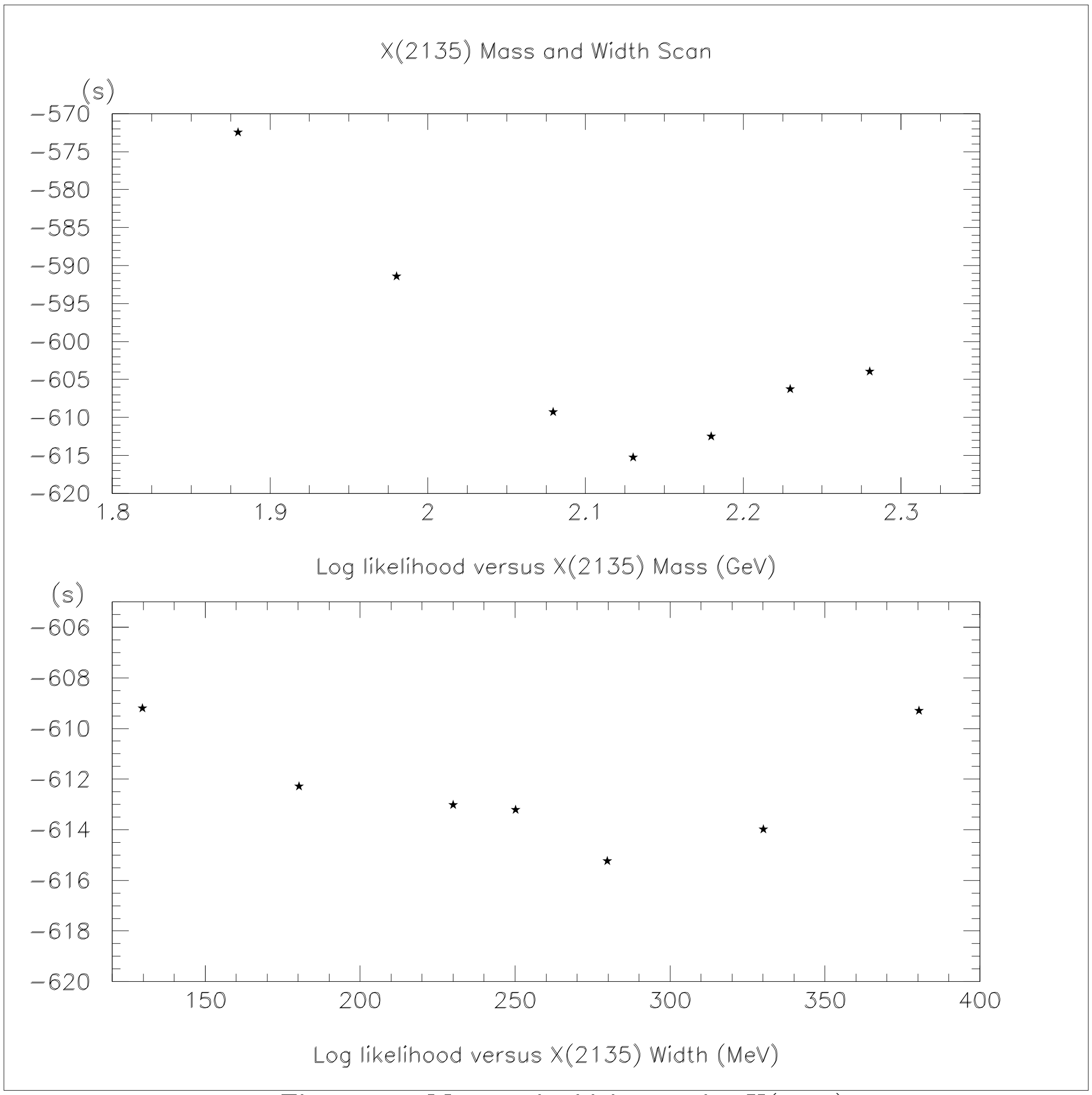

Figure 5.6: Mass and width scan for $X(2135)$.

that of acceptance corrected phase space Monte Carlo data. Note that the two mass distributions have been arbitrarily normalized such that the area under the profile is unity. A clear enhancement is seen from 1760 to 1900MeV in the real data.

A resonance was added to the fit with an 1850MeV mass and 225MeV width in the channel:

$$\bar{p}p \rightarrow \pi^0 X(1850) \rightarrow \pi^0[\eta f_2(1270)] \rightarrow \pi^0\eta(\pi^0\pi^0) \qquad \text{Channel 9}$$

A resonance close to the $\eta f_2(1270)$ threshold is very likely to have orbital angular momentum L=0, hence quantum numbers $J^{PC}=2^{-+}$. However, as with the tests for the $\pi^0 X(2135)$ channel, many spin states were tested for the $X(1850)$ state. The optimum fit was given by 2^{-+} with Δs=-54. This fit included $X(1850)$ interfering with the $a_0(980)f_2(1270)$, $\eta\pi_2(1670)$ and $\pi^0\eta_2(1650)$ channels. Table 5.2 presents the results of alternative mass and spin assignments to the resonance with an $\eta f_2(1270)$ decay mode.

A potential explanation of the strong $f_2(1270)$ band without requiring an additional resonance is that the $\eta f_2(1270)$ signal is due a second decay mode of the $\eta_2(1650)$ in it's high energy tail. This solution has been rejected. A Flatté formula was used to fit the $\eta_2(1650)$, enabling it to decay into $a_2(1320)\pi^0$ and $\eta f_2(1270)$.

$$f_i = \frac{\Lambda_i}{s - M^2 + iM(\Gamma_1 + \Gamma_2)} \tag{5.6}$$

Here $(M\Gamma_i)_r$ implies evaluation on resonance with mass, M=1650MeV. The term $\Gamma(a_2(1320)\pi^0)$ is kept constant, but allowance is made for the opening of the $f_2(1270)\eta$ channel by using a Fermi function:

$$\Gamma_2 = \frac{\Gamma_1 \sum_m \mid \Lambda_{2m} \mid^2 /(7\sum_m \mid \Lambda_{1m} \mid^2)}{1 + exp([3.323 - s]/0.3458)} \tag{5.7}$$

The numerator weights Γ_2 by the sum of intensities of helicities m=0, 1 and 2 for the second channel and divides by the corresponding sum for the first channel. The factor 7 is used to allow for the 14% branching ratio of $a_2(1320)$ into $\eta\pi$. The

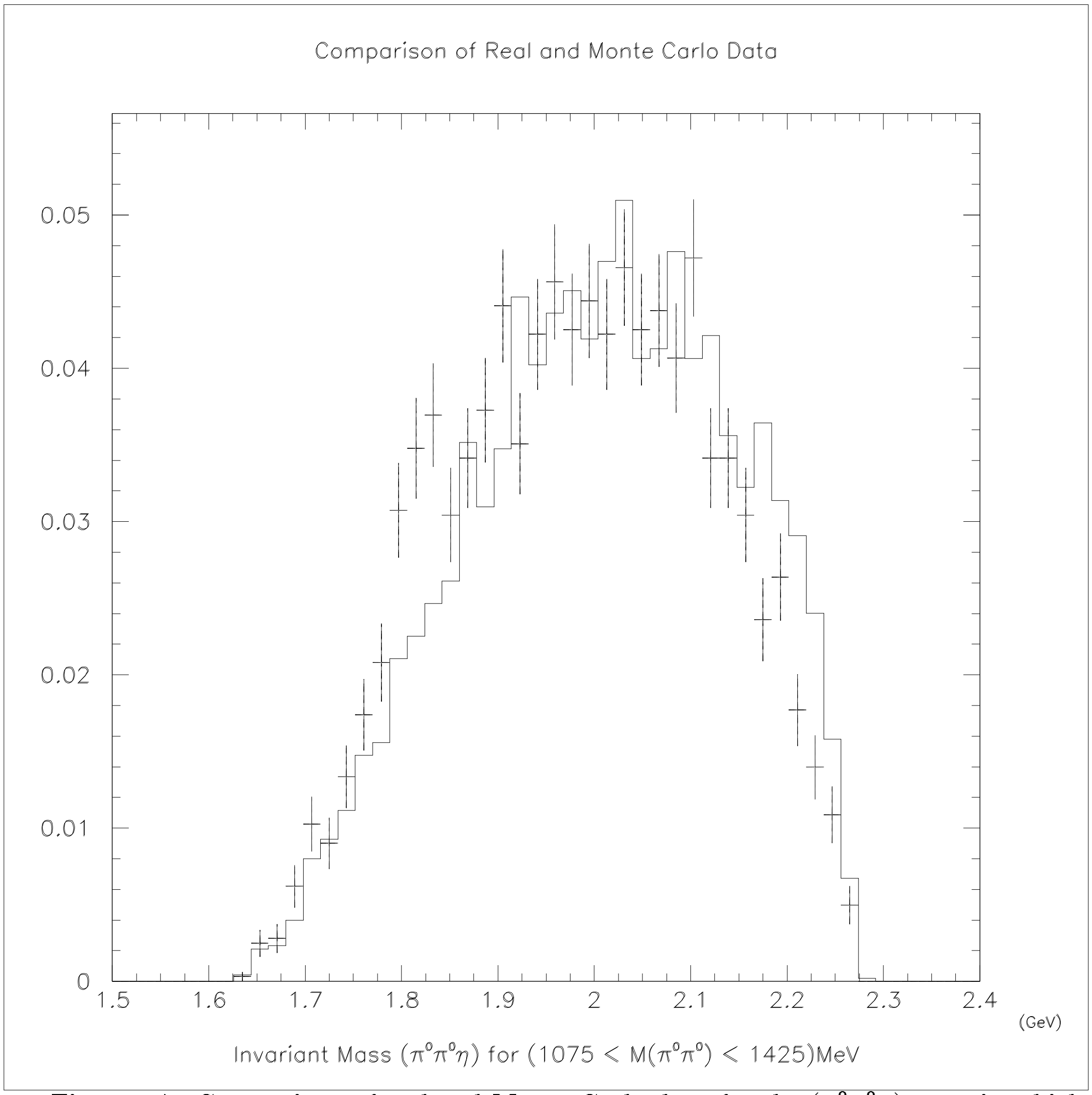

Figure 5.7: Comparison of real and Monte Carlo data for the $(\pi^0\pi^0\eta)$ mass in which the $(\pi^0\pi^0)$ mass is in the $f_2(1270)$ mass region. Error bars represent the real data.

$M(\pi^0\pi^0\eta)$ (MeV)	3^{++} $[\eta f_2(1270)\pi^0]_{L=1}$	2^{++} $[\eta f_2(1270)\pi^0]_{L=1}$	1^{++} $[\eta f_2(1270)\pi^0]_{L=1}$
1600	47.2	16.2	5.3
1650	39.2	21.0	8.3
1700	31.8	23.8	9.8
1750	28.5	22.4	10.2
1800	26.0	21.5	11.5
1850	23.8	20.8	12.2
1900	22.2	17.9	11.5
1950	20.2	15.1	10.9
2000	21.1	15.1	10.8

Table 5.2: Improvements to log likelihood using various spin and mass assumptions for the $X(1850)$. The L=1 centrifugal barrier used a radius of interaction of 0.6fm.

denominator is an approximation to the opening of the $\eta f_2(1270)$ channel. The width of the $f_2(1270)$ is included in the factor 0.3458; however, the fit results are insensitive to this number.

The resulting fit gives a poor description of the energy dependence of $\eta f_2(1270)$ production: Δs=-12 compared with -54 when the 1850MeV resonance is fitted independently. Fitting the data with two separate resonances gives a far superior log likelihood compared with that from a single resonance with a Flatté formula. Both the $\eta_2(1650)$ and $X(1850)$ interfere strongly with other channels. The pattern of interference is quite different for the two resonances suggesting that they are independent signals.

The assignment of this state to the 2^{-+} nonet is difficult. A possibility is the η_2'; a predicted state analogous to the $\eta'(958)$ of the pseudoscalar nonet. However, it is expected that the η_2' should have a dominant decay mode into $K\bar{K}\pi$. The decay to $\eta f_2(1270)$ is tentative evidence for a glueball since gluons are believed to couple preferentially to η and η'. It is interesting that MARK III data on $J/\psi \rightarrow \gamma(\eta\pi\pi)$ shows a clear peak at 1850MeV in $\eta\pi\pi$, Figure 5.8(a). No spin-parity analysis of these data has been published.

There is some other evidence for $X(1850)$. The Crystal Ball $\gamma\gamma \rightarrow \pi^0\pi^0\eta$ data[43] shows a signal near 1900MeV, Figure 5.8(b). They claimed a 2^{-+} state with a large (70%) decay into $a_2(1320)\pi^0$ and 30% decay into $a_0(980)\pi$. Adding an $a_2(1320)\pi^0$ decay mode for the 2^{-+} $X(1850)$ to the optimum fit gave no significant improvement. Data from the VES Spectrometer at Serpukhov have shown a signal[44] at 1815MeV in $\pi^-\eta\eta$ with spins 1^{++} and 2^{-+} favoured. This cannot be the same state as the $X(1850)$ found here, due to isospin.

5.7 Mass and Width Errors

The systematic errors in the measured masses and widths of the resonances were estimated from the range of fitted values as the ingredients in the fit were varied.

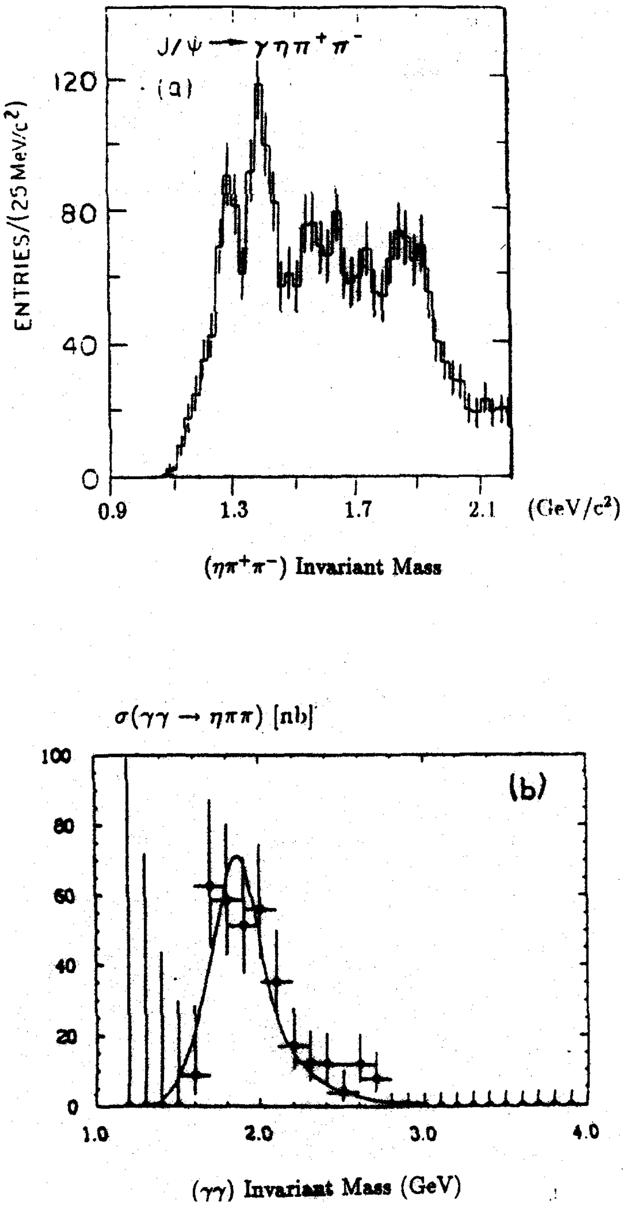

Figure 5.8: (a) MARK III $J/\psi \rightarrow \gamma\eta\pi^+\pi^-$ data. The $(\eta\pi^+\pi^-)$ invariant mass distribution shows a peak at 1850MeV. (b) Crystal Ball $\gamma\gamma \rightarrow \eta\pi^0\pi^0$ data. The cross section peaks in the $(\gamma\gamma)$ invariant mass region just below 1900MeV.

The statistical errors are considered to be negligible compared to the systematic errors. The estimated errors cover the full range of variation observed with different ingredients in the fit. Table 5.3 summarizes the errors on resonance mass and width.

Resonance	Mass (M)	Δ M	Width (Γ)	Δ Γ
$\eta_2(1650)$	1650	± 15	180	± 75
$X(1850)$	1850	± 30	225	± 50
$X(2135)$	2135	± 50	250	± 50

Table 5.3: Resonance Mass and Widths including the estimated errors.

5.8 Summary

The optimum fit to the $\bar{p}p \rightarrow \pi^0\pi^0\pi^0\eta$ at 1.94GeV/c required the following channels:-

$\bar{p}p \rightarrow \mathrm{f}_2(1270).a_0(980) \rightarrow (\pi^0\pi^0)(\pi^0\eta)$ Channel 1

$\bar{p}p \rightarrow \sigma.a_2(1320) \rightarrow (\pi^0\pi^0)(\pi^0\eta)$ Channel 2

$\bar{p}p \rightarrow \pi^0 f_1(1285) \rightarrow \pi^0[\pi^0 a_0(980)] \rightarrow \pi^0\pi^0(\pi^0\eta)$ Channel 3

$\bar{p}p \rightarrow \sigma.a_0(980) \rightarrow (\pi^0\pi^0)(\pi^0\eta)$ Channel 4

$\bar{p}p \rightarrow \pi^0\eta_2 \rightarrow \pi^0[\pi^0 a_2(1320)] \rightarrow \pi^0\pi^0(\pi^0\eta)$ Channel 5

$\bar{p}p \rightarrow \eta\pi_2(1670) \rightarrow \eta[\pi^0 f_2(1270)] \rightarrow \eta\pi^0(\pi^0\pi^0)$ Channel 6

$\bar{p}p \rightarrow \pi^0 X(2135) \rightarrow \pi^0[\pi^0 a_2(1320)]$ and $\pi^0[\eta f_2(1270)]$ Channel 7 & 8

$\bar{p}p \rightarrow \pi^0 X(1850) \rightarrow \pi^0[\eta f_2(1270)] \rightarrow \pi^0\eta(\pi^0\pi^0)$ Channel 9

An indication of the significance of the contribution from a channel is given by the change in log likelihood when the channel is removed from the optimum fit. This change can be considered as a lower limit since channels with similar kinematics are able to compensate to some extent when the fit is re-optimized. An example of this effect can be seen with the $\eta\pi_2(1670)$ and $\pi^0 X(2135)$ channels. Table 5.4 presents the effect of dropping individual channels. Without the $\eta\pi_2(1670)$ channel, the $\pi^0 X(2135)$ makes a highly significant contribution to the fit since the $\eta\pi_2(1670)$ is not there to compensate. The $\eta\pi_2(1670)$ channel is not easily seen by eye in the data (See bottom of Figure 5.13) and causes ambiguity in the fit, but it is retained since it is an established resonance and provides a significant improvement to the log likelihood. Without the $\eta\pi_2(1670)$ channel, the $\pi^0\eta_2(1650)$ and $a_0(980)f_2(1270)$ channels become slightly less significant. This can be attributed to the removal of the interference with the $\eta\pi_2(1670)$.

Drop Channel	With $\eta\pi_2(1670)$	Without $\eta\pi_2(1670)$
$\eta\pi_2(1670)$	$\Delta s = +88.0$	
$\pi^0\eta_2(1650)$	$\Delta s = +67.6$	$\Delta s = +50.2$
$\pi^0 X(1850)$	$\Delta s = +53.8$	$\Delta s = +103.4$
$\pi^0 X(2135)$	$\Delta s = +37.6$	$\Delta s = +101.2$
$a_0(980)f_2(1270)$	$\Delta s = +29.2$	$\Delta s = +20.7$
$a_2(1320)\sigma$	$\Delta s = +16.3$	$\Delta s = +18.7$
$a_0(980)\sigma$	$\Delta s = +12.8$	$\Delta s = +18.2$
$\pi^0 f_1(1285)$	$\Delta s = +41.5$	$\Delta s = +42.4$
Background	$\Delta s = +69.2$	$\Delta s = +91.3$

Table 5.4: The effect of dropping individual components from the optimum fit, with and without the inclusion of the $\eta\pi_2(1670)$ channel.

Interference plays an important part in the data with the prominent channels 1 and 2 acting as interferometers. Phase information from the interference makes the fit sensitive to the resonance masses thus helping to establish the masses of resonances with broad widths. Interferences improving the log likelihood by more than Δs=-10 were retained in the fit:-

$$a_0(980)f_2(1270) \otimes \pi^0 X(1850) : \Delta s = \text{-21.2}$$

$$a_2(1320)\sigma \otimes \pi^0\eta_2(1650) : \Delta s = \text{-30.1}$$

$$\pi^0\eta_2(1650) \otimes \pi^0 X(1850) : \Delta s = \text{-20.1}$$

$$a_0(980)f_2(1270) \otimes \eta\pi_2(1670) : \Delta s = \text{-25.3}$$

$$\pi^0\eta_2(1650) \otimes \eta\pi_2(1670) : \Delta s = \text{-10.4}$$

$$\pi^0 X(1850) \otimes \eta\pi_2(1670) : \Delta s = \text{-34.2}$$

The comparison of the real data with the invariant mass projections from the optimum fit provides a good illustration of the overall quality of the fit. These mass projections can be found in Figures 5.9 and 5.10. Figure 5.11 shows the full scatter plot generated by the optimum fit. Resonances with narrow widths in the fit projections are slightly too broad. This may be because the phase space component is not a perfect description of the background.

More specific regions of the data, such as the data with $\pi^0\eta$ combinations in the $a_2(1320)$ mass region have been selected to illustrate a more detailed comparison of the real data with the optimum fit. Figure 5.12 shows the $(\pi^0\pi^0\eta)$ mass distribution for events with a $(\pi^0\eta)$ mass combination in the $a_2(1320)$ mass region ([1318.2$\pm$75]MeV) and a cut against the $f_0(975)$ and $f_2(1270)$. Enhancements around 1650MeV and 2135MeV show clear $\eta_2(1650)$ and $X(2135)$ signals. The latter is small since it's second decay mode via $\pi^0 f_2(1270)$ has been removed.

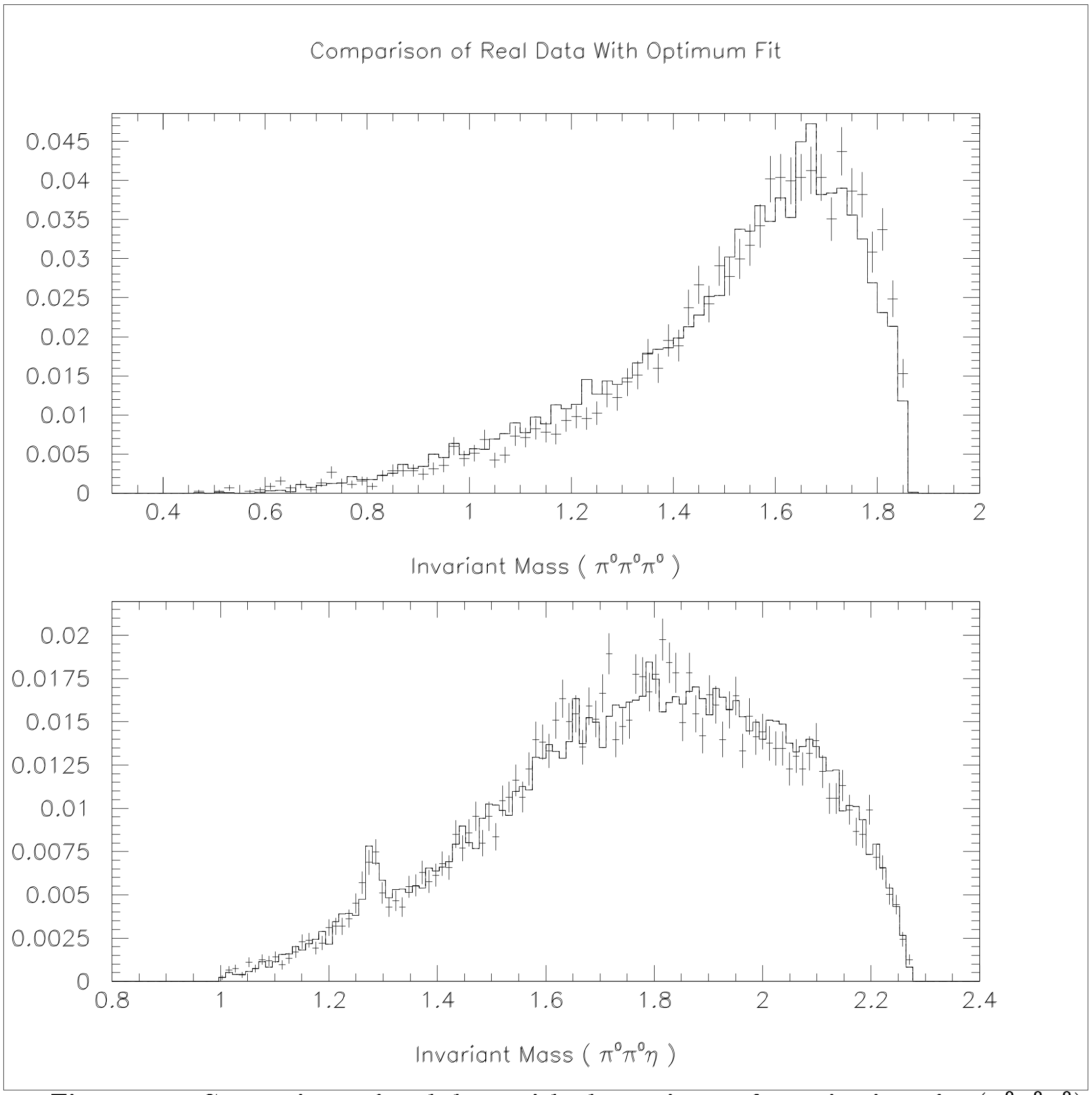

Figure 5.9: Comparison of real data with the optimum fit projections for $(\pi^0\pi^0\pi^0)$ and $(\pi^0\pi^0\eta)$. The real data is represented by the error bars.

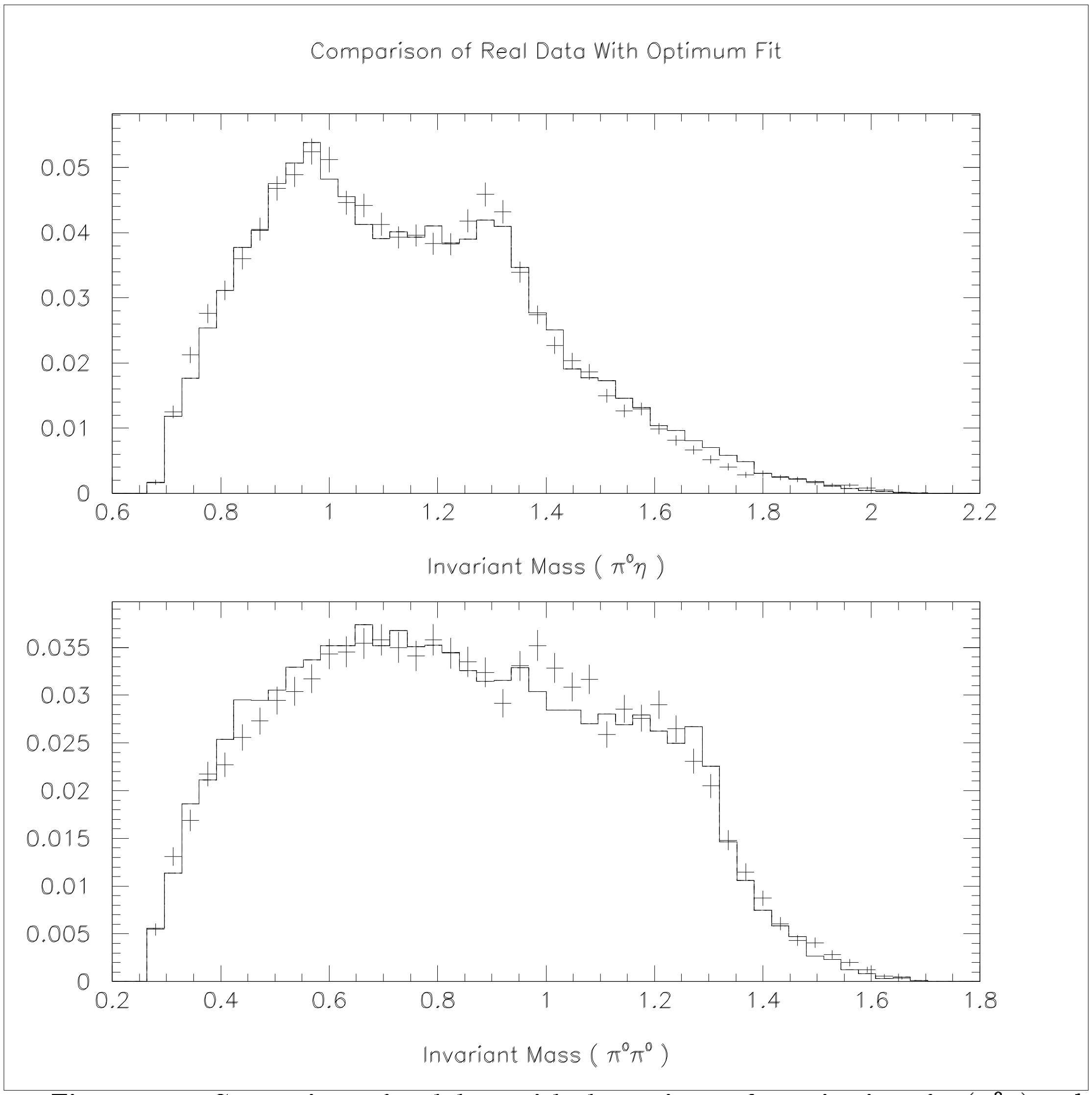

Figure 5.10: Comparison of real data with the optimum fit projections for $(\pi^0\eta)$ and $(\pi^0\pi^0)$. The real data is represented by the error bars. A small discrepancy can be seen in the $f_0(975)$ mass region.

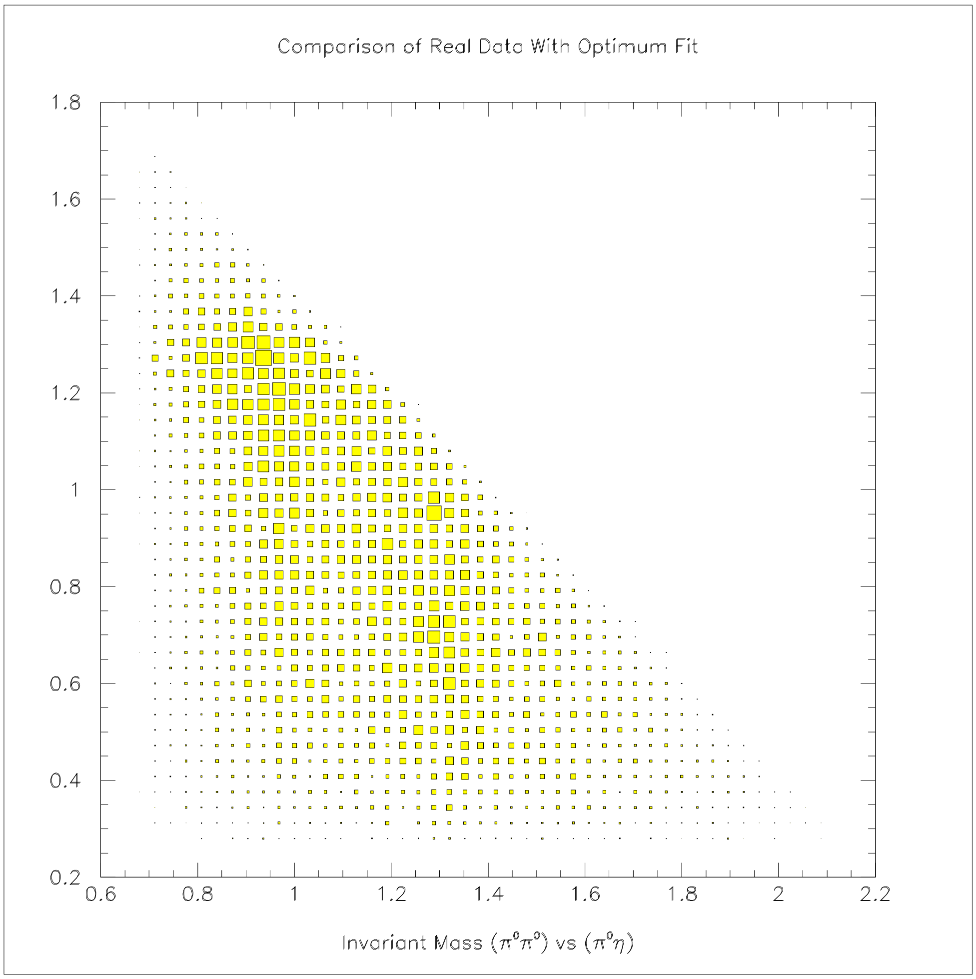

Figure 5.11: Full scatter plot of $(\pi^0\pi^0)$ versus $(\pi^0\eta)$ [all combinations plotted] generated using the optimum fit parameters. This compares well with the real data scatter plot in Figure 4.18

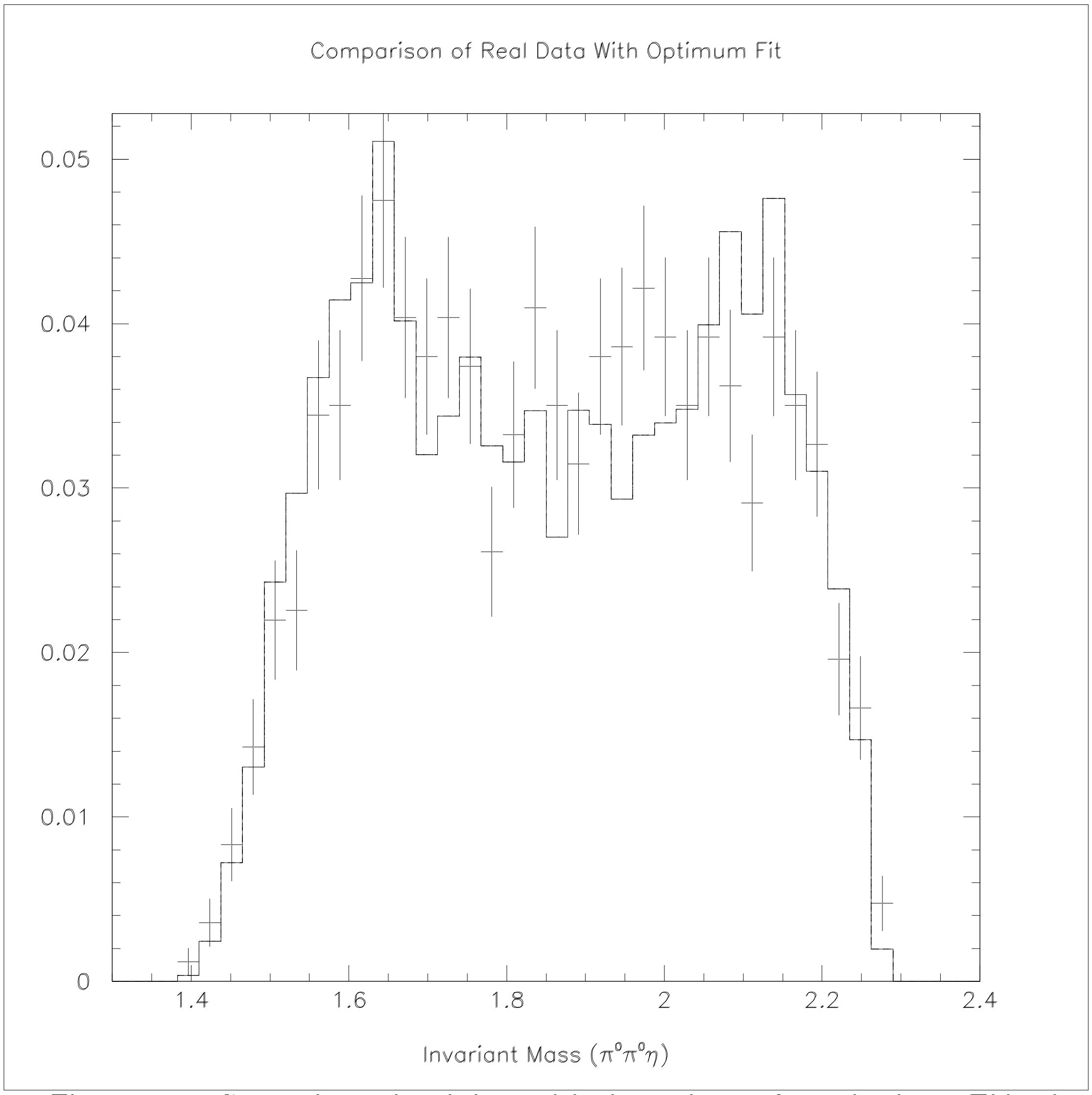

Figure 5.12: Comparison of real data with the optimum fit projections. This plot shows the ($\pi^0\pi^0\eta$) mass with a ($\pi^0\eta$) combination in the $a_2(1320)$ mass region and the ($\pi^0\pi^0$) mass not in the region (925-1325)MeV to avoid the $f_0(975)$ and $f_2(1270)$. Error bars represent the real data.

Selecting events with $(\pi^0\pi^0)$ combinations in the $f_2(1270)$ mass region (1100-1400MeV) and cutting out those events which have a $(\pi^0\eta)$ combination in the $a_2(1320)$ mass region shows peaks due to the $X(1850)$ and $X(2135)$ in the resulting $(\pi^0\pi^0\eta)$ mass distribution, Figure 5.13. Also shown is the $(\pi^0\pi^0\pi^0)$ mass distribution. It is puzzling that there is no apparent signal from $\pi_2(1670) \rightarrow \pi^0 f_2(1270)$.

To check that a channel including the $a_0(980)$ had not been missed, events with a $(\pi^0\eta)$ combination in the mass region of the $a_0(980)$ ([982.7$\pm$70]MeV) were selected and the corresponding $(\pi^0\pi^0\eta)$ mass distribution plotted. Note that $(\pi^0\pi^0)$ combinations in the $f_2(1270)$ mass region were not used so as to eliminate the strong $a_0(980)f_2(1270)$ signal, channel 1. This $a_0(980)\pi^0$ mass distribution can be seen in Figure 5.14. There is no evidence for further resonances, in particular for the decays of $\eta_2(1650)$ or $X(1850)$ to $a_0(980)\pi^0$. Also presented is a $(\pi^0\pi^0\eta)$ mass distribution from events with a $(\pi^0\pi^0)$ mass in the region of the $f_0(975)$ ([974.1$\pm$50]MeV). This shows a slight systematic enhancement in the real data from 1575 to 1700MeV. On investigation, it is found that this discrepancy can be removed by adding a 0^- state (decaying into $f_0(975)\eta$) with a mass between (1625-1650)MeV. The addition improves the log likelihood by a barely significant amount, Δs=-21, and is ambiguous with a spin of 1^{++} which gives Δs=-15. Higher statistics would be needed to resolve whether a further resonance is required, and if so, it's spin-parity assignment. It is certainly not an additional decay mode of $\eta_2(1650)$. The L=2 centrifugal barrier is strong and consequently this hypothesis gives only Δs=-4.

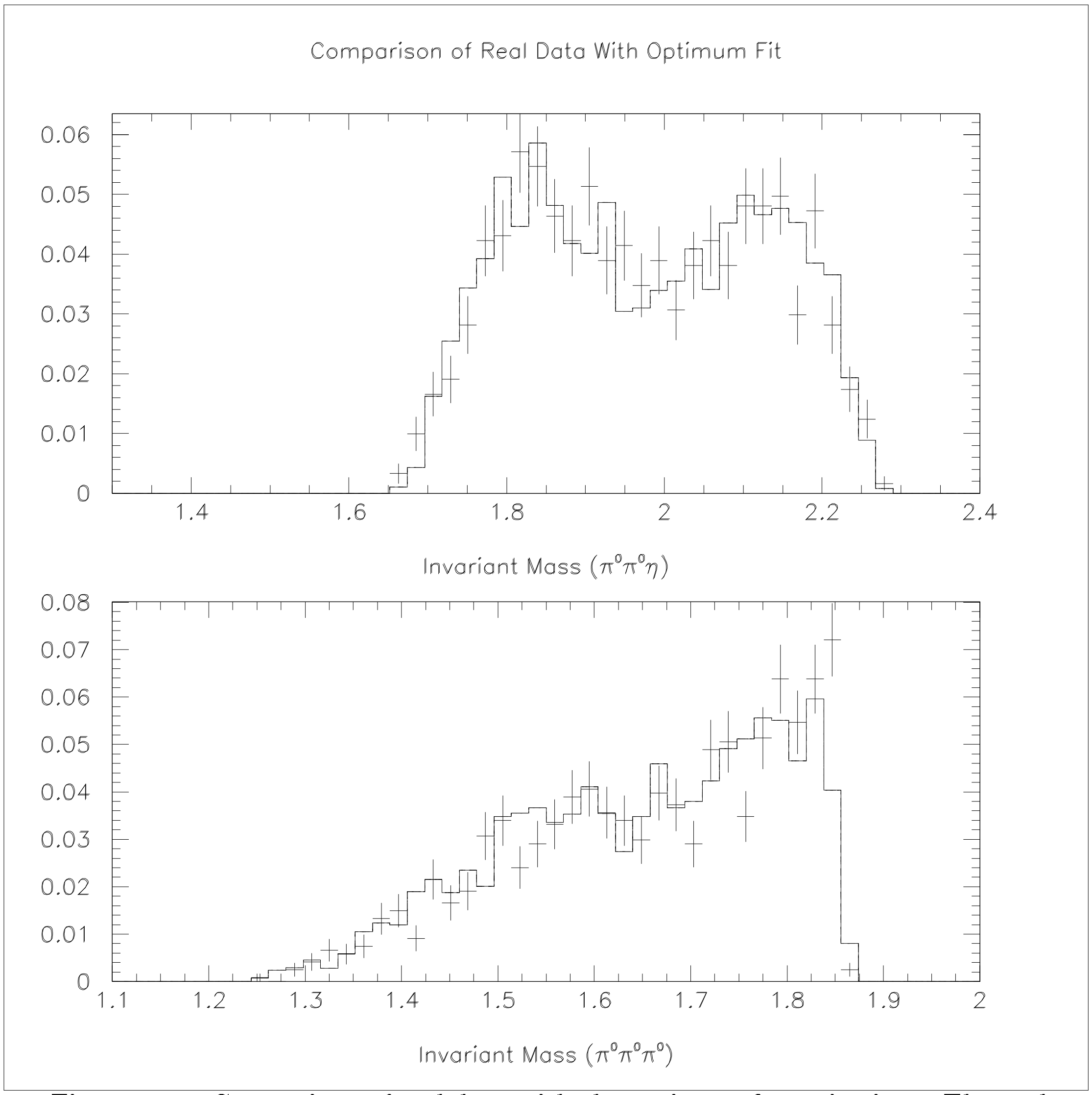

Figure 5.13: Comparison of real data with the optimum fit projections. These plots have the $(\pi^0\pi^0)$ combination in the $f_2(1270)$ mass region and the $(\pi^0\eta)$ masses are not in the $a_2(1320)$ mass region. Error bars represent the real data.

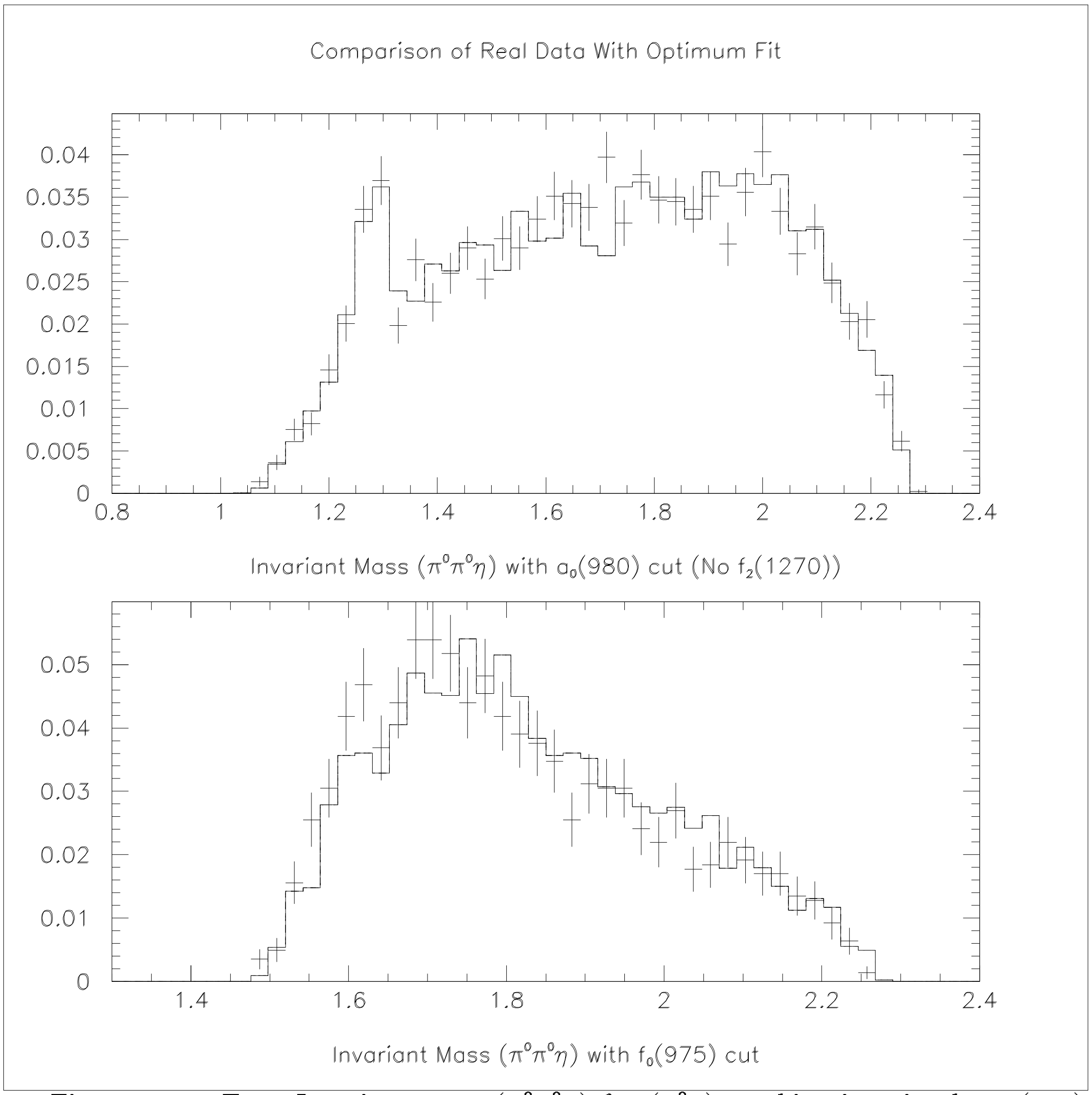

Figure 5.14: Top: Invariant mass $(\pi^0\pi^0\eta)$ for $(\pi^0\eta)$ combinations in the $a_0(980)$ mass region and the $(\pi^0\pi^0)$ not in the $f_2(1270)$ mass region. Bottom: Invariant mass $(\pi^0\pi^0\eta)$ for events with $(\pi^0\pi^0)$ in the $f_0(975)$ mass region.

Chapter 6

Concluding Comments

The aim of this analysis was to observe new J^P=2^- states and therefore contribute to the search for the missing 2^- glueball candidate. This search for 2^- states uses $\bar{p}p \rightarrow \pi\pi\pi\eta$ Crystal Barrel data:

- $\bar{p}p \rightarrow \pi^+\pi^-\pi^0\eta$ at 1.20 GeV/c
- $\bar{p}p \rightarrow \pi^+\pi^-\pi^0\eta$ at 1.94 GeV/c
- $\bar{p}p \rightarrow \pi^0\pi^0\pi^0\eta$ at 1.20 GeV/c
- $\bar{p}p \rightarrow \pi^0\pi^0\pi^0\eta$ at 1.94 GeV/c.

The data have good mass resolution and are a rich source of resonances through a variety of decay channels. The use of invariant mass distributions and the comparison of real and Monte Carlo data provides a crude but effective method of searching for initial indications of new resonances. Discrepancies in the mass distributions have provoked a more thorough analysis to establish quantum numbers of the resonances.

Both charged channel data sets contain a discrepancy in the comparison of the real and Monte Carlo data for the $\pi^+\pi^-\eta$ and $\pi^\pm\pi^0\eta$ invariant mass distributions. The discrepancy occurs for *all* distributions in the (1600-1800)MeV $\pi\pi\eta$ mass region. A second common feature of the charged channel data sets is the charged and neutral

ρ signal. Scatter plots of $(\pi\pi)$ versus $(\pi\eta)$ show enhancements due to $a_0(980)\rho$ and $a_2(1320)\rho$ signals above a large ρ band. A state decaying into $\eta\rho$ with zero orbital angular momentum between the η and ρ would have 2^{--} quantum numbers and produce a ρ band in a $(\pi\pi)$ versus $(\pi\eta)$ scatter plot. Therefore assuming that the enhancement in the (1600-1800)MeV $\pi\pi\eta$ mass region is due to $\eta\rho$, the $\pi^+\pi^-\pi^0\eta$ data shows great promise in the search for new 2^- states.

The $\pi^0\pi^0\pi^0\eta$ data also exhibits an interesting $\pi^0\pi^0\eta$ enhancement in the 1.94GeV/c data. This data set was chosen, in preference to the charged data, for spin analysis due to the limited number of isospin states. The maximum likelihood method was used to fit the $\pi^0\pi^0\pi^0\eta$ 1.94GeV/c data and the following channels were observed:

1. $\bar{p}p \rightarrow \mathrm{f}_2(1270).a_0(980) \rightarrow (\pi^0\pi^0)(\pi^0\eta)$
2. $\bar{p}p \rightarrow \sigma.a_2(1320) \rightarrow (\pi^0\pi^0)(\pi^0\eta)$
3. $\bar{p}p \rightarrow \pi^0 f_1(1285) \rightarrow \pi^0[\pi^0 a_0(980)] \rightarrow \pi^0\pi^0(\pi^0\eta)$
4. $\bar{p}p \rightarrow \sigma.a_0(980) \rightarrow (\pi^0\pi^0)(\pi^0\eta)$
5. $\bar{p}p \rightarrow \eta\pi_2(1670) \rightarrow \eta[\pi^0 f_2(1270)] \rightarrow \eta\pi^0(\pi^0\pi^0)$.

In addition to these channels it is necessary to include several more channels involving new or poorly established resonances. These resonances are discussed in the following sections.

6.1 $\eta_2(1650)$

The $\pi_2(1670)$ (J^{PC}=2^{-+}) has a predicted isospin I=0 partner, the η_2. A natural candidate for this resonance has been observed with (1650±15) MeV mass and (180±75) MeV width. It is observed in the following decay channel:

- $\bar{p}p \rightarrow \pi^0\eta_2 \rightarrow \pi^0[\pi^0 a_2(1320)] \rightarrow \pi^0\pi^0(\pi^0\eta)$.

and contributes to the enhancement in the $\pi^0\pi^0\eta$ mass distribution. No additional decay modes have been observed and the quantum numbers are measured, without ambiguity, to be 2^{-+}. This channel interferes with channels 2, 5 and a second channel involving a new resonance with 1850 MeV mass and $J^{PC}=2^{-+}$.

6.2 $X(1850)$

The second new $J^{PC}=2^{-+}$ is observed to be produced at threshold in the channel:

- $\bar{p}p \to \pi^0 X(1850) \to \pi^0[\eta f_2(1270)] \to \pi^0\eta(\pi^0\pi^0)$.

The mass of the resonance is (1850±30) MeV and the width (225±75) MeV. Again, the $J^{PC}=2^{-+}$ quantum numbers are unambiguous and the $\pi^0[\eta f_2(1270)]$ decay is the only decay mode observed. The $\pi^0 X(1850)$ channel interferes with channels 1, 5 and $\pi^0\eta_2(1650)$.

The assignment of this state as the ninth member of the pseudotensor nonet is difficult. A possibility is that the $X(1850)$ is the same state as that observed in the MARK III data, Figure 5.8. The MARK III $J/\psi \to \gamma\pi^+\pi^-\eta$[45] data shows an enhancement in the $\pi^+\pi^-\eta$ mass distribution in the 1850MeV mass region. If these two states were the same then the $X(1850)$ must be a strong candidate for a 2^{-+} glueball.

6.3 $X(2135)$

A third channel required by the fit is:

- $\bar{p}p \to \pi^0 X(2135) \to \pi^0[\pi^0 a_2(1320)]$ and $\pi^0[\eta f_2(1270)]$.

The state, $X(2135)$, has a (2135±50) MeV mass and (250±50) MeV width with $J^{PC}=2^{++}$. Although many different spin states are predicted in this mass region,

2^{++} quantum numbers gave the only significant contribution. The most likely assignment of this state to a previously observed resonance is the $f_2(2175)$ observed by GAMS. By changing the optimum mass and width to those claimed by GAMS, the fit deteriorates by an insignificant amount.

6.4 Interference and the $\pi_2(1670)$

The effects of interference between channels has proven to enhance the sensitivity in measuring resonance masses. Although the prominent channels 1 and 2 appear to dominate the data and swamp the weaker channels, they are not a hindrance; they are important as interferometers. Phase variation due to interference helps to sharpen mass resolution and distinguish separate resonances with large widths and similar masses.

A complication in the fitting of the data is caused by the presence of the $\pi_2(1670)$. It's appearance in the data is not completely convincing. Evidence suggesting it's presence arises in the enhancement around 1670MeV of the $(\pi^0\pi^0\pi^0)$ mass distribution and large improvement to the fit when the $\eta\pi_2(1670)$ channel is included in the fit. Evidence suggesting a negligible contribution is seen in the $(\pi^0\pi^0)$ versus $(\pi^0\eta)$ scatter plot. The $\pi_2(1670)$ has a predominant decay mode into $f_2(1270)\pi^0$ and therefore the $f_2(1270)$ should appear as a band. Despite the $f_2(1270)a_0(980)$ region of enhancement, no clear $f_2(1270)$ band is seen. Having selected events with a $(\pi^0\pi^0)$ mass combination in the $f_2(1270)$ mass region, the corresponding $(\pi^0\pi^0\pi^0)$ mass distribution does not show any enhancement in the 1670MeV mass region.

Due to the evidence suggesting the presence of the $\pi_2(1670)$ and the fact that it is an established meson, the $\eta\pi_2(1670)$ channel is retained in the fit. The $\eta\pi_2(1670)$ channel has no effect on the observation of the $\eta_2(1650)$, $X(1850)$ and $X(2135)$ signal observations. The $\eta\pi_2(1670)$, $\pi^0X(1850)$ and $\pi^0X(2135)$ channels are able to mimic each other to some extent. This effect is seen when individual components are removed from the fit. Without the presence of the $\pi_2(1670)$, the significance of the $X(1850)$ and $X(2135)$ signals is increased dramatically. However, even with the $\pi_2(1670)$, both the $X(1850)$ and $X(2135)$ provide highly significant contributions to the fit.

6.5 $TS(1635)$

A tentative signal, $TS(1635)$ is observed in the channel:

- $\bar{p}p \rightarrow \pi^0 TS(1635) \rightarrow \pi^0[\eta f_0(975)] \rightarrow \pi^0\eta(\pi^0\pi^0)$.

The mass is measured to be in the range (1625-1650) MeV. The quantum numbers giving the best fit are 0^{-+}, however, 1^{++} provides an improvement to the log likelihood which is almost as good. More statistics are necessary to resolve this ambiguity. A 0^{-+} with a mass in the region of 1635 MeV is most likely to be a radial excitation.

6.6 Future Work

The restriction in time only allowed a spin analysis of the $\bar{p}p \rightarrow \pi^0\pi^0\pi^0\eta$ at 1.94GeV/c data set. However, the results of this analysis prompts an analysis of the $\bar{p}p \rightarrow \pi^0\pi^0\pi^0\eta$ at 1.20GeV/c data in order to consolidate the observations of the $\eta_2(1650)$ and $X(1850)$ signals. It is expected that the spin analysis of the $\bar{p}p \rightarrow \pi^0\pi^0\pi^0\eta$ at 1.20GeV/c data should be relatively simple since the $\pi_2(1670)$ and high mass states decaying into $\pi^0\pi^0\eta$ are excluded due to the limits of phase space. Having completed a spin analysis of the $\pi^0\pi^0\pi^0\eta$ data, a search for 2^- states with isospin I=1 in the corresponding $\pi^+\pi^-\pi^0\eta$ data is made easier. The nature of the $X(1850)$ state must be verified by a spin analysis of the similar resonance observed in the MARK III data.

Appendix A

Scaling Factors, Confidence Levels and Pulls

This appendix presents the scaling factors, confidence level distributions and pulls from the kinematic fits.

A.1 Scaling Factors.

Tables A.2 and A.1 show the scaling factors used in the analysis of the 2-prong and 0-prong data. The scaling factors for the Monte Carlo (MC) data were obtained using the $\pi^+\pi^-\pi^0\eta$ and $\pi^0\pi^0\pi^0\eta$ events. Scaling factors were applied to error magnitudes for parameters used in kinematic fits. For charged particles these include the angle (ψ) between the tangent at the point of a track's closest approach to the origin and a line parallel to the x-axis, the dip angle of the helix in the r-z plane, (λ), and the radius of curvature, (α). The scaled photon errors used in kinematic fits were $\Delta\phi$, $\Delta\theta$ and $\Delta\text{Energy}_\gamma$. The reconstruction of charged particles from both real and MC data shows that the transverse momentum ($\mathbf{p}_{xy}$) of positive and negative particles needs separate scaling factors. Also, despite the crystal calibration, it was necessary to scale the photon energies.

Scaling Factor	December 0-Prong	July 0-Prong	Monte Carlo at 1.20GeV/c	Monte Carlo at 1.94GeV/c
γ SF($\Delta\phi$)	0.7700	0.7900	1.060	1.050
γ SF($\Delta\theta$)	0.3300	0.3500	0.500	0.450
γ SF(ΔE)	1.4500	1.4000	1.400	1.450
γ SF(E)	1.0180	1.0124	1.000	1.000

Table A.1: Scaling Factors for 0-Prong Data.

Scaling Factor	December 2-Prong	July 2-Prong	Monte Carlo at 1.20GeV/c	Monte Carlo at 1.94GeV/c
$\pi^\pm$ SF($\Delta\psi$)	1.0500	0.900	0.450	0.4000
$\pi^\pm$ SF($\Delta\lambda$)	1.8400	1.730	1.020	1.0200
$\pi^\pm$ SF($\Delta\alpha$)	2.7800	1.900	1.000	0.9500
π^+ SF($\mathbf{p}_{xy}$)	1.0478	1.044	1.025	1.0310
π^- SF($\mathbf{p}_{xy}$)	1.0768	1.065	1.003	1.0005
γ SF($\Delta\phi$)	1.2000	1.100	1.020	1.0200
γ SF($\Delta\theta$)	1.4000	1.400	1.040	1.0400
γ SF(ΔE)	1.6000	1.400	1.200	1.2000
γ SF(E)	1.0120	1.012	1.002	1.0020

Table A.2: Scaling Factors for 2-Prong Data.

A.2 Confidence Level Distributions and Pulls.

In this section the confidence level (CL) distributions and the corresponding pull information are presented. For the 2-prong data sets, the CL distribution and hadronic split-off multiplicity provided by CBDROP are also shown.

A.2.1 December 1991 2-Prong Data

Figure A.1 shows the CL distribution from the energy-momentum fit (required in the identification of hadronic split-offs) and the corresponding hadronic split-off multiplicity distribution. The CL distribution is flat for CL $>$ 20% implying that overall, the errors are the correct size. The hadronic split-off multiplicity distribution is similar to that of at-rest data. Figure A.2 presents the CL distributions for fits to energy-momentum, $\pi^+\pi^-\pi^0\gamma\gamma$ and $\pi^+\pi^-\pi^0\eta$. The pull information suggests that the photon energies have been underestimated. This is an effect caused by the large number of events in which one or more photons were lost along the beam line thus biasing the total energy of the events.

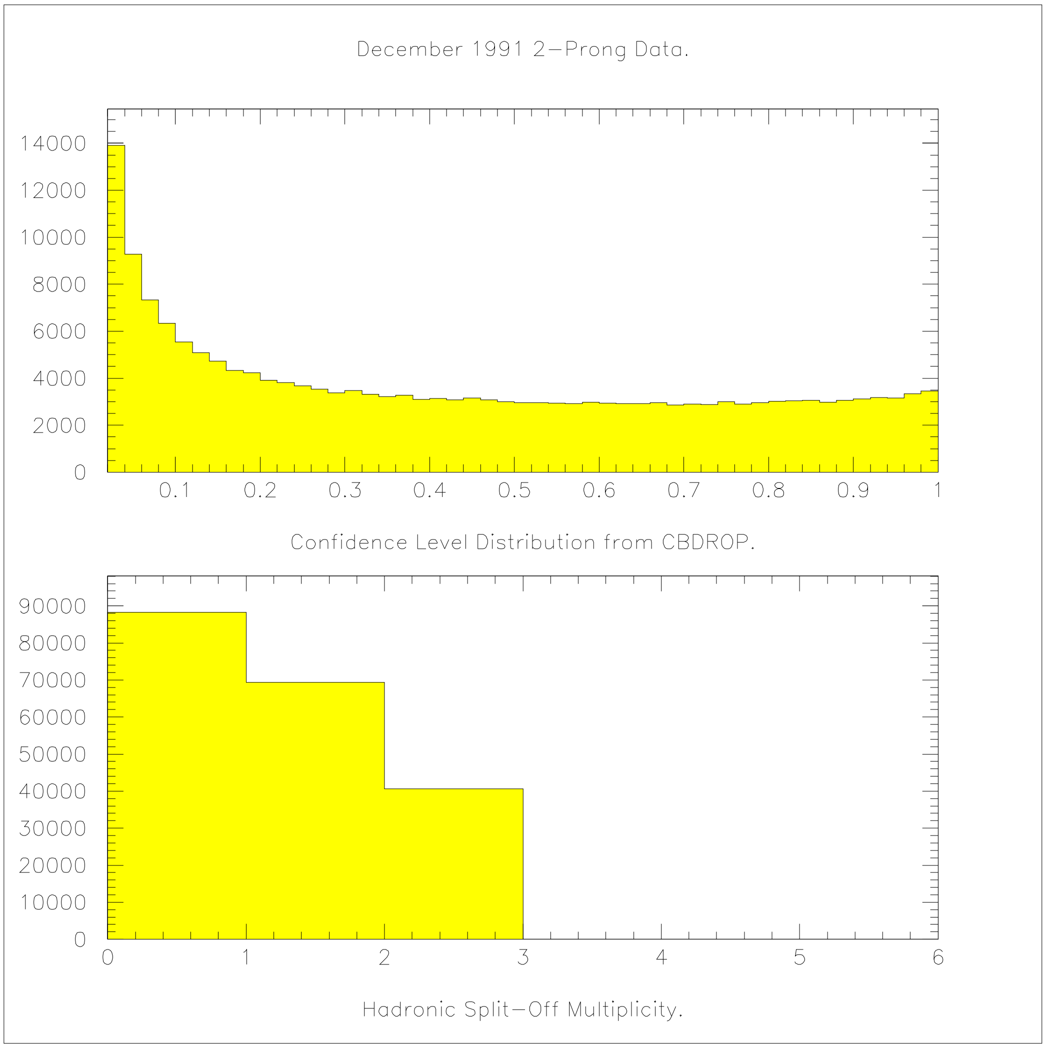

Figure A.1: Confidence level distribution and hadronic split-off multiplicity from CBDROP for the December 1991 2-prong data. The split-off multiplicity distribution is very similar to the distribution from at-rest data.

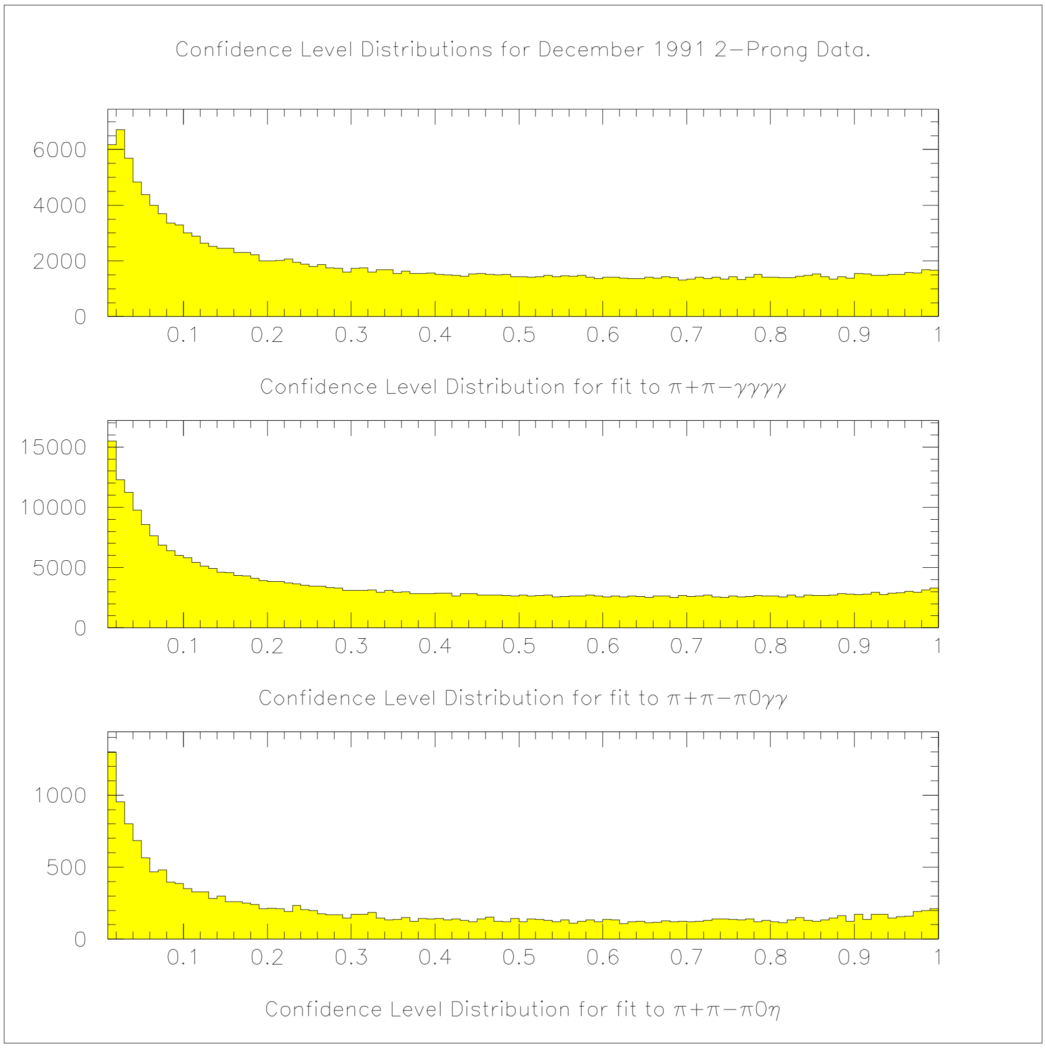

Figure A.2: CBKFIT: Confidence Level Distributions from the kinematic fitting of the December 1991 2-Prong Data.

Kinematic Fit to Ideal Energy-Momentum at 1.20GeV/c					
Fit Parameter		Real Data		MC Data	
		Mean	Sigma	Mean	Sigma
π^+	ψ	0.033 ± 0.003	1.104 ± 0.002	0.013 ± 0.005	0.987 ± 0.004
	$\tan(\lambda)$	0.003 ± 0.002	1.018 ± 0.002	0.040 ± 0.005	1.024 ± 0.003
	$1/P_{xy}$	-0.050 ± 0.003	1.081 ± 0.001	0.026 ± 0.005	1.030 ± 0.004
π^-	ψ	-0.039 ± 0.003	1.105 ± 0.002	0.057 ± 0.004	0.959 ± 0.004
	$\tan(\lambda)$	0.005 ± 0.002	1.023 ± 0.002	0.006 ± 0.005	1.009 ± 0.003
	$1/P_{xy}$	-0.011 ± 0.003	1.049 ± 0.001	0.017 ± 0.004	0.984 ± 0.004
γ	ϕ	0.000 ± 0.001	1.019 ± 0.001	-0.008 ± 0.002	1.008 ± 0.002
	θ	-0.136 ± 0.001	1.062 ± 0.001	-0.072 ± 0.002	1.059 ± 0.002
	$\sqrt{E}$	0.192 ± 0.001	0.986 ± 0.001	0.167 ± 0.002	1.023 ± 0.002

Table A.3: Pulls for December 2-Prong Data.

Kinematic Fit to $\bar{p}p \rightarrow \pi^+\pi^-\pi^0\gamma\gamma$ at 1.20GeV/c					
Fit Parameter		Real Data		MC Data	
		Mean	Sigma	Mean	Sigma
π^+	ψ	0.019 ± 0.003	1.073 ± 0.001	0.026 ± 0.005	0.964 ± 0.004
	$\tan(\lambda)$	-0.005 ± 0.004	1.016 ± 0.002	0.028 ± 0.005	1.010 ± 0.003
	$1/P_{xy}$	-0.040 ± 0.003	1.127 ± 0.002	0.011 ± 0.005	1.011 ± 0.004
π^-	ψ	-0.035 ± 0.003	1.078 ± 0.002	0.044 ± 0.004	0.940 ± 0.004
	$\tan(\lambda)$	-0.008 ± 0.002	1.015 ± 0.002	0.002 ± 0.005	0.996 ± 0.003
	$1/P_{xy}$	-0.011 ± 0.003	1.046 ± 0.001	0.002 ± 0.005	0.963 ± 0.004
γ	ϕ	-0.001 ± 0.001	1.063 ± 0.001	-0.008 ± 0.003	1.063 ± 0.002
	θ	-0.089 ± 0.001	1.059 ± 0.001	-0.049 ± 0.003	1.099 ± 0.002
	$\sqrt{E}$	0.213 ± 0.001	1.102 ± 0.001	1.000 ± 0.002	1.048 ± 0.002

Table A.4: Pulls for December 2-Prong Data.

Kinematic Fit to $\bar{p}p \rightarrow \pi^+\pi^-\pi^0\eta$ at 1.20GeV/c					
Fit Parameter		Real Data		MC Data	
		Mean	Sigma	Mean	Sigma
π^+	ψ	-0.008 $\pm$ 0.007	1.090 $\pm$ 0.005	0.020 $\pm$ 0.005	0.937 $\pm$ 0.004
	$\tan(\lambda)$	-0.046 $\pm$ 0.007	1.005 $\pm$ 0.005	0.050 $\pm$ 0.005	1.004 $\pm$ 0.003
	$1/P_{xy}$	-0.018 $\pm$ 0.007	1.117 $\pm$ 0.005	0.045 $\pm$ 0.005	0.989 $\pm$ 0.004
π^-	ψ	-0.017 $\pm$ 0.007	1.065 $\pm$ 0.005	0.060 $\pm$ 0.004	0.911 $\pm$ 0.004
	$\tan(\lambda)$	-0.053 $\pm$ 0.007	1.000 $\pm$ 0.005	0.009 $\pm$ 0.005	0.998 $\pm$ 0.003
	$1/P_{xy}$	0.020 $\pm$ 0.007	1.084 $\pm$ 0.005	0.037 $\pm$ 0.005	0.935 $\pm$ 0.004
γ	ϕ	0.016 $\pm$ 0.004	1.213 $\pm$ 0.003	-0.007 $\pm$ 0.002	0.988 $\pm$ 0.002
	θ	-0.105 $\pm$ 0.004	1.188 $\pm$ 0.003	-0.057 $\pm$ 0.003	1.056 $\pm$ 0.002
	$\sqrt{\mathrm{E}}$	0.215 $\pm$ 0.004	1.251 $\pm$ 0.003	0.093 $\pm$ 0.003	1.015 $\pm$ 0.002

Table A.5: Pulls for December 2-Prong Data.

A.2.2 July 1992 2-Prong Data

Figure A.3 shows the CL distribution from the energy-momentum fit (required in the identification of hadronic split-offs) and the corresponding hadronic split-off multiplicity distribution. The CL distribution rises for CL $>$ 90% implying that overall, the errors are slightly too large. The hadronic split-off multiplicity distribution is similar to that of at-rest and 1.20GeV/c data. Figure A.4 presents the CL distributions for fits to energy-momentum, $\pi^+\pi^-\pi^0\gamma\gamma$ and $\pi^+\pi^-\pi^0\eta$. The pull information suggests that the photon energies have been underestimated. This is an effect caused by the large number of events in which one or more photons were lost along the beam line thus biasing the total energy of the events.

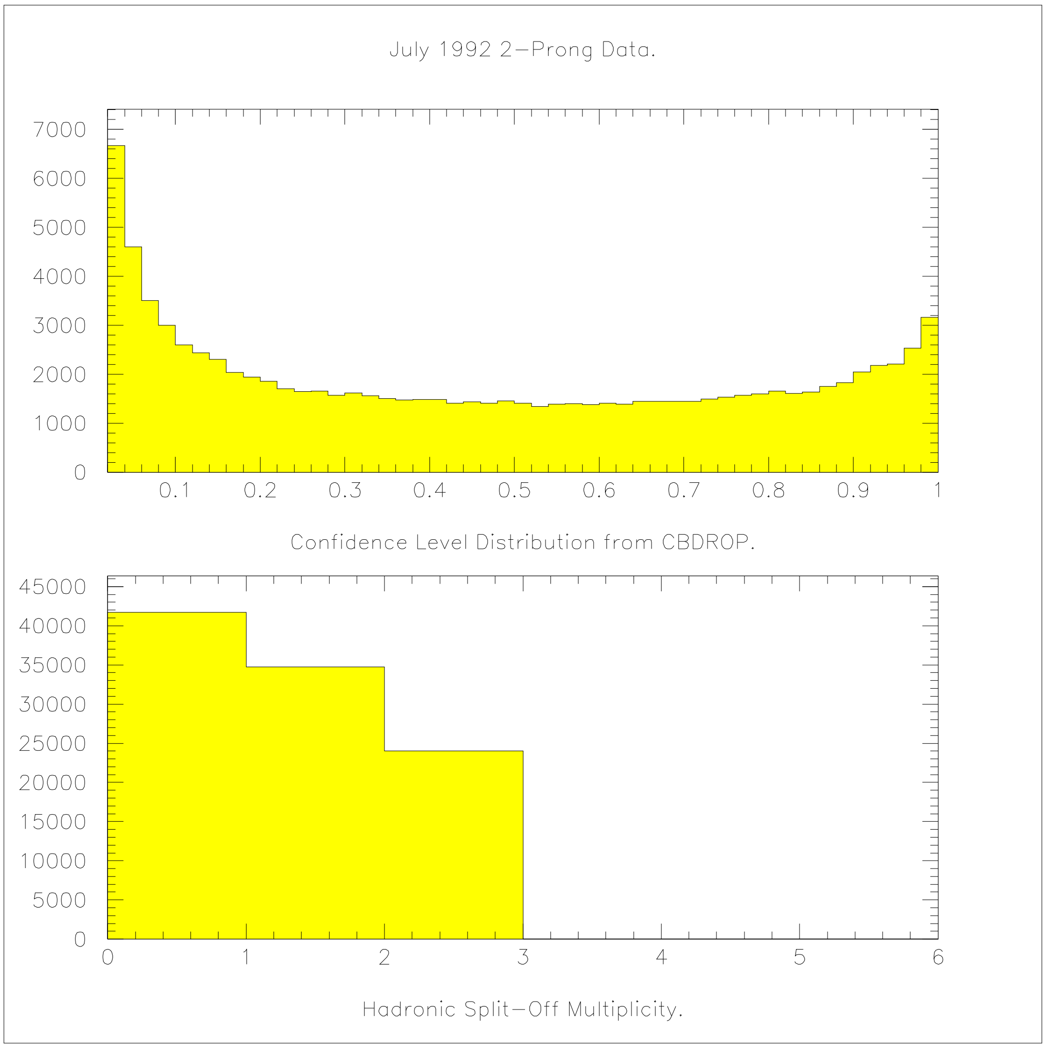

Figure A.3: Confidence level distribution and hadronic split-off multiplicity from CBDROP for the July 1992 2-prong data.

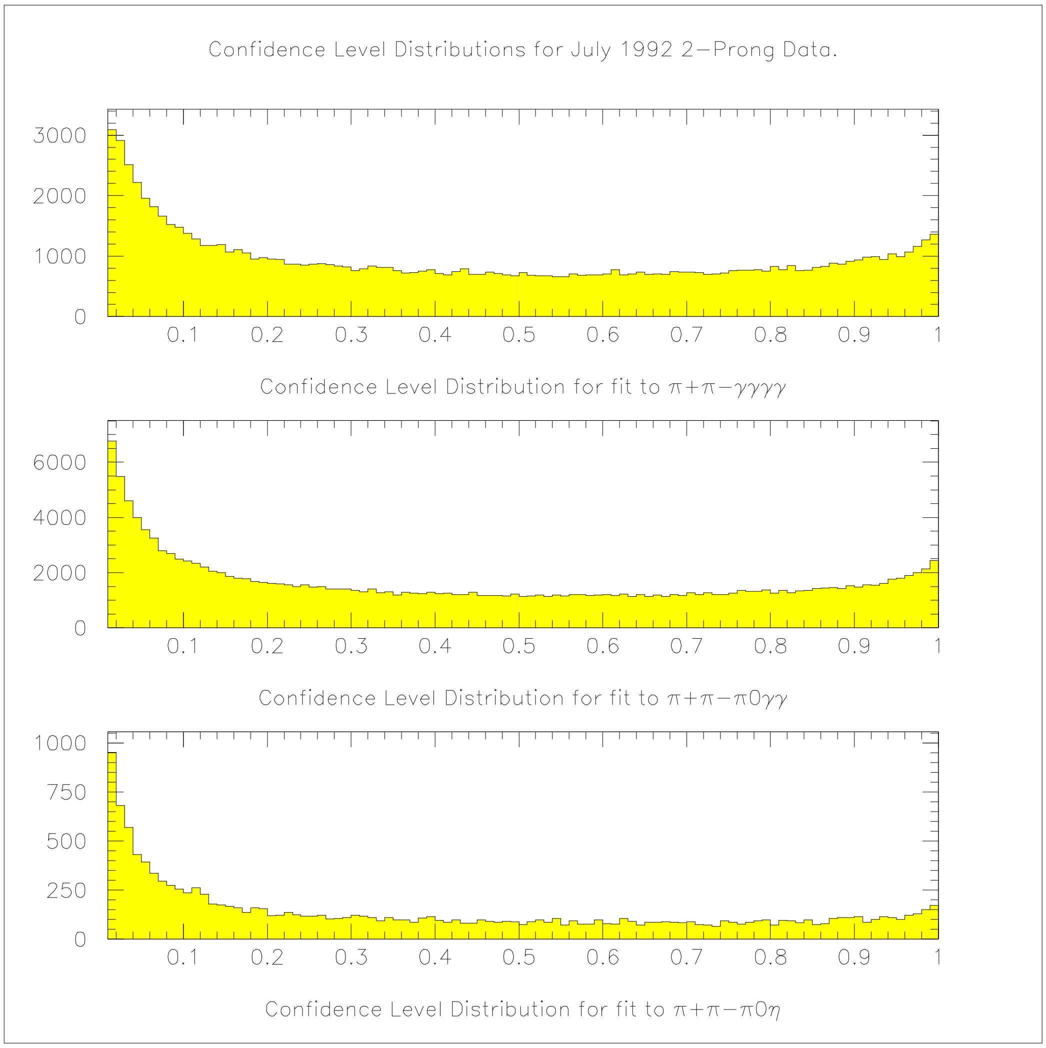

Figure A.4: CBKFIT: Confidence Level Distributions from the kinematic fitting of the July 1992 2-Prong Data.

Kinematic Fit to Ideal Energy-Momentum at 1.94GeV/c					
Fit Parameter		Real Data		MC Data	
		Mean	Sigma	Mean	Sigma
π^+	ψ	0.024 ± 0.003	1.019 ± 0.003	0.009 ± 0.007	0.976 ± 0.006
	$\tan(\lambda)$	0.101 ± 0.004	1.056 ± 0.003	0.083 ± 0.007	1.006 ± 0.005
	$1/P_{xy}$	-0.005 ± 0.003	1.030 ± 0.003	0.011 ± 0.007	1.005 ± 0.006
π^-	ψ	-0.017 ± 0.003	1.033 ± 0.003	0.066 ± 0.006	0.953 ± 0.006
	$\tan(\lambda)$	0.085 ± 0.004	1.061 ± 0.003	0.042 ± 0.007	1.006 ± 0.005
	$1/P_{xy}$	-0.019 ± 0.003	1.036 ± 0.003	0.023 ± 0.006	0.967 ± 0.006
γ	ϕ	0.023 ± 0.002	1.187 ± 0.002	-0.011 ± 0.003	1.027 ± 0.003
	θ	-0.179 ± 0.002	1.105 ± 0.001	-0.099 ± 0.003	1.062 ± 0.002
	$\sqrt{\mathrm{E}}$	0.306 ± 0.002	1.162 ± 0.001	0.240 ± 0.003	1.043 ± 0.003

Table A.6: Pulls for July 2-Prong Data.

Kinematic Fit to $\bar{p}p \to \pi^+\pi^-\pi^0\gamma\gamma$ at 1.94GeV/c					
Fit Parameter		Real Data		MC Data	
		Mean	Sigma	Mean	Sigma
π^+	ψ	0.027 ± 0.004	1.025 ± 0.003	0.023 ± 0.007	0.955 ± 0.006
	$\tan(\lambda)$	0.103 ± 0.004	1.040 ± 0.003	0.071 ± 0.007	0.985 ± 0.005
	$1/P_{xy}$	-0.001 ± 0.004	1.030 ± 0.003	-0.001 ± 0.007	0.987 ± 0.006
π^-	ψ	-0.017 ± 0.004	1.029 ± 0.003	0.051 ± 0.006	0.938 ± 0.006
	$\tan(\lambda)$	0.080 ± 0.004	1.030 ± 0.002	0.028 ± 0.007	0.989 ± 0.005
	$1/P_{xy}$	-0.022 ± 0.004	1.026 ± 0.003	0.003 ± 0.007	0.953 ± 0.006
γ	ϕ	0.036 ± 0.002	1.100 ± 0.001	-0.006 ± 0.004	1.067 ± 0.003
	θ	-0.077 ± 0.002	1.122 ± 0.001	-0.077 ± 0.004	1.118 ± 0.003
	$\sqrt{\mathrm{E}}$	0.177 ± 0.002	1.117 ± 0.001	0.171 ± 0.004	1.070 ± 0.003

Table A.7: Pulls for July 2-Prong Data.

Kinematic Fit to $\bar{p}p \rightarrow \pi^+\pi^-\pi^0\eta$ at 1.20GeV/c					
Fit Parameter		Real Data		MC Data	
		Mean	Sigma	Mean	Sigma
π^+	ψ	0.006 $\pm$ 0.009	1.003 $\pm$ 0.008	0.010 $\pm$ 0.007	0.931 $\pm$ 0.006
	$\tan(\lambda)$	0.116 $\pm$ 0.009	1.003 $\pm$ 0.007	0.086 $\pm$ 0.007	0.975 $\pm$ 0.005
	$1/P_{xy}$	-0.020 $\pm$ 0.009	1.013 $\pm$ 0.009	0.026 $\pm$ 0.007	0.958 $\pm$ 0.006
π^-	ψ	-0.011 $\pm$ 0.009	1.013 $\pm$ 0.008	0.062 $\pm$ 0.006	0.914 $\pm$ 0.006
	$\tan(\lambda)$	0.089 $\pm$ 0.009	1.018 $\pm$ 0.007	0.033 $\pm$ 0.007	0.975 $\pm$ 0.005
	$1/P_{xy}$	-0.012 $\pm$ 0.009	1.012 $\pm$ 0.008	0.031 $\pm$ 0.007	0.918 $\pm$ 0.006
γ	ϕ	0.006 $\pm$ 0.005	1.206 $\pm$ 0.004	-0.004 $\pm$ 0.004	1.001 $\pm$ 0.003
	θ	-0.062 $\pm$ 0.005	1.221 $\pm$ 0.004	-0.078 $\pm$ 0.004	1.065 $\pm$ 0.003
	$\sqrt{E}$	0.178 $\pm$ 0.006	1.245 $\pm$ 0.004	0.171 $\pm$ 0.004	1.055 $\pm$ 0.003

Table A.8: Pulls for July 2-Prong Data.

A.2.3 December 1991 0-Prong Data

Figure A.5 shows the CL distribution from the fits to energy-momentum, $\pi^0\pi^0\pi^0\gamma\gamma$ and $\pi^0\pi^0\pi^0\eta$. The slightly negative gradient implies that the errors are too small.

Kinematic Fit to Z-Vertex at 1.20GeV/c					
Fit Parameter		Real Data		MC Data	
		Mean	Sigma	Mean	Sigma
γ	$\sqrt{E}$	0.260 $\pm$ 0.002	1.519 $\pm$ 0.002	0.315 $\pm$ 0.003	1.207 $\pm$ 0.002

Table A.9: Pulls for December 0-Prong Data.

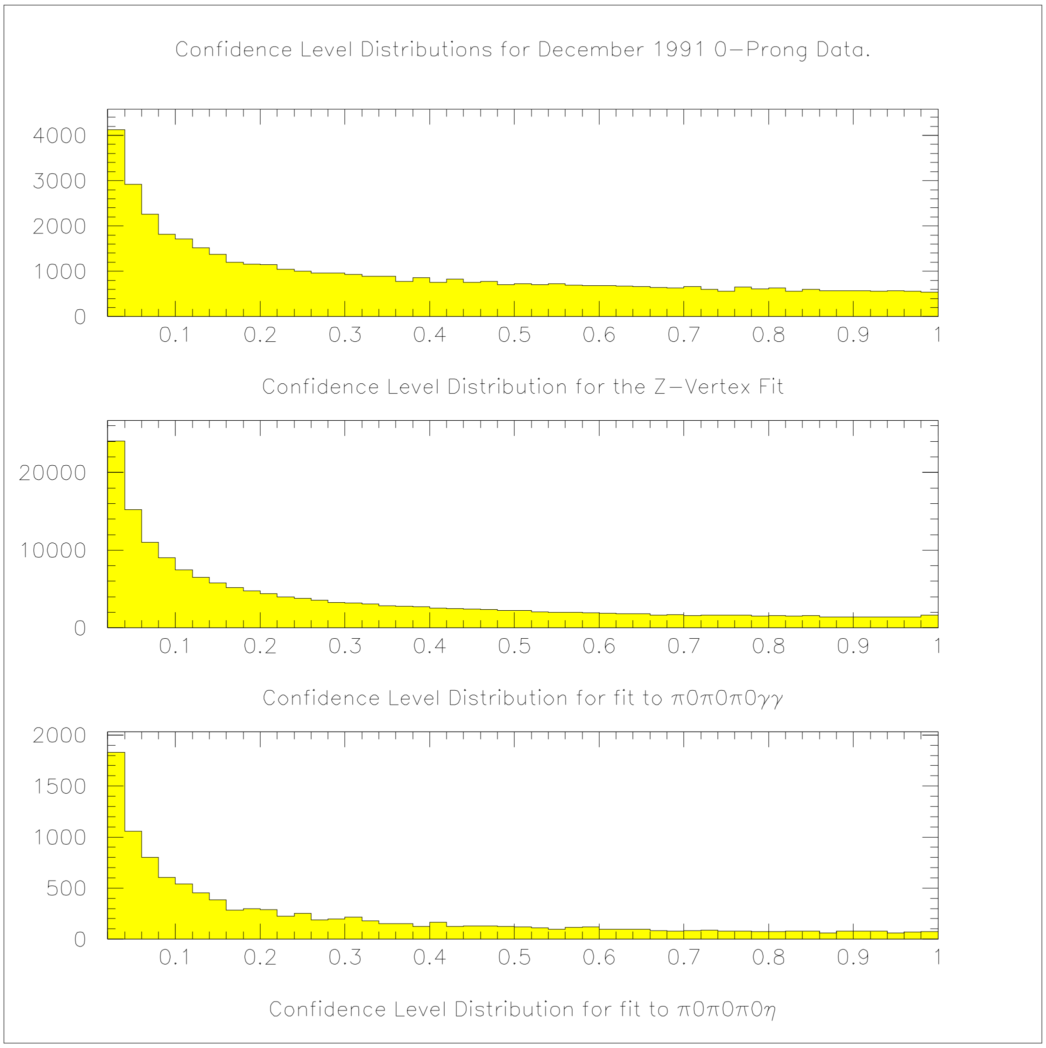

Figure A.5: CBKFIT: Confidence Level Distributions from the kinematic fitting of the December 1991 0-Prong Data.

Kinematic Fit to $\bar{p}p \rightarrow \pi^0\pi^0\pi^0\gamma\gamma$ at 1.20GeV/c					
Fit Parameter		Real Data		MC Data	
		Mean	Sigma	Mean	Sigma
γ	ϕ	-0.002 $\pm$ 0.002	1.095 $\pm$ 0.001	0.002 $\pm$ 0.002	1.020 $\pm$ 0.002
	θ	0.007 $\pm$ 0.002	0.970 $\pm$ 0.002	-0.022 $\pm$ 0.002	0.928 $\pm$ 0.002
	$\sqrt{\mathrm{E}}$	0.057 $\pm$ 0.002	1.097 $\pm$ 0.001	0.161 $\pm$ 0.002	0.959 $\pm$ 0.002

Table A.10: Pulls for December 0-Prong Data.

Kinematic Fit to $\bar{p}p \rightarrow \pi^0\pi^0\pi^0\eta$ at 1.20GeV/c					
Fit Parameter		Real Data		MC Data	
		Mean	Sigma	Mean	Sigma
γ	ϕ	0.002 $\pm$ 0.004	1.274 $\pm$ 0.003	0.002 $\pm$ 0.003	1.082 $\pm$ 0.002
	θ	0.001 $\pm$ 0.004	1.218 $\pm$ 0.003	-0.014 $\pm$ 0.003	1.064 $\pm$ 0.002
	$\sqrt{\mathrm{E}}$	-0.004 $\pm$ 0.004	1.196 $\pm$ 0.003	0.114 $\pm$ 0.002	0.972 $\pm$ 0.002

Table A.11: Pulls for December 0-Prong Data.

A.2.4 July 1992 0-Prong Data

Figure A.6 shows the CL distribution from the fits to energy-momentum, $\pi^0\pi^0\pi^0\gamma\gamma$ and $\pi^0\pi^0\pi^0\eta$. The flat distribution implies that overall, the errors were of the correct size.

Kinematic Fit to Z-Vertex at 1.94GeV/c					
Fit Parameter		Real Data		MC Data	
		Mean	Sigma	Mean	Sigma
γ	$\sqrt{E}$	0.204 ± 0.002	1.363 ± 0.002	0.359 ± 0.003	1.285 ± 0.003

Table A.12: Pulls for July 0-Prong Data.

Kinematic Fit to $\bar{p}p \rightarrow \pi^0\pi^0\pi^0\gamma\gamma$ at 1.94GeV/c					
Fit Parameter		Real Data		MC Data	
		Mean	Sigma	Mean	Sigma
γ	ϕ	0.000 ± 0.002	0.965 ± 0.001	-0.001 ± 0.003	1.049 ± 0.002
	θ	-0.001 ± 0.001	0.868 ± 0.001	-0.016 ± 0.003	0.955 ± 0.003
	$\sqrt{E}$	0.062 ± 0.002	0.995 ± 0.001	0.211 ± 0.003	0.986 ± 0.002

Table A.13: Pulls for July 0-Prong Data.

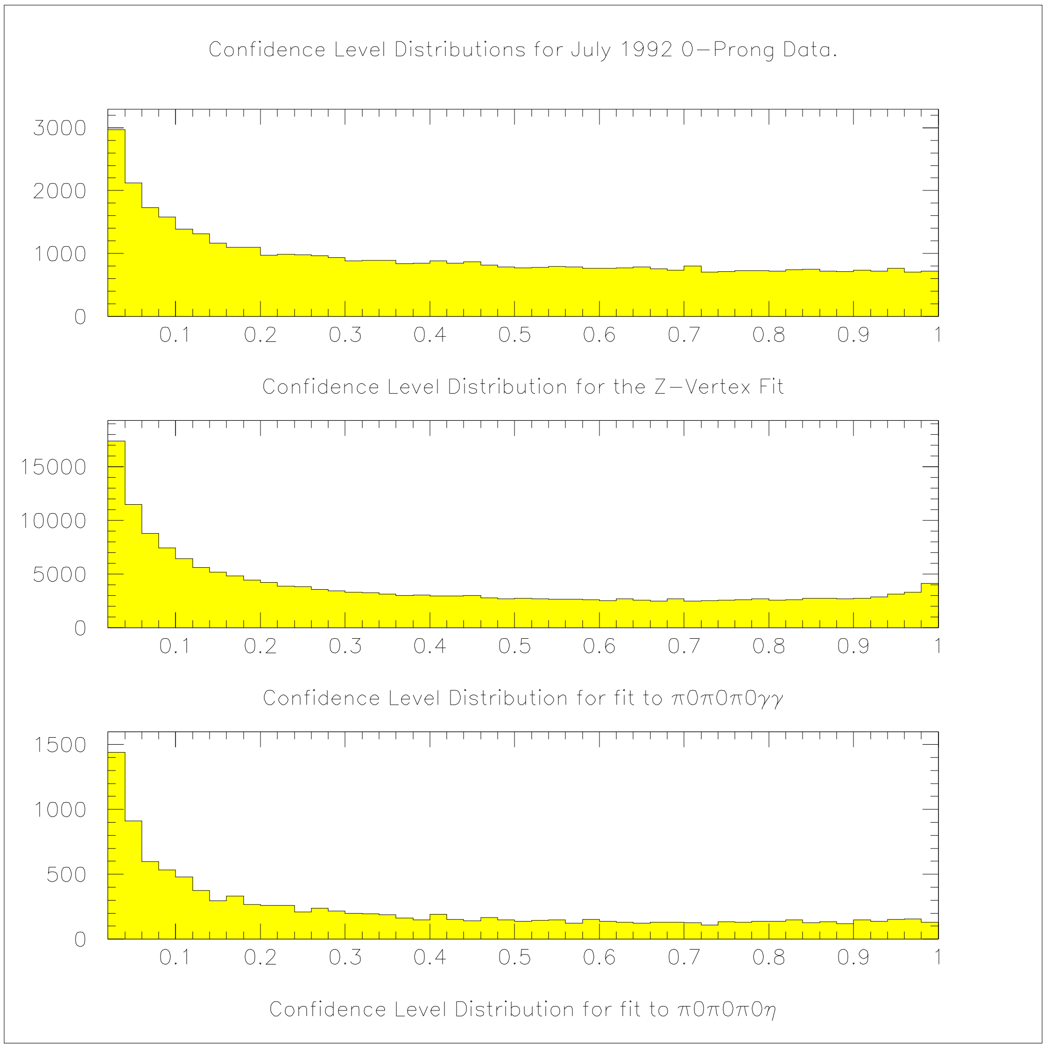

Figure A.6: CBKFIT: Confidence Level Distributions from the kinematic fitting of the July 1992 0-Prong Data.

Kinematic Fit to $\bar{p}p \rightarrow \pi^0\pi^0\pi^0\eta$ at 1.94GeV/c					
Fit Parameter		Real Data		MC Data	
		Mean	Sigma	Mean	Sigma
γ	ϕ	0.004 $\pm$ 0.004	1.217 $\pm$ 0.003	0.000 $\pm$ 0.003	1.111 $\pm$ 0.003
	θ	0.014 $\pm$ 0.004	1.179 $\pm$ 0.003	-0.001 $\pm$ 0.003	1.073 $\pm$ 0.003
	$\sqrt{\mathrm{E}}$	0.011 $\pm$ 0.004	1.146 $\pm$ 0.003	0.168 $\pm$ 0.003	1.004 $\pm$ 0.003

Table A.14: Pulls for July 0-Prong Data.

Bibliography

[1] F Abe *et al.*, FERMILAB-PUB-94/116-E May (1994)

[2] IJR Aitchison & AJG Hey, “Gauge Theories in Particle Physics” ed. DF Brewer (Adam Hilger)

[3] SL Glashow, Nucl. Phys. **22** 1961 (579)

[4] A Salam, “Elementary Particle Theory” ed. N Svartholm (Stockholm: Almqvist)

[5] S Weinberg, Phys. Rev. Lett. **19** 1967 (1264)

[6] M Gell-Mann & Y Ne’eman, Phys. Lett. **8** 1964 (214)

[7] M Aguilar-Benitez *et al.*, Rev. of Particle Properties, Phys. Rev. **D 45** (1992)

[8] T de Grand, RL Jaffe, K Johnson and J Kiskis, Phys. Rev. **D12**, 2060, (1975)

[9] NN Achasov, SA Devyanin and GN Shestakov, Sov. Phys. Usp., **27**, 161, (1984)

[10] R Kokoski and N Isgur, Phys. Rev., **D35**, 907, (1987)

[11] J Gasser and H Leutwyler, Nucl. Phys., **B250** 465,517 and 539 (1985)

[12] AJG Hey, Surv. High Energy Physics, **5**, 287, (1987)

[13] F Close, “Spectroscopy of Light and Heavy Quarks” Ed. U Gastaldi, R Klapisch & F Close

[14] M Poulet, "Exotic Mesons" First Biennial Conf. on Low Energy Antiproton Physics., World Scientific Publishing Co. (1991)

[15] F Close, AIP Conf. Proc. **185** ed. SU Chung, Brookhaven (1988)

[16] FG Binon, Nuclear Physics B (Proc. Suppl.) **8** 24 (1989)

[17] RL Jaffe & K Johnson, Phys. Lett. **60B**, 201, (1976)

[18] VV Anisovich *et al.*, Phys. Lett. **322**, 431, (1994)

[19] M Burchell, CERN-PPE/92-158 September (1992)

[20] C Amsler *et al.*, Nuclear Instruments and Methods in Physics Research, **A321**, 69-108, (1992)

[21] LeCroy, Multi Wire Proportional Chamber System.

[22] H. Drumm *et al.*, Nucl. Instr. and Meth. **176**, 333, (1980)

[23] LeCroy, Fast Encoding and Readout System.

[24] LeCroy, 2282 High Density ADC Data Acquisition System.

[25] R. Brun and J. Zoll, ZEBRA user guide, CERN Program Library Q100, (1987)

[26] K. Braune, The Fast Cluster Encoder, CB-Note 41, (1986), Unpublished.

[27] G. Folger and M. Doser, Crystal Barrel Offline Reconstruction Software, CB-Note 121, (1993), Unpublished.

[28] C. Meyer, Crystal Barrel Chamber Reconstruction Software, CB-Note 93, (1991), Unpublished.

[29] C. Meyer, Crystal Barrel Chamber Reconstruction Software: User Guide., CB-Note 123, (1991), Unpublished.

[30] F.H. Heinsius and T. Kiel, Crystal Barrel Crystal Data Reconstruction Software, CB-Note 92, (1991), Unpublished.

[31] M. Burchell, Crystal Barrel Global Tracking Particle Bank Structure, CB-Note 118, (1991), Unpublished.

[32] R. Veenhof, CERN program library W5050 (1989)

[33] N. Hessey, Split-off recognition with Dolby-C, CB-Note 199, (1992), Unpublished.

[34] C. Meyer, User Guide for CBDROP - A Charged Split-Off Suppression Package, CB-Note 191, (1992), Unpublished.

[35] P. Hidas and G. Pinter, Kinematic Fitting Software, CB-Note 138, (1993), Unpublished.

[36] Program 353QH, CERN Program Library (1987)

[37] W Chinowsky, G Goldhaber *et al.*, Phys. Rev. Letters **9**, 330 (1962)

[38] G Goldhaber, W Chinowsky *et al.*, Phys. Letters **6**, 62 (1963)

[39] BS Zou and DV Bugg, Phys. Rev., **D48**, 3948, (1993)

[40] A subroutine for Fitting the χ^2 and Maximum Likelihood Function (FUMILI, LIKELM), CERN Program Library, **D510** 1971.

[41] C Bourrely, E Leader and J Soffer, Phys. Reports, **59**, Number 2, March 1980.

[42] YU D Prokoshkin, Hadron 89 Conference. p27

[43] K Karch *et al.*, Phys Lett. **B249** 353 (1990)

[44] SI Bityukov *et al.*, Protvino preprint IFVE-91-26

[45] W Stockhausen, SLAC preprint SLAC-PUB-4026 July (1986)

Acknowledgements

I would like to thank the following people for their encouragement and assistance.

David Bugg (supervisor, top scientist & ex-Ipswich player), the UK team: Tony Baker, Chris Batty, Chris Pinder, Iain Scott & Bing Song Zou. The Crystal Barrel collaboration (In particular Nigel Hessey, Michael Doser & Curtis Meyer who endured my persistent questions). The people at QMW college, especially Adil Hasan, Gary (LL) Barker, Mike Akrawy, Asif Malik, Paul Singh, John Heatherington, Mohsin Raza, Andy Yeaman. Derek Newman-Coburn, my hair stylist advisor. The Scouse group: Emmett Cawley, Andy Cody, Kev Forbes, Colum Higgins and Barry King. Martin Bates for putting up with Barker. Phil Bysh and John Burgoyne for putting up with me. My family for listening and the advice: "Finish the analysis and write it up". Suzanne for her patience, support and cooking.

I acknowledge the financial support of the SERC.